The Dissertation Committee for Lizhi Zheng Certifies that this is the approved version of the following dissertation:

NITRATE REMOVAL EFFICIENCY IN HYPORHEIC ZONES: THE EFFECT OF TEMPERATURE AND BEDFORM DYNAMICS

Committee:

Meinhard Bayani Cardenas, Supervisor

Philip C Bennett

David Mohrig

Charles J. Werth

Kevan B. Moffett

NITRATE REMOVAL EFFICIENCY IN HYPORHEIC ZONES: THE EFFECT OF TEMPERATURE AND BEDFORM DYNAMICS

by

Lizhi Zheng

Dissertation

Presented to the Faculty of the Graduate School of

The University of Texas at Austin

in Partial Fulfillment

of the Requirements

for the Degree of

Doctor of Philosophy

The University of Texas at Austin

August 2017

Acknowledgements

I would like to thank my advisor M. Bayani Cardenas for his generous guidance, unwavering support, and understanding. I appreciate his instant feedback on my paper and dissertation. No one can believe I always get his feedback within three days, sometimes even within one day. That is unbelievable since he is working as an editor of Geophysical Research Letter with tight schedules.

I would like to thank my committee member David Mohrig for being so generous to provide me the material for reference and finding time to meet with me in his busy schedule.

I would like to thank my committee member Kevan Moffett for her feedbacks on every step or process of my dissertation. She is my role model. She has two kids, but know how to balance work and life.

I would like to thank my other committee members Phil Bennett and Charles J. Werth for accepting my delay submission of the draft.

I would like to thank Jackson School for affording me the TA position and all the help and support from the staff.

I would like to thank the National Science Foundation (EAR-0955750) and the Geology Foundation at the University of Texas at Austin for financial support of my research.

I would like to thank all my close friends and colleagues I met in Austin. I cannot finish my PhD without all your help and support.

I would like to thank my parents-in law to help me take care of my daughter.

I would like to thank my parents, my sister, and my brother to their love and being my strongest supporters all the time.

Finally, I would like to thank my husband for his patience, support, encourage, and understanding. Most importantly, I appreciate his sacrifice for the family in his academia career. He chose to continue his postdoc in the same research group after graduation in order to stay with me and our newborn baby. I know he deserved a better offer.

NITRATE REMOVAL EFFICIENCY IN HYPORHEIC ZONES: THE EFFECT OF TEMPERATURE AND BEDFORM DYNAMICS

Lizhi Zheng, Ph.D.

The University of Texas at Austin, 2017

Supervisor: Meinhard Bayani Cardenas

Fundamental understanding of bedform-induced hyporheic flow and how it controls the nitrate dynamics in the hyporheic zone (HZ) is critical for environmental and ecological problems, such as eutrophication, deterioration of water quality, and loss of biodiversity. The HZ is regarded as a biogeochemical hotspot for removing nitrate from the river system. Although hyporheic flux has been extensively studied in the HZ in the last decade, the cycle of nitrate dynamics in the HZ is still poorly understood. To better characterize and predict nitrate cycling in the HZ, I have investigated the role of HZ in removing nitrate in response to temperature variations and bedform migration through numerical experiments.

I have designed and generated all bedform shapes for this dissertation. All numerical experiments followed the same sequential procedures: (1) Solving Reynolds-averaged Navier-Stokes equations to obtain pressure distribution along the sediment-water interface; (2) The bedform-induced pressure along sediment-water interface drives water entering into and out of HZ by solving the Darcy's equation; (3) Meanwhile, the transport equations were implemented for solving reactive species and/or temperature distributions, depending on whether temperature was assumed to be spatially heterogeneous or homogeneous. The reactive species were either consumed or produced that was closely related to the reaction chains for the nitrate transformations in the HZ.

Here, we only considered aerobic respiration, denitrification, and nitrification for nitrate cycling in the HZ.

My dissertation started with the simplest cases assuming uniform temperature in the HZ. I found that nitrate transformations in the HZ are temperature-dependent since the chemical reaction rates increase with enlarging temperature. The functionality of HZ acting as nitrate source or sink depends strongly on the stream water quality. When the HZ serves as nitrate sink, the nitrate removal efficiency increases with temperature. Moreover, since temperature changes diurnally following a sinusoidal function, a persistent biogeochemical hotspot for removing nitrate is present regardless of the occurrence of dynamic and complex hyporheic temperature patterns. The daily-averaged nitrate removal efficiency with instantaneously changing temperature is fairly identical to the counterpart by using uniform temperature in the HZ. Last but not least, I generated more realistic moving ripple bedforms. The migration rate of ripples causes different hyporheic flux and thus reactive transport processes in the HZ. I found that the nitrate removal efficiency increases asymptotically with Damköhler number, and the immobile ripples overestimate the nitrate removal efficiency compared to that for mobile ripples. All above-mentioned research results can be readily extended for large scales.

Table of Contents

List of Tables

List of Figures

Chapter 1: Introduction

1.1 MOTIVATION AND PROBLEM STATEMENTS

Human activities have greatly disturbed the global nitrogen cycle [*Gruber and Galloway*, 2008]. The excess nitrogen has been causing many serious ecological and environmental issues [*Birgand et al.*, 2007], including deterioration of water quality, coastal eutrophication, loss of biodiversity.

Streams and rivers are considered as the most important sites in removing nitrogen [*Peterson et al.*, 2001], and controlling nitrogen exports to the downstream coastal waters [*Alexander et al.*, 2000; *Seitzinger et al.*, 2002]. "At least half of the nitrogen entering river systems appears to be lost on its way to the sea" [*Galloway et al.*, 2004]. Fundamental understanding of the mechanisms and factors controlling the nitrogen dynamics in streams and rivers is thus essential for fluvial ecosystem and management of river networks.

Streams and rivers cannot be simply seen as pipelines to the sea. The hyporheic zone (HZ) is the transition zone that connect the stream water and the underlying aquifer. It plays as the role of the liver of the whole fluvial ecosystems [*Fischer et al.*, 2005]. Essentially, stream water enters into the HZ, carrying solute and heat, after a short flow path, returns to stream water. The HZ is a hot spot for biogeochemical reactions due to its biologically active streambed sediments [*Boulton et al.*, 1998; *Mazza et al.*, 2014; *Zarnetske et al.*, 2012]. N transformations occurring in HZs determine the amount and

fate of N traveling through the porous sediment, and thus controlling the water quality and N export to the sea [*Alexander et al.*, 2000; *Birgand et al.*, 2007; *Gomez et al.*, 2015; *Peterson et al.*, 2001].

Since stream water temperature varies daily and seasonally, this results in complex and dynamic thermal pattern in HZs [*Marzadri et al.*, 2013]. Temperature influences hyporheic flux and supply rate of solutes. In addition, most biogeochemical reactions are temperature dependent. Few research consider about the temperature effect on nitrogen dynamics in HZs. Moreover, most studies on HZ assumed that bedform is immobile and thus hyporheic flux is purely caused by pumping effect. However, the ubiquitous bedform migration can lead to turnover effect, which could greatly change the flow field, hyporheic flux, supply rate of solute, and chemical reactions [*Ahmerkamp et al.*, 2015; *Kessler et al.*, 2015; *Packman and Brooks*, 2001; *Rutherford et al.*, 1993]. To fill above-mentioned gaps, my dissertation aims at addressing the following scientific questions:

(1) Effects of temperature:

- Q1A: How does uniformly distributed temperature affect nitrogen dynamics in the HZ? We assumes that the stream water temperature is constant over time.
- Q1B: How do dynamic changes in surface water temperature affect nitrogen dynamics in the HZ?

(2) Effects of bedform morphodynamics:

- Q2: How does bedform mobility affect hyporheic exchange and consequent nitrogen dynamics?

1.2 ORGANIZATION OF DISSERTATION

The organization of the dissertation is to address above questions in each chapter. Each chapter has its own Abstract, Introduction, Methods, Results, Discussion, and Conclusions for journal publication. All the references for each chapter are collated in the Bibliography.

Chapter 2 examines the effect of steady temperature on nitrogen cycling in bedform-induced hyporheic zones. I found that the function of HZ as a nitrate source or sink strongly depends on the concentration ratio (i.e., $[NO_3^-]/[NH_4^+]$) of stream water. At high concentration ratio, denitrification was dominant over nitrification in the HZ. The HZ functioned as a nitrate sink, and the nitrate removal efficiency increased with temperature. At low concentration ratio, nitrification was dominant in the HZ, so the HZ functioned as a nitrate source with the nitrate production efficiency increasing with temperature. At intermediate concentration ratio, the function of HZ can switch from a nitrate sink to a nitrate source with increasing temperature.

Chapter 3 investigates the effects of diurnal stream temperature on the nitrate removal efficiency in the HZ. I conducted a series of multiphysics numerical simulations through a fully coupled model, including fluid flow, heat transport, and reactive *C* and *N* transport in the HZs. Although thermal patterns in the HZ were dynamic and complex, a biogeochemical hotspot with significant denitrification rates persisted. The nitrate removal efficiency fluctuated strongly over a day caused by the stream temperature variation. Surprisingly, the daily average nitrate removal efficiency with dynamic stream

temperature was effectively the same as those with constant and equivalent temperature for denitrification-dominant systems.

Chapter 4 explores the impact of ripple migration on the nitrogen dynamics in the HZ. I designed several realistic ripple geometries based on bedform stability, which is fundamentally dependent on mean stream velocity and median grain size. The "turnover" effect caused by bedform migration had a large influence on supply rate and chemical reaction rates. The nitrate removal efficiency increased asymptotically with Damköhler number for both mobile and immobile bedforms, but the immobile bedform always had a higher nitrate removal efficiency.

Chapter 5 summarizes the key findings in this dissertation, and put forward future research.

Chapter 2: Temperature effects on nitrogen cycling and nitrate removal-production efficiency in bedform-induced hyporheic zones[1]

2.1 ABSTRACT

Hyporheic flow in aquatic sediment controls solute and heat transport thereby mediating the fate of nutrients and contaminants, dissolved oxygen, and temperature in the hyporheic zone (HZ). We conducted a series of numerical simulations of hyporheic processes within a dune with different uniform temperatures, coupling turbulent open-channel fluid flow, porous fluid flow, and reactive solute transport, to study the temperature dependence of nitrogen source/sink functionality and its efficiency. Two cases were considered: a polluted (nutrient-rich) and a pristine (nutrient-poor) stream. Sensitivity analysis was performed to investigate the influence of stream water $[NO_3^-]$ /$[NH_4^+]$. The simulations showed that in both cases warmer temperatures resulted in shallower denitrification zones and oxic-anoxic zone boundaries, but the trend of net denitrification rate and nitrate removal or production efficiency of the HZ for these two cases differed. For both cases, at high $[NO_3^-]$ /$[NH_4^+]$, the HZ functioned as a NO_3^- sink with the nitrate removal efficiency increasing with temperature. But at low $[NO_3^-]$ /$[NH_4^+]$ for the polluted stream, the HZ is a NO_3^- sink at low temperature, but then switches to a NO_3^- source at warmer temperatures. For the pristine stream case, the HZ was always a

[1] Zheng, L., M. B. Cardenas, and L. Wang (2016), Temperature effects on nitrogen cycling and nitrate removal-production efficiency in bed form-induced hyporheic zones, Journal of Geophysical Research: Biogeosciences, 121(4), 1086-1103. Dr.Wang instructed me set up numerical simulations.

NO_3^- source, with the NO_3^- production efficiency increasing monotonically with temperature. In addition, although the interfacial fluid flux expectedly increased with the increasing temperature due to decreasing fluid viscosity, the total nitrate flux into the HZ did not follow this trend. This is because when HZ nitrification is high, uniformly elevated [NO_3^-] lowers dispersive fluxes into the HZ. We found that there are numerous confounding and interacting factors that combined to lead to final temperature-dependence of N transformation reaction rates. Although the temperature effect on the rate constant ca be considered as the dominant factor, but simply using the Arrhenius equation to predict the reaction rate would lead to incomplete insight by ignoring the changes in interfacial fluid flux and reaction areas. Our study shows that HZ temperature and stream [NO_3^-] /[NH_4^+] are key controls for HZ sink/source functions.

2.2 INTRODUCTION

Excess bio-available nitrogen in stream waters, especially nitrate (NO_3^-) is a significant concern because it is a drinking water pollutant and causes eutrophication that threatens aquatic ecosystems [*Boano et al.*, 2014; *Galloway et al.*, 2003; *Groffman et al.*, 2005]. Previous studies have shown that small first-order streams [*Peterson et al.*, 2001] are important locations of nitrogen (N) transport and retention that can strongly affect downstream N exports [*Alexander et al.*, 2000; *Gomez-Velez et al.*, 2015; *Howard-Williams et al.*, 1983; *Kiel and Cardenas*, 2014]. There is widespread evidence that N can be removed from water ways during its downstream transport through watersheds [*Engler and Patrick*, 1974; *Kaushik and Robinson*, 1976]. The fraction of removal of N in streams compared to the overall N budget in watersheds could reach 40% or even more

[*Birgand et al.*, 2007]. Nitrogen could be temporarily reduced within the stream water through, for example, assimilation by plant nitrogen uptake [*Howard-Williams et al.*, 1983], and storage of N in the sediment [*Birgand et al.*, 2007; *Svendsen and Kronvang*, 1993]. The broad literature on the removal of N in streams highlighted the critical role of denitrification. Denitrification is considered as the main mechanism that could permanently remove NO_3^- from streams. For example, it has been suggested that at least half of the NO_3^-entering river systems appears to be "lost" due to denitrification on its way to the ocean [*Alexander et al.*, 2009; *Galloway et al*.,2003] .

Streams and aquifers are two critical parts of the hydrosphere that are intimately connected through the hyporheic zone (HZ), which is the transition zone between the surface water and subsurface water in fluvial systems. Pore water in subsurface sediment is continuously circulated through and exchanged with the overlying surface water defining HZs. Hyporheic exchange drives advection of solute mass and energy and exerts a strong influence on the quality of both surface and subsurface waters and on fluvial ecology [*Boano et al.*, 2014; *Cardenas*, 2015; *Harvey and Gooseff*, 2015]. A large number of factors influence hyporheic exchange, which have been investigated in previous studies through mathematical models, flume experiments and field studies. These physical factors include streambed topography, sediment permeability and heterogeneity, sediment transport, large woody debris and other obstacles in rivers, stream discharge, and stream curvature [*Cardenas*, 2008a; *Cardenas et al.*, 2004; *Packman and Salehin*, 2003; *Sawyer et al.*, 2011, *Ahmerkamp et al.*, 2015].

HZs are recognized as ecotones or perhaps a unique ecosystem providing vital

functions [*Boulton et al.*, 1998; *Brunke and Gonser*, 1997; *Findlay*, 1995; *Jones Jr and Holmes*, 1996; *Stanford and Ward*, 1988]. The HZ is rich in biologically active sediment, creating a favorable condition for microbially facilitated reactions to occur, including organic carbon oxidation (aerobic respiration), nitrification, and denitrification. A large number of investigations have shown that the HZs serve as the active sites of N biogeochemical dynamics [*Bardini et al.*, 2012; *Cirmo and McDonnell*, 1997; *Duff and Triska*, 1990; *Kessler et al.*, 2014; *Zarnetske et al.*, 2012], determine the amount and fate of N travelling through the streambed sediment, and are thus influencing water quality in the stream channel [*Harvey et al.*, 2013; *Bardini et al.*, 2012; *Marzadri et al.*, 2012; *Zarnetske et al.*, 2012]; these have been shown to be important at the river network scale [*Kiel and Cardenas*, 2014; *Gomez-Velez et al.*, 2015].

The biogeochemical reactions in the HZ could produce or consume inorganic N (NH_4^+, NO_3^-) and thus affect stream water quality and ultimately ecosystem health [*Groffman et al.*, 2005]. The potential function of the HZ as a source or sink of NO_3^- is primarily controlled by the supply and demand of O_2 because O_2 largely determines the redox conditions which regulate where and when nitrification and denitrification occur [*Zarnetske et al.*, 2012]. Denitrification in the HZs has been found to reduce NO_3^- levels in streams and rivers which could decrease or buffer eutrophication [*Clément et al.*, 2002; *Martin et al.*, 2001; *McClain et al.*, 2003] when the HZ provides a NO_3^- sink role. On the other hand, HZs can also be a NO_3^- source when nitrification is dominant over denitrification [*Jones Jr et al.*, 1995]. In addition to favorable redox conditions, denitrification is also controlled by the availability of labile carbon [*Jones Jr and Holmes*,

1996; *Zarnetske et al.*, 2011], and thus the C and N cycles in the HZ are intimately coupled.

Most biogeochemical reactions are sensitive to temperature, especially bacterially mediated reactions. Thus, temperature could play an important role in the biogeochemical processes within the HZ. Furthermore, HZs are subject to spatially and temporally varying temperatures. For example, a diel temperature pattern following stream water would penetrate through the sediment water interface (SWI) and result in a dynamic temperature pattern, which would potentially affect the biogeochemical reactions in the HZ [*Cardenas and Wilson*, 2007b; *Norman and Cardenas*, 2014; *Sawyer et al.*, 2012; *Swanson and Cardenas*, 2010]. Since rivers are subject to seasonal temperature changes, so are their HZs. However, there have been few studies focused on coupling and integrating fluid flow, heat transport, and reactive solute transport to understand the complex links and feedbacks between hydrodynamic, biogeochemical, and thermal processes in the HZ. Therefore, an integrated framework is necessary.

The goal of this study is to understand and quantify the effect of temperature on nitrate removal and production efficiency in bedform-induced hyporheic zones. We investigated and analyzed the pertinent coupled processes of fluid flow, and temperature-dependent biogeochemical reactions. We used multiphysics numerical models that integrate all the above processes but focus on N biogeochemistry. We take into account four representative reactive compounds pertinent in N cycling: dissolved organic carbon (DOC), dissolved oxygen (DO), nitrate (NO_3^-), and ammonium (NH_4^+). These species are usually used as direct indicators of water quality in field studies and they have direct

influence on many aquatic ecosystems [*Bardini et al.*, 2012]. Since the effects of dynamic temperatures are potentially complex, we first study the steady temperature effect. This paper addresses the steady temperature effect on nitrate removal-production efficiency, future work will analyze the effect of diurnal temperature variations.

A series of numerical simulations with different homogeneous temperatures, increasing from 5 °C to 35°C in increments of 5 °C, were conducted. The models simulated the distributions of chemical species and reaction rates in the HZ. Integration of nitrification, denitrification and net denitrification rates in the HZ was conducted to further evaluate the over-all NO_3^- removal or production efficiency occurring within the HZ. We focused on two stream water quality scenarios, a polluted stream, with high nutrient concentration (nutrient-rich) and pristine stream , with low nutrient concentration (nutrient-poor) but no limitation on DOC following *Bardini et al*. [2012]. A sensitivity analysis was performed to gain broader insight.

2. 3 METHODOLOGY AND THEORETICAL BACKGROUND

The modeling scheme follows those presented previously in *Cardenas and Wilson* [2007a] and *Bardini et al.* [2012; 2013]; this is conceptually illustrated in Figure 2.1. Briefly, the method is as follows: (1) turbulent flow was modeled above a dune bedform; (2) the pressure along the SWI from the turbulent flow model is used as a boundary condition for a groundwater flow model; (3) the groundwater flow field is used to model reactive transport where the reaction kinetics are temperature-dependent. For this study, a steady and homogeneous temperature field is assumed.

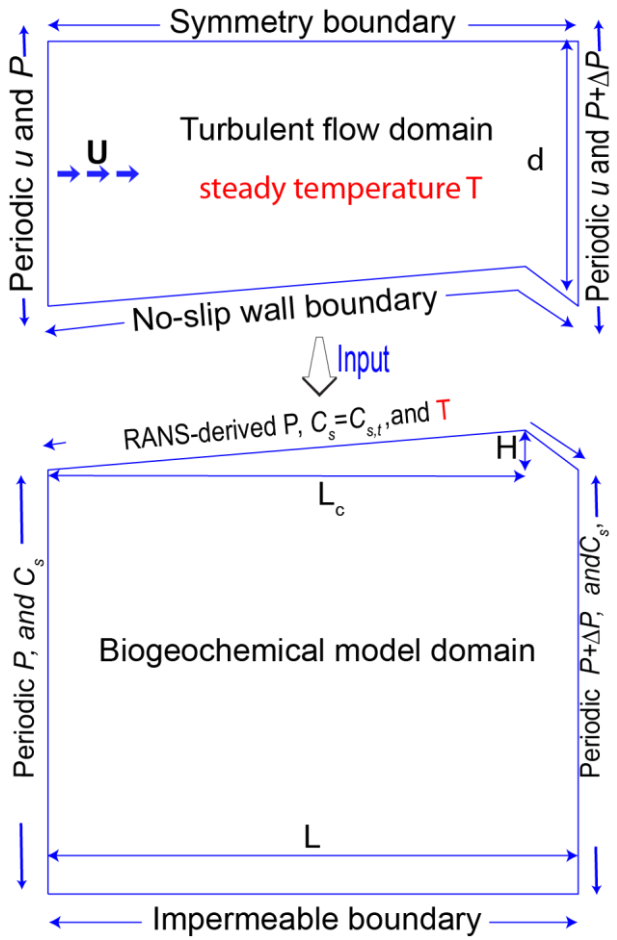

Figure 2.1: Schematic representation of numerical modeling approach for the physical-biogeochemical processes occuring in a representative bedform-induced HZ. The streambed length L=1 m, height H=0.05 m, with the crest at 0.9 L (Lc=0.9 m), and the sediment thickness is 0.8 m. The upper panel represents the stream flow (water depth d=0.5 m), while the lower panel represents the permeable porous sediment. T is temperature, P is pressure, C is solute concentration, and U is stream velocity.

2.3.1 Turbulent flow modeling for pressure distribution along the interface

Mean unidirectional turbulent flow in the water column over the bedform was modeled by numerically solving a finite-volume formulation of Reynolds-averaged Navier-Stokes (RANS) equations for an incompressible, homogeneous and isothermal fluid with the k-ω closure scheme [*Wilcox*, 1991]. This approach has been validated showing that the simulated pressure profiles along the SWI agrees reasonably well with experimental observations [*Cardenas and Wilson*, 2007a; *Janssen et al.*, 2012]. In this study, we did not conduct actual turbulent flow modeling. Instead, we took the result of one model from *Cardenas and Wilson* [2007a]. But for completeness, we briefly discuss the model conditions and parameters here.

A symmetry boundary condition was used at the top of the RANS domain [*Cardenas and Wilson*, 2007a]. Spatially periodic pressure conditions were prescribed on the lateral boundaries, with a specified pressure drop (ΔP) [*Bardini et al.*, 2012] between the left and right boundaries of the RANS domain which represents the channel slope. The bottom of the domain (SWI) was treated as a no-slip wall boundary condition that neglects the influence of subsurface flow below the RANS domain. We retrieved the time-averaged pressure distribution (considered as the steady-state pressure) along the SWI from the RANS simulation. This pressure distribution is further used as a Dirichlet boundary condition for simulating fluid flow through the porous sediment, and thus determines the hyporheic exchange across the SWI and flow within the HZ. The RANS model result used here has a water depth of 0.5 m above the trough and a mean flow velocity of 0.4 m/s, leading to a Reynolds Number of 20,000 (with the bedform crest

height as the length scale). In all models, the bedform length L=1 m, height H=0.05 m, with the crest at 0.9L.

2.3.2 Pore water flow through the sediment

Two-dimensional porous-media flow in the sediment (Figure 2.1) is solved using the steady-state groundwater flow equations (i.e., the continuity equation and Darcy's Law) which reads as:

$$\nabla \cdot q = 0 \tag{2.1}$$

$$q = -\frac{k_p}{\mu(T)} \nabla P \tag{2.2}$$

where q is the Darcy flux, k_p is intrinsic permeability, μ is the fluid viscosity depending on T, and P is the pressure.

The top boundary of the porous domain (the SWI) is a Dirichlet boundary defined by the RANS-derived pressure distribution. The lateral boundaries are spatially periodic boundaries with a prescribed pressure drop (ΔP) (Figure 2.1), which is the same as applied for the RANS domain. This approach results in a continuous pressure distribution across the RANS domain and porous domain [*Cardenas and Wilson*, 2007a]. The bottom of the porous flow domain, which is at a depth of 0.8 m, was assigned as a no-flux boundary. The sediment is assumed to be homogeneous and isotropic with a k_p=5×10^{-11} m^2 which roughly corresponds to medium to coarse sand.

2.3.3 Multi-component reactive transport modeling

Hyporheic flow carries carbon, nutrients, and dissolved oxygen into the sediment that makes microbially facilitated reactions more likely to occur in the biologically-active

sediments. In particular, we consider four representative reactive compounds: dissolved organic carbon (DOC), dissolved oxygen (DO), nitrate (NO_3^-), and ammonium (NH_4^+). Formaldehyde (CH_2O) is used here to represent complex DOC substrate due to its simple chemical structure following [*Bardini et al.*, 2012]. We do not consider particulate organic carbon (POC) specifically in this study, since POC particles could affect the permeability of the sediment and distribution of the bacteria community, which may make the system too complex to study. We assume all the nutrients and carbon in the sediments come from the penetration of stream water in the streambed. The multi-component reactive transport model explicitly simulates three critical chemical reactions that govern nitrogen biogeochemistry: nitrification (NI), denitrification (DN), and aerobic respiration of dissolved organic matter (AR) (Table 2.1). Other N transformations, such as anaerobic ammonium oxidation (ANAMMOX) and dissimilatory nitrate reduction to ammonium (DNRA), can also affect the cycling of nitrate and ammonium in fluvial systems. But compared to nitrification and denitrification, they can be negligible [*Zarnetske et al.*, 2012].

In this study, the microbial degradation of organic compounds was considered as a primary reaction and serves as the ultimate source of chemical energy [*Hunter et al.*, 1998]. For simplicity, first-order degradation kinetics is assumed for the DOC oxidation rate r_{DOC}:

$$r_{\mathrm{DOC}} = k_{\mathrm{DOC}} \cdot C_{DOC} \tag{2.3}$$

where k_{DOC} is the first-order reaction rate constant (i.e., the DOC decay constant);C_{DOC} is the DOC molar concentration.. The linear kinetics in equation (2.3) is the simplest way to

represent DOC degradation [*Bardini et al.*, 2012], since other methods (i.e. Monod) need more parameters. This further implies that the availability of primary organic substrate determines the overall degree of enzymatic activity of the microbial community [*Hunter et al.*, 1998].

We assume that the electrons released by DOC degradation are transferred to the potential terminal electron acceptors, in this study we only have O_2 andNO_3^-, which is used by microorganisms sequentially. As we know the total rate of electrons that are released by DOC degradation, then the reduction rate of $r_{red,i}$ of the i-th electron acceptor (i=1 for O_2, i=2 for NO_3^-) can be estimated based on their contribution:

$$r_{red,i} = f_i \cdot r_{DOC} \cdot \beta_i \quad (i = 1,2) \tag{2.4}$$

where f_i is the fraction of electrons consumed by the *i*-th reduction half-reaction, and β_i (table 1) is the ratio between the moles of transferred electrons per mole of oxidized DOC and the moles of electrons per mole of reduced compound in the *i*-th reaction. The fraction f_i is defined with a simplified Monod formulation for the utilization of the terminal electron acceptors [*Bardini et al.*, 2012; *Hunter et al.*, 1998] following:

$$f_i = \left(1 - \sum_{n=0}^{i-1} f_n\right) \cdot \alpha_i \tag{2.5}$$

with f_0=0 and:

$$\alpha_i = \begin{cases} \frac{C_i}{C_{i,lim}} & if\ C_i < C_{i,lim} \\ 1 & if\ C_i \geq C_{i,lim} \end{cases} \tag{2.6}$$

where C_i and $C_{i,lim}$ are the molar concentration and the molar limiting concentration of the *i*-th reaction electron acceptor, respectively. α_i is a dimensionless parameter that assumes each electron acceptor has a limiting concentration ($C_{i,lim}$). When the

concentration of this electron acceptor (C_i) exceeds its threshold, the corresponding half-reaction rate is independent of C_i. Otherwise, the rate is proportional to C_i (i.e., first-order dependence). According to the preferential order of utilization of the electron acceptors, f_1, f_2 correspond to O_2, NO_3^-, respectively. Nitrification is described by conventional second-order bimolecular reaction kinetics:

$$r_{\mathrm{NH_4^+}} = k_{\mathrm{NH_4^+}} \cdot C_{\mathrm{NH_4^+}} \cdot C_{\mathrm{O_2}} \tag{2.7}$$

where $k_{\mathrm{NH_4^+}}$ is the second-order nitrification molar rate coefficient, $C_{\mathrm{NH_4^+}}$ and $C_{\mathrm{O_2}}$ are the molar concentrations of ammonium and oxygen, respectively.

Some species play double roles in reactions, taking part not only as reactants but also as products. We define the net reaction rates of those four representative compounds from Equations (2.3) - (2.7) as follows:

$$R_{\mathrm{DOC}} = -r_{DOC} \tag{2.8a}$$

$$R_{\mathrm{O_2}} = -r_{red,1} - 2r_{\mathrm{NH_4^+}} \tag{2.8b}$$

$$R_{\mathrm{NO_3^-}} = -r_{red,2} + r_{\mathrm{NH_4^+}} \tag{2.8c}$$

$$R_{\mathrm{NH_4^+}} = -r_{\mathrm{NH_4^+}} \tag{2.8d}$$

The negative sign indicates that the reactant is consumed, and vice versa. The calculation of reaction rates for the four species reported in the Appendix A1.

The steady-state reactive solute transport through the sediment is described by:

$$\nabla \cdot \left(-\theta D \nabla C_j + q \cdot C_j\right) = \theta R_j \quad (\mathrm{j} = \mathrm{DOC}, \mathrm{O_2}, \mathrm{NO_3^-}, \mathrm{NH_4^+}) \tag{2.9}$$

Where θ is the sediment porosity, R_j (sink/source term) is the net reaction rate of the compound j, D is the hydrodynamic dispersion tensor and C_j is the molar concentration of

the species *j*, q is the specific discharge as defined in equation (2.1). The top boundary of the sediment (the SWI) for equation (2.9) is set as an open boundary. The top boundary is divided into two zones, downwelling parts are treated as a Dirichlet condition with the constant solute concentrations in the stream ($C_{s,t}= C_{s,0}$) ; upwelling parts are assigned as advective boundaries with no dispersion (zero gradient). The lateral boundaries of the sediment domain are set as periodic boundaries ($C_{s,l}=C_{s,r}$). The bottom is set as no-flow boundary.

The *D* tensor is calculated following:

$$\theta D_{ij} = \alpha_T |q| \delta_{ij} + (\alpha_L - \alpha_T) \cdot \frac{q_i q_j}{|q|} + \theta \cdot \tau D_m \delta_{ij} \quad (i, j = 1,2) \qquad (2.10)$$

where *i, j*=1, 2, α_L and α_T are transverse and longitudinal dispersivities, τ is the tortuosity factor, δ_{ij} is the Kronecker delta function, and D_m is the molecular diffusion coefficient in porous media. α_L is set to be 3 cm (several grain diameters for sand), and α_T is considered to be $\alpha_L/10$.

Here, we assume that the stream water is well-mixed such that the concentration of four species at the top boundary of the sediment is constant. To study the effect of temperature on the nutrient cycling on the HZ, we employed two cases with different in-stream species concentrations following *Bardini et al.* [2012]. The concentrations of the four components are listed in Table 2.2.

2.3.4 Temperature-dependent kinetics and hydraulic parameters

The influence of temperature on biochemical reaction kinetics has been proposed to follow the Arrhenius law [*Dawson and Murphy*, 1972] (see Figure 2.2):

$$k(T) = Ae^{-E/RT} \tag{2.11}$$

where $k(T)$ is the reaction rate constant at some temperature T, A is the pre-exponential factor, E is the activation energy of the reaction, and R is the ideal gas constant. For many biochemical reactions, within the appropriate temperature range, the reaction rates could double with a 10 °C temperature increase [*Veraart et al.*, 2011]. The Arrhenius equation can be modified to consider temperature changes, resulting in:

$$k(T_1) = k(T_2)e^{-\frac{E}{R}\left(\frac{1}{T_1}-\frac{1}{T_2}\right)} \tag{2.12}$$

From equations 2.11 and 2.12, the reaction rate constant at any given temperature can be determined. In this study, we assume that aerobic respiration and nitrification follow an Arrhenius relationship between 5°C and 35°C. Activation energies for aerobic respiration (E_1) and nitrification (E_2) in this study are 60 kJ/mol [*Thamdrup et al.*, 1998; *Yvon-Durocher et al.*, 2012] and 162 kJ/mol [*Sheibley et al.*, 2003], respectively (Table 2.3).

Additionally, the density (ρ) and viscosity (μ) of water are temperature-dependent. Both ρ and μ decrease with increasing temperature, but the influence of temperature on ρ can typically be ignored for the temperature range we considered in this study (5°C to 35°C which translates to a 0.6% decrease in ρ), especially compared to the influence on dynamic viscosity. Since $K_h = k_p \rho g/\mu$, where K_h is the hydraulic conductivity, k_p is the intrinsic permeability, g is the acceleration of gravity, temperature variation affects pore water flow via an effect on K_h. For example, because of decreasing μ with increasing T, the value of K_h doubles when the temperature is increased from 0°C to 25°C [Birgand et al., 2007.]. The viscosity dependence on temperature follows a

polynomial function [*Cardenas and Wilson*, 2007b; *Schmidt*, 1979]:

$$\mu(T) = a - bT + cT^2 - dT^3 + eT^4 \quad (2.13)$$

The coefficients above are a=0.00179, b=5.942×10^{-5}, c=1.286×10^{-6}, d=1.623×10^{-8}, and e=8.665×10^{-11}.

2.3.5 Numerical modeling implementation

The above conceptual model with hydrodynamic and chemical processes is implemented in a generic finite-element software, COMSOL Multiphysics. The sediment domain is discretized into ~200,000 triangular elements. To capture the physical and chemical processes occurring at the SWI, we used a refined mesh (~0.005 mm spacing) close to the top boundaries, and relatively much coarser elements (~1 mm) within the domain. Additionally, we utilize the boundary layer mesh functionality in COMSOL to further ensure the accuracy of results from the boundary and moving away from it. The numerical results have been tested to be insensitive to the mesh size.

We implemented a parametric modeling approach in COMSOL with increasing temperature from 5°C to 35°C. The implementation of numerical models are also carried out with two cases that represent different in-stream water quality (Table 2.2). The values of all model input parameters are presented in Table 2.3.

Table 2.1: Chemical reactions considered in the simulations

Reaction type& index	Reaction	β
Aerobic respiration (r1)	$CH_2O + O_2 \rightarrow CO_2 + H_2O$	1
Denitrification （r2）	$5CH_2O + 4NO_3^- + 4H^+ \rightarrow 5CO_2 + 2N_2 + 7H_2O$	0.8
Nitrification (r3)	$NH_4^+ + 2O_2 \rightarrow NO_3^- + 2H^+ + H_2O$	---

Table 2.2: In-stream concentration of species

Case	[DOC] (mg/L)	[O_2] (mg/L)	[NO_3^-] (mg/L)	[NH_4^+] (mg/L)	[NO_3^-]/[NH_4^+]
Polluted Stream	150	10	8	5	1.6
Pristine Stream	50	10	1	0.05	20

Table 2.3: Summary of input parameters for the reactive transport models

Symbol	Unit	Value	Description
D_m	[m^2/s]	1×10^{-10}	Molecular Diffusion coefficient
θ	[-]	0.4	Porosity
τ	[-]	$\theta^{1/3}$	Tortuosity
$\beta 1$	[-]	1	Ratio of transferred electrons for O_2
$\beta 2$	[-]	0.8	Ratio of transferred electrons for NO_3^-
$[O_2]_{lim}$	mg/L	1	Oxygen limiting concentration
$[NO_3^-]_{lim}$	mg/L	0.5	Nitrate limiting concentration
k_{NH4+}	L/(mg·s)	5×10^{-6}	Second-order nitrification molar rate coefficient at temperature 20°C
k_{DOC}	1/s	5×10^{-6}	DOC decay constant at temperature 20°C
R	J/(K·mol)	8.31	Gas constant
$E1$	kJ/mol	60	Activation energy for aerobic respiration
$E2$	kJ/mol	162	Activation energy for nitrification

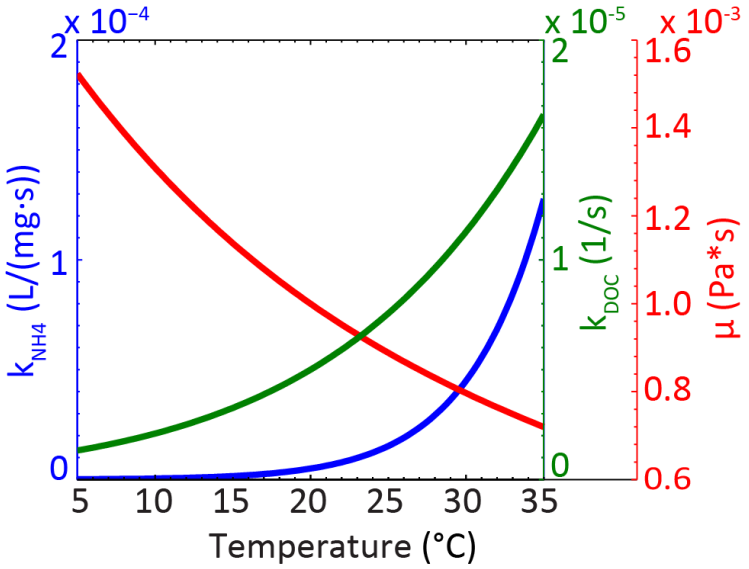

Figure 2.2: Temperature-dependent parameters: Arrhenius relationship between reaction rate constant of respiration (k_{DOC}) and denitrification (k_{NH4})and temperature; viscosity (μ) decreases with temperature.

2.3.6 Definition of N transformation reaction rates

The spatially averaged reaction rates are calculated by integrating the distributed reaction rates over the whole sediment domain and then dividing by the area of the HZ:

$$\overline{r_{NI}} = \frac{1}{A}\int \theta \cdot \mathrm{r}_{\mathrm{NH}_4^+} \cdot \mathrm{dA} \tag{2.14a}$$

$$\overline{r_{DN}} = \frac{1}{A}\int \theta \cdot r_{red,2} \cdot \mathrm{dA} \tag{2.14b}$$

$$\overline{r_{netDN}} = \frac{1}{A}\int \theta \cdot R_{\mathrm{NO}_3^-} \cdot \mathrm{dA} \tag{2.14c}$$

Negative net denitrification values ($\overline{r_{netDN}}$) indicate that the amount of nitrate consumption through denitrification is greater than the amount of nitrate production from nitrification, and vice versa.

2.4 RESULTS

2.4.1 Temperature effect on the flow field and interfacial fluxes

The hyporheic flow fields at different temperatures are nearly the same (Figures 2.3 and 2.4), which shows that temperature hardly has an effect on the flow kinematics. Since the effect of temperature on fluid flow is through temperature-dependent viscosity (i.e., equation 2.13) and therefore hydraulic conductivity, as a result, the calculated interfacial flux over the SWI changes from 1.7×10^{-9}m^2/s at T= 5°C to 3.6×10^{-9}m^2/s at T= 35°C (Table 2.4). Although temperature has a measurable effect on the interfacial fluid flux, it expectedly only affects the velocity magnitude, and does not alter the general flow pattern (Figures 2.3 and 2.4). However, temperature would affect the nutrient cycling in hyporheic zones through the supply rate of solutes, i.e., it affects the reaction rates due to

more availability of reactants because of increased hyporheic advection.

To analyze the effects of temperature on the nutrient supply rate, we calculated the total interfacial flux of nitrate into ($[NO_3^-]_{in}$) and out of ($[NO_3^-]_{out}$) the HZ. For the polluted stream case, $[NO_3^-]_{in}$ increases until it peaks at 25°C, then decreases with even higher temperature (Table 2.4). The temperature effect on $[NO_3^-]_{in}$ is less than one order of magnitude variation from 5°C to 35°C (Table 2.4). $[NO_3^-]_{out}$ increases monotonically with temperature. For the pristine stream case, both $[NO_3^-]_{in}$and $[NO_3^-]_{out}$ always increase with increasing temperature (Table 2.5). The main difference between these two cases is the relative abundance of ammonium and nitrate; $[NO_3^-]/[NH_4^+]$ of the polluted stream case is 1.6, while $[NO_3^-]/[NH_4^+]$ of the pristine stream case is 20 (Table 2.2).

Table 2.4: Summary of simulation results for the polluted stream case

T (°C)	HZ flux (m^2/s)	$[NO_3]_{in}$ mg/(m·s)	$[NO_3]_{out}$ mg/(m·s)	$[NO_3]_{advin}$ mg/(m·s)	$[NO_3]_{dspout}$ mg/(m·s)	$\overline{r_{NI}}$ mg/(m^3·s)	$\overline{r_{DN}}$ mg/(m^3·s)	$\overline{r_{netDN}}$ mg/(m^3·s)	N_A mg/(m·s)	N_{RE}
5	9.4×10^{-7}	-7.6×10^{-3}	4.4×10^{-3}	-7.5×10^{-3}	9.9×10^{-5}	3.5×10^{-4}	4.2×10^{-3}	-3.9×10^{-3}	-3.2×10^{-3}	42.4%
10	1.1×10^{-6}	-8.8×10^{-3}	4.8×10^{-3}	-8.7×10^{-3}	1.5×10^{-4}	8.6×10^{-4}	5.7×10^{-3}	-4.8×10^{-3}	-4.0×10^{-3}	45.8%
15	1.3×10^{-6}	-1.0×10^{-2}	5.2×10^{-3}	-1.0×10^{-2}	2.9×10^{-4}	1.9×10^{-3}	7.7×10^{-3}	-5.8×10^{-3}	-4.9×10^{-3}	48.5%
20	1.4×10^{-6}	-1.1×10^{-2}	5.6×10^{-3}	-1.1×10^{-2}	6.5×10^{-4}	3.7×10^{-3}	1.0×10^{-2}	-6.6×10^{-3}	-5.5×10^{-3}	49.9%
25	1.6×10^{-6}	-1.2×10^{-2}	6.0×10^{-3}	-1.3×10^{-2}	1.5×10^{-3}	6.8×10^{-3}	1.4×10^{-2}	-6.7×10^{-3}	-5.6×10^{-3}	48.5%
30	1.8×10^{-6}	-1.1×10^{-2}	6.6×10^{-3}	-1.4×10^{-2}	3.6×10^{-3}	1.2×10^{-2}	1.7×10^{-2}	-5.3×10^{-3}	-4.5×10^{-3}	40.5%
35	2.0×10^{-6}	-8.4×10^{-3}	7.5×10^{-3}	-1.6×10^{-2}	7.9×10^{-3}	2.0×10^{-2}	2.1×10^{-2}	-1.1×10^{-3}	-9.0×10^{-4}	10.7%

Table 2.5: Summary of simulation results for the pristine stream case

T(°C)	HZ flux (m^2/s)	$[NO_3]_{in}$ mg/(m·s)	$[NO_3]_{out}$ mg/(m·s)	$[NO_3]_{advin}$ mg/(m·s)	$[NO_3]_{dspout}$ mg/(m·s)	$\overline{r_{NI}}$ mg/(m^3·s)	$\overline{r_{DN}}$ mg/(m^3·s)	$\overline{r_{netDN}}$ mg/(m^3·s)	N_A mg/(m·s)	N_{RE}
5	9.4×10^{-7}	-9.5×10^{-4}	6.9×10^{-4}	-9.4×10^{-4}	7.8×10^{-6}	9.4×10^{-6}	3.3×10^{-4}	-3.2×10^{-4}	-2.7×10^{-4}	28.3%
10	1.1×10^{-6}	-1.1×10^{-3}	7.4×10^{-4}	-1.1×10^{-3}	1.1×10^{-5}	2.4×10^{-5}	4.6×10^{-4}	-4.4×10^{-4}	-3.7×10^{-4}	33.1%
15	1.3×10^{-6}	-1.3×10^{-3}	8.0×10^{-4}	-1.3×10^{-3}	1.5×10^{-5}	5.6×10^{-5}	6.2×10^{-4}	-5.7×10^{-4}	-4.8×10^{-4}	37.3%
20	1.4×10^{-6}	-1.4×10^{-3}	8.6×10^{-4}	-1.4×10^{-3}	2.1×10^{-5}	1.1×10^{-4}	8.2×10^{-4}	-7.1×10^{-4}	-5.9×10^{-4}	40.9%
25	1.6×10^{-6}	-1.6×10^{-3}	9.1×10^{-4}	-1.6×10^{-3}	3.4×10^{-5}	1.9×10^{-4}	1.0×10^{-3}	-8.5×10^{-4}	-7.1×10^{-4}	44.0%
30	1.8×10^{-6}	-1.8×10^{-3}	9.5×10^{-4}	-1.8×10^{-3}	6.3×10^{-5}	2.8×10^{-4}	1.3×10^{-3}	-9.9×10^{-4}	-8.3×10^{-4}	46.4%
35	2.0×10^{-6}	-1.9×10^{-3}	1.0×10^{-3}	-2.0×10^{-3}	1.2×10^{-4}	4.0×10^{-4}	1.5×10^{-3}	-1.1×10^{-3}	-9.2×10^{-4}	48.0%

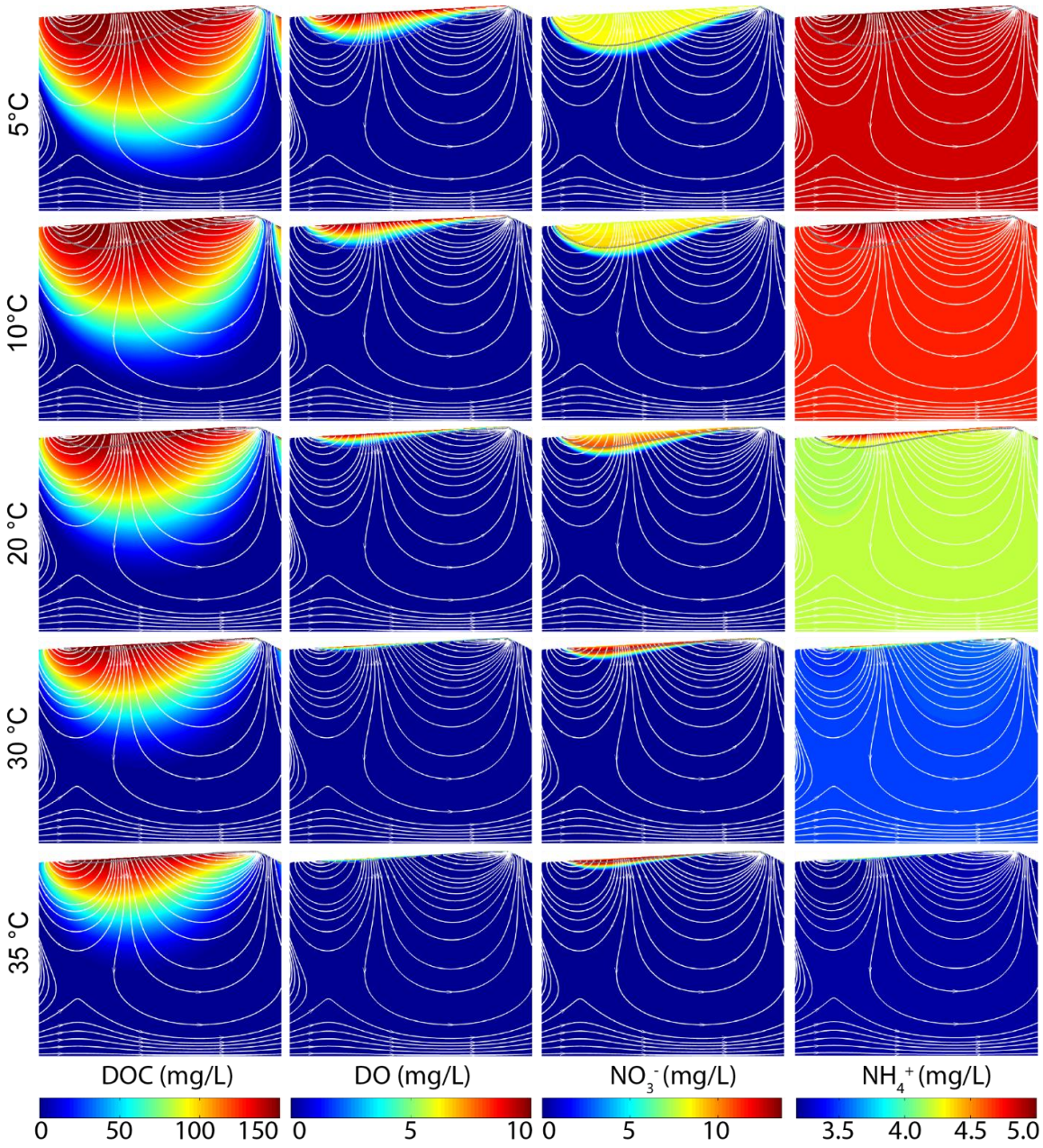

Figure 2.3: Solute spatial distribution with varying temperatures for the polluted stream case. Channel flow is from left to right. White lines with arrows indicate streamlines. Dotted gray lines indicate the oxic-anoxic boundary ($[O_2]_{lim}$=1mg/L). The domain is 1 m wide.

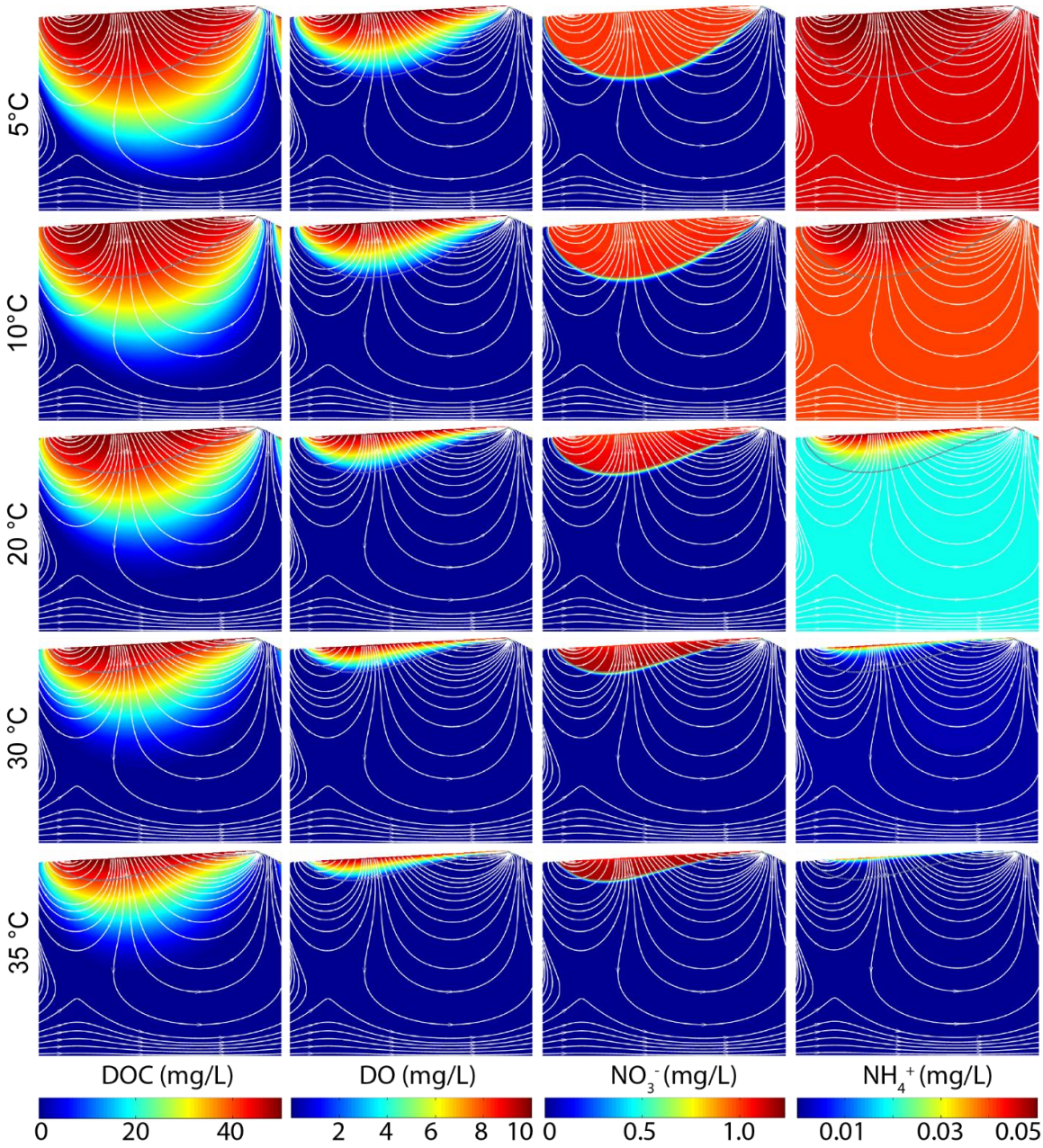

Figure 2.4: Solute spatial distribution with varying temperatures for the pristine stream case. Channel flow is from left to right. White lines with arrows indicate streamlines. Dotted gray lines indicate the oxic-anoxic boundary. The domain is 1 m wide.

2.4.2 Temperature effect on nutrient distribution

The resultant spatial distributions of the four N species at steady state are shown in Figure 2.3 (polluted stream case) and Figure 2.4 (pristine stream case). DOC, DO and NH_4^+ concentrations, which are set by the boundary condition at the SWI, decrease with depth for both cases. The solute fronts are similar in shape but different in size, i.e., they all have a parabolic shape and front and the deepest portion is located at the divide of two counter-flowing advective flow cells (i.e., near the stagnation point). The smooth solute concentration fronts imply that dispersion plays an important role for delivering and distributing solutes into the HZ.

NO_3^- displays a different behavior relative to the other three species, with the maximum concentration just above the oxic-anoxic zone boundary (Figures 2.3 and 2.4). This is because nitrification occurs in the oxic zone with the nitrate produced advected downwards further along the hyporheic flow path, whereas the removal of nitrate through denitrification begins only when oxygen is depleted or drops below the limiting concentration. In this study, the DO limiting concentration of 1 mg/L is defined as the oxic-anoxic boundary. In short, nitrification prevails above the oxic-anoxic boundary occurring in the shallow sediment, while denitrification dominates below the oxic-anoxic boundary in the deep sediment. In addition, the NO_3^- front is steeper than the DOC, DO and NH_4^+ concentration fronts. This is because additional nitrate is supplied from nitrification, which is then removed by denitrification very quickly, thus spatially constraining the denitrification zone.

Additionally, the penetration depth of NO_3^- is barely deeper than the oxygen

penetration depth at the same temperature. The main difference between the two water quality scenarios is that the concentration front of NO_3^- in the pristine stream case (Figure 42.) is sharper and penetrates deeper than that of the polluted stream case (Figure 2.3). This shows that below the oxic zone, NO_3^- is quickly consumed. But in the pristine stream case, oxygen is consumed slowly thus allowing for deeper penetration of NO_3^-. For the polluted stream case, due to the high concentration of DOC and NH_4^+, oxygen is quickly consumed, and thus the NO_3^- does not make it to greater depths since denitrification occurs at shallower depths.

The DOC concentration in both water quality scenarios is relatively high; DOC is not the limiting reactant. Thus, aerobic respiration would primarily be limited by the oxygen supply rate. The availability of DOC would therefore have minimal effect on the fate of oxygen, and consequently is less relevant to the denitrification rates in our study. For the same temperature, as expected, the penetration depth of DOC is deeper than those of DO and NO_3^- at steady state (Figures 2.3 and 2.4). Due to the high DOC concentration, DO always becomes depleted at a certain depth due to respiration and nitrification. Any ammonium that is not nitrified in the oxic zone is simply transported further along the hyporheic flow paths (Figures 2.3 and 2.4).

The fate of the different solutes is affected differently by temperature. In general, the penetration depths of all solutes considered decreased with increasing temperature (Figure 2.3 and 2.4) due to the consumptive biogeochemical reaction rates increasing with temperature. In particular, the oxic zone became shallower and narrower as temperature increased. The oxic-anoxic boundary moved up from ~8 cm depth at 5°C to

~1 cm at 35°C for the polluted stream case (Figure 2.3), and from ~21 cm at 10°C to ~ 5 cm at 35°C for the pristine stream case (Figure 2.4). This is a clear consequence of aerobic respiration and nitrification rates increasing with temperature (Figure 2.2). The reactions rates are analyzed in more detail below.

2.4.3 Temperature effect on reaction rates

The spatial patterns of nitrification, denitrification and net denitrification rates for the polluted and pristine cases (Figures 2.5 and 2.6) further illustrate that nitrification prevails in the oxic zone and that denitrification dominates in the anoxic zone. The nitrification rate has its maximum value near the SWI due to the abundance of NH_4^+ and O_2, but it declined with depth due to the depletive consumption of both reactants. Moreover, the denitrification rate peaked right below the oxic-anoxic boundary, and dropped sharply with depth afterwards, thus leading to a very narrow but pronounced denitrification zone. Both nitrification and denitrification reaction area decrease by about 5~10 times as the temperature increases from 5°C to 35°C (Figures 2.5 and 2.6).

Both nitrification and denitrification processes are sensitive to temperature variation (Figure 2.5). For the polluted stream case, the maximum nitrification rate increased from 2.7×10^{-2} mg/(m^3·s) at 5°C to 2.7×10^{1} mg/(m^3·s) at 35°C, roughly a thousand-fold increase. Moreover, the maximum denitrification rate increased from

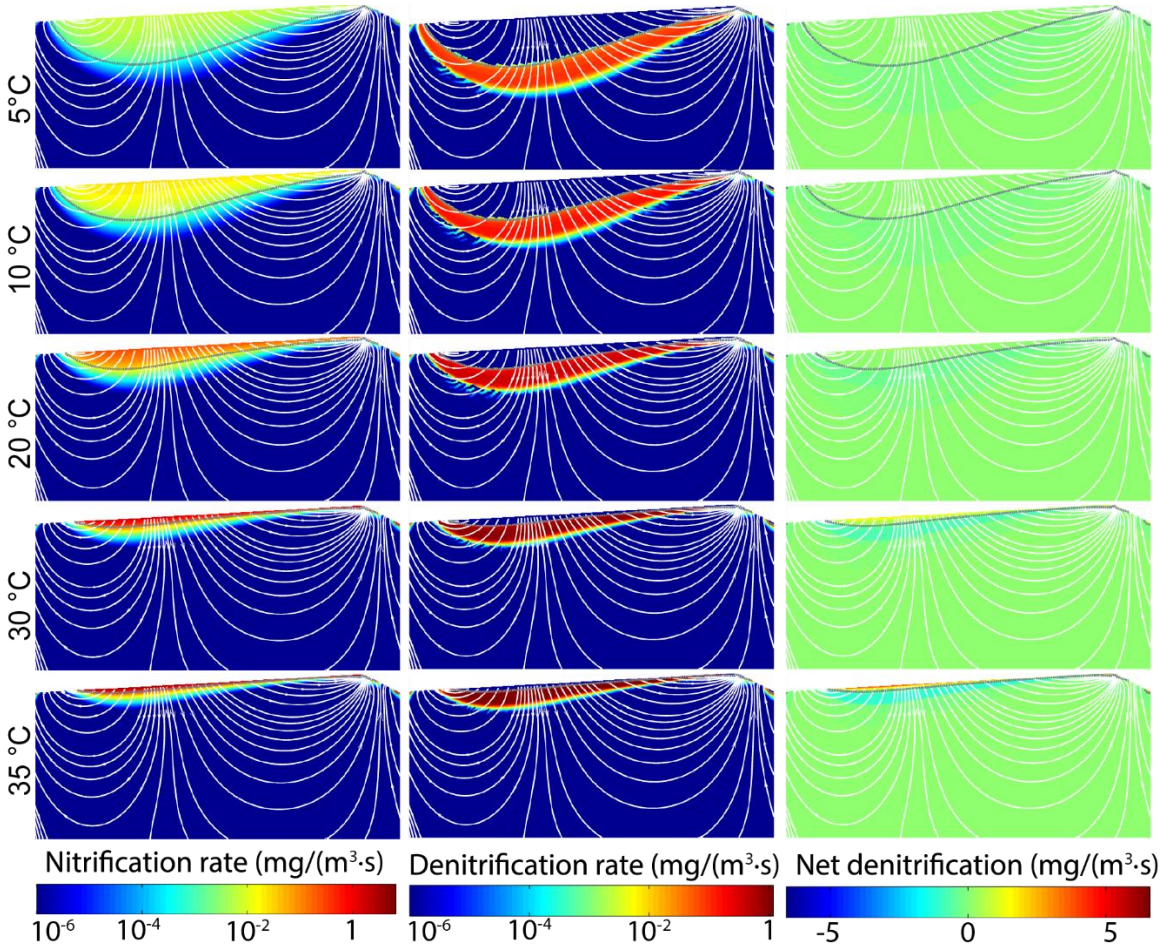

Figure 2.5: Distribution of nitrification, denitrification and net denitrification rates with varying temperatures for the polluted stream case. Channel flow is from left to right. White lines with arrows indicate streamlines. Dotted gray lines indicate the oxic-anoxic boundary. The domain is 1 m wide. Since chemical reactions are limited to the top part, the graph is cut to show the top 0.5m.

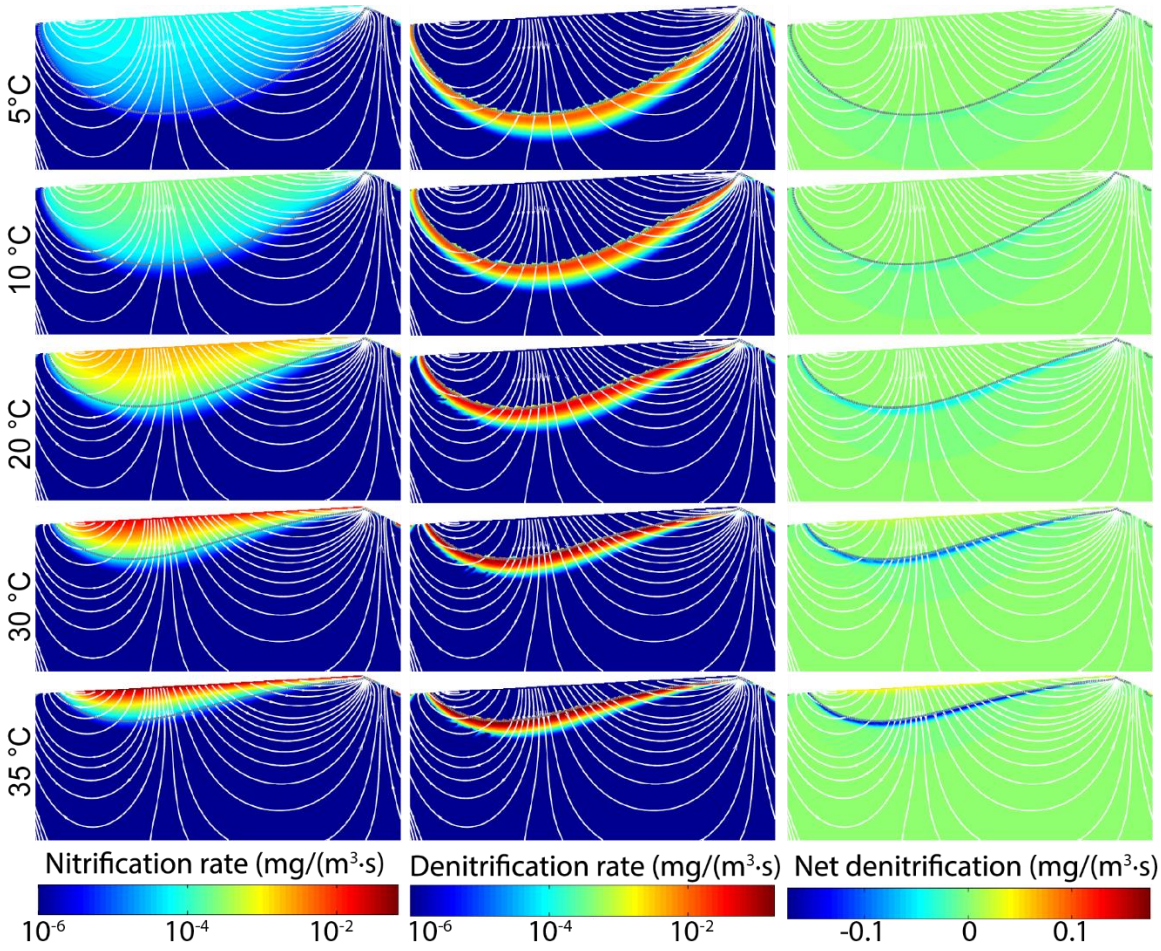

Figure 2.6: Distribution of nitrification, denitrification and net denitrification rates with varying temperatures for the pristine stream case. Channel flow is from left to right. White lines with arrows indicate streamlines. Dotted gray lines indicate the oxic-anoxic boundary. The domain is 1 m wide, the depth is 0.5m.

3.0×10^{-1} mg/(m^3·s) at 5°C to 3.9 mg/(m^3·s) at 35°C (Figure 2.5), which is a ten-fold increase. However, the overall denitrification zone became shallower from a depth of ~8 cm at 5°C to ~ 1 cm at 35°C; the nitrification and oxic zones moved up correspondingly (Figure 2.5). For the pristine stream case, the maximum nitrification rate increased from 2.7×10^{-4} mg/(m^3·s) at 5°C to 2.8×10^{-1} mg/(m^3·s) at 35°C; this is still around a thousand-fold increase but the rates were relatively and generally much lower than the polluted case. The maximum denitrification rate increased from 4.8×10^{-2} mg/(m^3·s) at 5°C to 5.8 $\times10^{-1}$ mg/(m^3·s) at 35°C (Figure 2.6), which is once again roughly a ten-fold increase. Similar to the polluted stream case, the denitrification zone became shallower from a depth of ~21 cm at 5°C to ~ 5 cm at 35°C. The nitrification and oxic zones moved upwards correspondingly.

To further analyze the overall temperature effect on the key chemical reactions over the whole HZ, we evaluated the spatially averaged value for nitrification rate $\overline{r_{NI}}$, denitrification rate $\overline{r_{DN}}$, and net denitrification rate $\overline{r_{netDN}}$, as defined in equation 2.14. The polluted stream case $\overline{r_{NI}}$ increased from 3.5×10^{-4} mg/(m^3·s) at 5°C to 2.0×10^{-2} mg/(m^3·s) at 35°C; $\overline{r_{DN}}$ increased from 4.2×10^{-3} mg/(m^3·s) at 5°C to 2.1×10^{-2} mg/(m^3·s) at 35°C; $\overline{r_{netDN}}$ became more negative from -3.9×10^{-3} mg/(m^3·s) at 5°C to -6.6×10^{-3} mg/(m^3·s) at 25°C and then increased to -1.1×10^{-3} mg/(m^3·s) at 35°C (Table 2.4). A negative value for $\overline{r_{netDN}}$ means denitrification is dominant in the HZ; the HZ consumes nitrate and is a nitrate sink. Additionally, for the pristine stream case, $\overline{r_{NI}}$ increased from 9.4×10^{-6} mg/(m^3·s) at 5°C to 4.0×10^{-4} mg/(m^3·s) at 35°C; $\overline{r_{DN}}$ increased from 3.3×10^{-4} mg/(m^3·s) at 5°C to 1.5×10^{-3} mg/(m^3·s) at 35°C; $\overline{r_{netDN}}$ became more negative from -

3.2×10^{-4} mg/(m^3·s) at 5°C to -1.1×10^{-3} mg/(m^3·s) at 35°C (Table 2.5). In summary, the temperature effect on nitrification is nearly a two order-of-magnitude increase, and on denitrification is a one order-of-magnitude increase, from 5°C to 35°C (Tables 2.4 and 2.5).

There are numerous confounding and interacting factors that ultimately combine to lead to the final temperature-dependence of reaction rates. First, equations 2.3 and 2.7 dictate that the resulting reaction rate is a function of both the rate constants (which are temperature dependent) and the concentration of reactants. Following the Arrhenius equation (equation 2.11), K_{NH4} increases from 1.38×10^{-7} L/(mg·s) at 5°C to 1.27×10^{-4} L/(mg·s) at 35°C, roughly a thousand-fold increase (Figure 2.2). Likewise, K_{DOC} increases from 1.32×10^{-6} (1/s) at 5°C to 1.66×10^{-5} (1/s) at 35°C, nearly a ten-fold increase (Figure 2.2). As mentioned above and secondly, temperature also has an effect on the interfacial fluid flux which roughly doubles from $9.4\times10^{-7}m^2/s$ at T= 5°C to 2.0 $\times10^{-6}m^2/s$ at T= 35°C (Table 2.4). Additionally, spatially averaged reaction rates are obviously affected by the spatial extent over which the reactions takes place. We found that reaction area decreases with increasing temperature, with nearly a 10-20 times reduction for nitrification area and ~2 times reduction for denitrification area (Figures 2.5 and 2.6). Furthermore and finally, nitrification, denitrification, and aerobic respiration occur simultaneously. One species (i.e., NO_3^-) can be both a reactant and product in different reactions. This further complicates the sensitivities of reaction rates to temperature. As to the relative importance of these factors on reaction rates, the temperature effect on the rate constant can be considered as the dominant factor.

However, the temperature effect on maximum reaction rates and spatially averaged reaction rates cannot be anticipated and exactly predicted by the Arrhenius equation.

2.5 DISCUSSION

2.5.1 Temperature effect on hyporheic NO_3^- removal ability and efficiency

We employed NO_3^- removal or production ability (N_A), and its associated efficiency (N_{RE}) as two metrics to evaluate the HZ functionality as a NO_3^- source or sink, and to estimate the HZ efficiency in N transformation, respectively. The net denitrification rate over the HZ, N_A, which also integrates the coupled nitrification-denitrification process on the mass change rate of nitrate, is defined as:

$$N_A = \int R_{NO_3^-} \cdot \mathrm{dA} \qquad (2.15)$$

where $N_A < 0$ implies the HZ is a net denitrifying system, in which denitrification dominates over nitrification; and thus the HZ serves as a nitrate sink. When $N_A > 0$, it implies the HZ is a net nitrifying system, where nitrification dominates over denitrification; and thus the HZ is a nitrate source. The magnitude of N_A indicates the extent of nitrate removal or production in the HZ.

Both nitrification and denitrification reaction rates increase as temperature increases from 5°C to 35°C, while nitrification reaction area decreases 10~20 times, denitrification reaction area decreases ~2 times (Figures 2.5 and 2.6). Spatially averaged nitrification rate ($\overline{r_{NI}}$) increases nearly a hundred times, while denitrification ($\overline{r_{DN}}$) increases less than 10 times, and net denitrification ($\overline{r_{netDN}}$) showed a ten-fold change from 5°C to 35°C (Tables 2.4 and 2.5). If reaction area was kept constant, $\overline{r_{NI}}$ would have to increase

nearly a thousand times, $\overline{r_{NI}}$ would be larger than $\overline{r_{DN}}$, and nitrification would dominate over denitrification at higher temperature. N_A would have to change from negative values (nitrate sink) at low temperature to positive at high temperature (nitrate source). This implies that reaction area also has a compensating effect on the spatially averaged reaction rates and N_A.

N_{RE} is a dimensionless number that compares reaction and supply rates [*Zarnetske et al.*, 2012] and is defined as:

$$N_{RE} = \begin{cases} \dfrac{|N_A|}{|[NO_3^-]_{in}|}, & N_A < 0 \\ \dfrac{-|N_A|}{[NO_3^-]_{in} + |N_A|}, & N_A \geq 0 \end{cases} \tag{2.16}$$

where $[NO_3^-]_{in}$ is the total influx of NO_3^- into the HZ. Similar to N_A, N_{RE} is a useful dimensionless metric describing whether the HZ is a nitrate source or sink. The range of N_{RE} is between 0 and 1 if the HZ is a nitrate sink with larger values indicating higher removal efficiency, where denitrification is dominant over nitrification. If the HZ is a nitrate source, N_{RE} ranges from -1 to 0 with more negative values signifying more nitrate is being produced in the HZ rather than being carried into the HZ across the SWI.

For the polluted stream case, the N_A increased with temperature until it peaked at 25°C, and then decreased with increasing temperature; the N_{RE} increased from 42.4% at 5°C to 49.9% (maximum) at 20°C, then decreased to 10.7% at 35°C (Table 2.4). However, for the pristine stream case, both N_A and N_{RE} increased with increasing temperature, the N_{RE} changed from 28.3% at 5°C to 48.0% at 35°C (Table 2.5). The temperature effects on N_A and N_{RE} are different.

To further explain the different trends in N_A and N_{RE} with temperature, we scrutinized the terms in equation (2.15). For $[NO_3^-]_{in}$, we expect that it should increase as the temperature increases because the interfacial flux across the SWI increases when the temperature goes up (Tables 2.4 and 2.5). However, the $[NO_3^-]_{in}$ increases at first, reaches its maximum value around 25°C, and then eventually decreases on with even higher temperatures for the polluted stream case (Table 2.4). This is because the nitrification rate increases with temperature at the oxic zone (i.e., near the top of sediment), resulting in the production of a relatively large amount of NO_3^- in the upper part of the HZ (Figure 2.5). This would suppress the amount of NO_3^- entering the HZ by increasing the dispersive flux out from the SWI ($[NO_3^-]_{dspout}$), where the incremental increase in $[NO_3^-]_{dspout}$ is larger than the incremental increase of advective flux of NO_3^- into the sediment ($[NO_3^-]_{advin}$) resulting from temperature change (which in turn is due to increased hydraulic conductivity due to viscosity effects) as the temperature is higher than 25°C (Table 2.4). For example, as the temperature increased from 25°C to 30°C , $[NO_3^-]_{dspout}$ increased from 1.5×10^{-3} mg/(m·s) to 3.6×10^{-3} mg/(m·s); its net increase is 2.1×10^{-3} mg/(m·s). $[NO_3^-]_{advin}$ increased from 1.3×10^{-2} mg/(m·s) to 1.4×10^{-2} mg/(m·s); its net increase is 1.0×10^{-3} mg/(m·s) which is smaller than that of $[NO_3^-]_{dspout}$ (Table 2.4).

The trend of $[NO_3^-]_{in}$ in the pristine stream case, where it monotonically increased with increasing temperature (Table 2.5), is very different from that of the polluted stream case. Even though the NO_3^- production increased with temperature (Table 2.5), which should consequently inhibit the amount of nitrate entering into the HZ by enhancing

$[NO_3^-]_{dspout}$, the incremental increase in $[NO_3^-]_{dspout}$ did not compensate for the incremental increase in $[NO_3^-]_{advin}$ due to the temperature change (Table 2.5).

As for N_A, for the polluted stream case, N_A increased initially and dropped off later on with further increasing temperature (Tables 2.4). For the pristine stream case, N_A monotonically increased with increasing temperature. In fact, both nitrification and denitrification rates rose as temperature went up (Tables 2.4 and 2.5). Because the relative concentration of NH_4^+ compared to NO_3^- is higher in the polluted stream case (Table 2.2), the nitrification rate is more sensitive to temperature in the polluted case than in the pristine case.

We surmise that the difference in trends in N_A and N_{RE} with increasing temperatures can be ascribed to the differing availability of NH_4^+ and NO_3^- (Tables 2.4 and 2.5). This is a natural result of equation (2.7) which assumes direct and strong dependence of the nitrification rate on $[NH_4^+]$. Additionally, since DOC is present in sufficient amounts in both water quality scenarios, the denitrification rate is also highly sensitive to NO_3^- availability following equations (2.4-2.6). Therefore, the change in nitrification and denitrification rates are largely dependent on the relative amount of nitrate and ammonium. In order to further test this interpretation, we carried out a sensitivity analysis of varying $[NO_3^-]/[NH_4^+]$ and analyze its impact on N_A and N_{RE}.

2.5.2 Sensitivity analysis of $[NO_3^-]/[NH_4^+]$ to nitrate removal and production efficiency

We implemented two sensitivity analyses by varying the ratio $[NO_3^-]/[NH_4^+]$ based on the initial concentration of both polluted and pristine cases (Table 2.2),

respectively. Since we hypothesize that the relative amount of NO_3^- and NH_4^+ could affect the dependence of N_A and N_{RE} on temperature, we changed either $[NO_3^-]$ or $[NH_4^+]$ to alter the ratio ($[NO_3^-]/[NH_4^+]$). However, since the results were not sensitive to what species concentration is changing (results are not shown here), for simplicity, we only show results from changing $[NH_4^+]$ for both sensitivity cases, and we kept $[NO_3^-]$ constant.

In the sensitivity analysis, the logarithm of ($[NO_3^-]/[NH_4^+]$) ranged from -1 to 1 (Figure 2.7) in both cases, as the $[NH_4^+]$ was increased from 0.8 mg/L to 80 mg/L for the polluted stream sensitivity study, while the $[NH_4^+]$ was increased from 0.1 mg/L to 10 mg/L for the pristine stream sensitivity analysis. The temperature, as previously, was increased from 5 °C to 35°C. For both stream cases, area-integrated nitrification, and denitrification over the HZ increased as temperature increased (Figure 2.7). However, at higher $[NO_3^-]/[NH_4^+]$ ratio, N_A was negative (denitrification dominant), and its absolute value increased initially, but reached its maximum value at a temperature then dropped off with further increasing temperature. That is, the maximum nitrate removal rate occurs at higher $[NO_3^-]/[NH_4^+]$ ratio and moderate temperature. In addition, the optimal temperature for the maximum nitrate removal rate increased with the $[NO_3^-]/[NH_4^+]$ ratio. At lower $[NO_3^-]/[NH_4^+]$ ratio, for the polluted stream, N_A changed from negative value to positive value; for the pristine stream, N_A was positive across the entire temperature range (nitrification dominant), and its value increased as temperature increased. This supports our hypothesis that $[NO_3^-]/[NH_4^+]$ ratio is also an important factor affecting the temperature effect on nitrate removal ability (N_A) In the HZ.

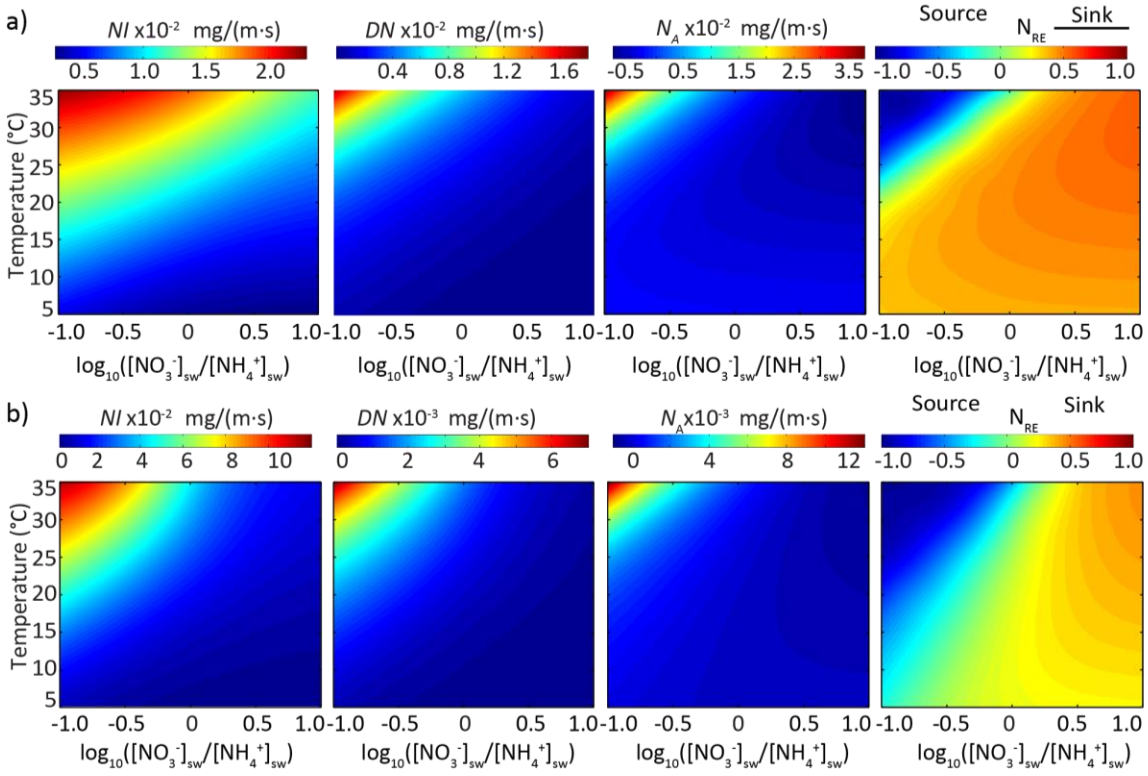

Figure 2.7: Results of sensitivity analysis for removal efficiency N_{RE} with different ratios of $[NO_3^-]$ to $[NH_4^+]$ for (a) polluted and (b) pristine stream cases.

With regard to N_{RE}, for both cases, at high $[NO_3^-]/[NH_4^+]$, the HZ functioned as a NO_3^- sink ($0< N_{RE} <1$), and the nitrate removal efficiency increased with increasing temperature (Figure 2.7). At lower $[NO_3^-]/[NH_4^+]$, the HZ behaved differently for the two scenarios. For the polluted stream, the HZ is a NO_3^- sink at low temperature, but then switched to a NO_3^- source ($-1< N_{RE} <0$) as temperature went up. However, for the pristine stream, the HZ was always a NO_3^- source, and the NO_3^- production efficiency increased as temperature increased.

For both cases, there is a transitional range of $[NO_3^-]/[NH_4^+]$ where N_{RE} is very close to 0, and thus it may fluctuate about 0, potentially causing the switching of HZ source-sink functionality with subtle temperature changes. The concentration ratio of the polluted stream case lies within the transitional range of $[NO_3^-]/[NH_4^+]$ (Table 2.2), therefore the results are consistent with what the sensitivity analysis revealed. That is the N_{RE} increased first as temperature went up, reached a maximum value, and then began to decline with further increasing temperature. Although the absolute ranges for the NO_3^- sink zone, the transition zone, and the NO_3^- source zone are different in these two sensitivity cases (Figure 2.7), the similar overall trend supports our interpretation of strong dependence on the $[NO_3^-]/[NH_4^+]$ ratio. This highlights the important contribution of $[NO_3^-]/[NH_4^+]$ to the influence of temperature on N_{RE}.

The sensitivity analysis (Figure 2.7) further illustrates the importance and interacting effects of stream temperature and stream water quality on HZ NO_3^- removal and production efficiency. It also revealed the important role of the relative supply of NH_4^+ compared to that of NO_3^- on N_A and N_{RE}.

2.5.3 Biogeochemical and ecological implications

Many previous studies have shown that hyporheic temperatures vary both temporally and spatially due to daily and seasonal changes in stream temperature and hyporheic exchange patterns [*Cardenas and Wilson*, 2007c; *Marzadri et al.*, 2013; *Norman and Cardenas*, 2014; *Sharma et al.*, 2012]. The results of our sensitivity analysis (Figure 2.7) indicate that during warmer temperatures, such as in summer at the seasonal scale or during daytime at the daily scale, nitrate removal (or production) efficiency would be higher compared to that in winter or at night. Whether the hyporheic zone acts as a nitrate source or sink also depends strongly on the $[NO_3^-]/[NH_4^+]$ of stream water. At high ratios, the HZ functions as a NO_3^- sink, nitrate removal efficiency increases as the temperature goes up. At intermediate or low ratios, the HZ functions as a NO_3^- source, nitrate production efficiency increase with increasing temperature; or the HZ may switch between a N sink during cooler periods and source during warmer periods even with and solely due slight temperature variation that might be observed within diurnal timescales (~5-10 °C variation). Seasonal changes in temperature (> 10 °C) would lead to more pronounced changes in N cycling with increased N removal efficiency during the summer. Further, the thermal patchiness of HZs, particularly in stream reaches that are gaining groundwater with potentially different temperatures, might also translate to N removal efficiency patchiness. Thus, our results imply that field and laboratory studies of biogeochemical reactions in the HZ are further confounded by the stream and hyporheic thermal regimes.

2.5.4 Limitations of this study and future directions

While this study is one of the first to couple and integrate fluid flow and reactive solute transport while relating the biogeochemical reactions to temperature, our analysis did not consider dynamic changes in hyporheic temperature and its potentially complex effect on transient biogeochemical reactions. All the flow models were steady-state, assumed homogeneous sediment, and also assumed thermal homogeneity throughout the domain. We did not consider the effect of ambient groundwater flow and solute inputs, and sediment sorption in this study. Furthermore, stream DO concentration decreases with increasing temperature [*Veraart et al.*, 2011]. We did not consider this thermal effect on stream DO concentration in order to isolate and focus on the temperature effect on N cycling. In general, all stream solute concentrations were kept constant in time, whereas these may vary in certain real field situations. Future studies should focus on simultaneously varying these parameters through space and time. For the reaction scheme, we did not consider ANAMMOX and DNRA, and ignored formation of the intermediate nitrite, which can be far more toxic than nitrate to aquatic life. We also did not consider about the bacteria need time to recover. In addition, this study focused on a single dune geometry. Future studies could focus on realistic, complex bedforms considering the superimposition of smaller bedforms upon larger ones. The above aspects are beyond the scope of this current study which provides the foundation for future investigations.

2.6 SUMMARY AND CONCLUSIONS

Hyporheic zones are hotspots for N transformations and affects the fate of N in

aquatic systems. Biogeochemical reactions in the HZ are naturally complicated by the interaction and competition between the supply rate of reactants, temperature changes, hydraulic properties of the sediment, hydrodynamics of the river, and morphology of the bed. A better understanding of how these factors affect N would be beneficial for predicting the reduction and production of N from the laboratory scale to the field scale, which could potentially be extrapolated to the watershed scale. Due to the complex interactions of the enumerated factors, this study focused on and isolated the effects of temperature. We conducted a series of numerical simulations which considered turbulent open channel flow, pore water flow, and reactive transport models with temperature-dependent reaction constants via the Arrhenius equation. Different homogeneous and steady temperatures were implemented to study the effect of temperature on the hyporheic NO_3^- source/sink function and its associated efficiency. We found that while interfacial fluid flux across the SWI expectedly increased with increasing temperature, the total flux of nitrate from the river into HZ does not always follow the same increasing trend. The relative amount of nitrate and ammonium in the stream, which entered the HZ, also determined whether the HZ functions as a nitrate source or sink, as well as its efficiency in producing or consuming nitrate. Thus, our model results show that water temperature and $[NO_3^-]/[NH_4^+]$ in the stream are both other potentially critical parameters controlling the HZ nitrate removal or production efficiency. There are multiple factors and mutual coupling that result in the complex temperature-dependent of reaction rates. N transformation reaction rates is heavily dependent on temperature but simply using the Arrhenius equation to predict the reaction rate would lead to incomplete

insight by ignoring the changes in interfacial fluid flux and reaction areas. The knowledge gained from this study can guide the prediction and management of stream water quality and ecosystems. Future directions should include extending the models to include couple dynamic temperatures and reactive solute transport in order to further understand the variable stream water temperature effect on the fate of nutrients and hyporheic nitrate source/sink function.

Chapter 3: Diurnal stream temperature effects on nitrogen cycling in hyporheic zones

3.1 ABSTRACT

Stream temperature naturally varies diurnally and seasonally, and these variations in turn propagate into hyporheic zones (HZs), resulting in their dynamic and complex thermal patterns. The resulting thermal regime could determine the presence of biogeochemical hotspots and the occurrence of hot moments. Yet, how diurnal temperature variations affect HZs biogeochemistry remains unknown. We thus conducted a series of multiphysics numerical simulations of non-isothermal fluid flow and multi-component reactive solute transport to investigate this problem. We assumed a sinusoidally varying stream temperature representing diurnal warming and cooling and then studied the effects of different temperature means and amplitudes on HZ nitrate removal efficiency. The results showed that the time-variable nitrification, denitrification and nitrate removal efficiency responded differently to the diurnal stream temperature signal. The temporal variation of spatially-averaged nitrification rate tracks the stream temperature signal, whereas the spatially-averaged denitrification variation pattern has a more complex connection to temperature. We observed a persistent hotspot where significant denitrification rates are present over the 24-hour period. We further evaluated and estimated the bulk removal efficiency calculated by time integration of spatially-averaged reaction rates over a day. The bulk nitrate removal efficiency for cases with

dynamic stream temperature was effectively the same as those with constant and equivalent temperature for denitrification-dominant systems. Therefore, a diurnally dynamic system can be represented by an equivalent steady system with respect to bulk removal efficiency. However, since large instantaneous variations in various rates and metrics were observed, results from randomly timed measurements are unlikely to be representative. This has implications on both past and future synoptic observational studies.

3.2 INTRODUCTION

Stream temperature varies daily and seasonally throughout the year, and this variation generally follows a sinusoidal shape for both diel and annual periods [*Caissie*, 2006; *Webb and Walling*, 1993]. Temperature is an important parameter controlling the health and functioning of fluvial ecosystems [*Hester et al.*, 2009; *Rutherford et al.*, 2004] since most physical processes and biogeochemical reactions occurring throughout the river corridor are sensitive to temperature [*Baer et al.*, 2014; *Dawson and Murphy*, 1972; *Saad and Conrad*, 1993; *Yvon-Durocher et al.*, 2012]. For example, stream temperature influences the metabolism of aquatic organisms; some biologically-mediated reactions double their rate with every 10°C increase in temperature [*Mulholland et al.*, 2006]. Thus, temporal variations in stream temperature should dictate numerous other processes.

Many studies have shown that stream nitrate concentration has a strong negative correlation with stream temperature [*Burns et al.*, 2016; *Heffernan and Cohen*, 2010; *Nimick et al.*, 2003; *Rusjan and Mikoš*, 2010; *Scholefield et al.*, 2005], with warmer temperatures corresponding to lower nitrate concentration. And like stream temperature,

stream nitrate concentration displays diel and annual cycles. For example, streams have maximum nitrate concentrations in the early morning and minimum concentrations in the late afternoon [*Heffernan and Cohen*, 2010; *Rusjan and Mikoš*, 2010; *Scholefield et al*., 2005]. Some studies reported the seasonal variation of nitrate concentration in stream, with highest concentrations observed in colder months and lowest concentrations seen in warmer months [*Christensen et al*.,1990; *Rusjan and Mikos*, 2010; *Halliday et al*., 2013]. In addition, the magnitude of diurnal or seasonal variations in nitrate concentration also showed a close relationship with the range of stream temperature variation. *Rusjan and Mikos* [2010] showed that the diel amplitude of in-stream nitrate concentration changes in different seasons, with the largest daily amplitude in April, the smallest amplitude in July, and intermediate amplitude in November. Correspondingly, stream temperature has the largest daily amplitude in April, smallest amplitude in July due to the shade from the vegetation, and intermediate medium amplitude in November. *Rusjan and Mikos* [2010] pointed out that "81% of the seasonal oscillation in stream nitrate concentration can be explained by the diel stream water amplitudes". *Mulholland et al*. [2006] also demonstrated that the diurnal variation in stream temperature can account for more than 54% of the increases in nitrate uptake rate. Yet, the details of the mechanisms underpinning the temperature effect on in-stream nitrate concentration remains elusive.

Streams are not pipes. Streams and their underlying aquifers are connected through hyporheic zones (HZs). Stream water infiltrates into and flows through the subsurface sediment and returns back to the stream after relatively short flow paths [*Harvey and Bencala*, 1993; *Tonina and Buffington*, 2009; Cardenas and *Wilson*, 2004].

Hyporheic flow is typically driven by variations in the pressure gradient along the sediment-water interface [*Thibodeaux and Boyle*, 1987] induced by small-scale streambed roughness elements (ripples, dunes, obstacles) [*Cardenas et al.*, 2008; *Cardenas and Wilson*, 2007b; *Hester et al.*, 2014; *Sawyer et al.*, 2011], or large-scale hydrological and morphological factors (riffles and pools, river curvature, steps, rapids) [*Boano et al.*, 2006; *Endreny et al.*, 2011; *Fabian et al.*, 2011; *Kasahara and Wondzell*, 2003; *Tonina and Buffington*, 2007]. Stream water carries heat and solutes flowing through the sediments by advection, diffusion, and mechanical dispersion processes. Thus, hyporheic exchange plays an important role in the thermal pattern of the HZs [*Norman and Cardenas*, 2014], and the distribution and transformation of nutrients [*Zarnetske et al.*, 2011; *Zarnetske et al.*, 2012]. A number of prior studies have demonstrated that HZs are important sites for biogeochemical reactions [*Bardini et al.*, 2012; *Hill et al.*, 1998; *Kessler et al.*, 2015; *Wondzell and Swanson*, 1996; *Zarnetske et al.*, 2011; *Zarnetske et al.*, 2012], regulating downstream nitrogen export in aquatic environments [*Alexander et al.*, 2000; *Alexander et al.*, 2009; *Gomez-Velez et al.*, 2015; *Kiel and Cardenas*, 2014; *Peterson et al.*, 2001].

Our recent study showed the effect of temperature on nitrate removal efficiency in the HZs [*Zheng et al.*, 2016]. The result indicated that the relative abundance of ammonium and nitrate in stream and temperature were two important factors influencing nitrate removal efficiency of the HZs. But this study assumed that temperature across the HZs was uniform and constant. However, hyporheic temperature is not uniform but varying in space and time in natural environments. The distribution and dynamics of

temperature in streambed sediments are associated with large in-stream structures [*Gerecht et al.*, 2011; *Hester et al.*, 2009], small bedforms such as ripples and dunes [*Norman and Cardenas*, 2014], riffles [*Swanson and Cardenas*, 2010], small obstacles such as logs [*Menichino and Hester, 2014; Lautz et al., 2010*], over-all gaining or losing stream conditions [*Cardenas and Wilson*, 2007c], and the stream temperature regime [*Cardenas and Wilson*, 2007b]. Thermal heterogeneity of the HZs will cause the temperature-dependent reactions (e.g., denitrification) occurring within the HZs to have different responses to the diurnal or seasonally varying stream temperatures. The complications due to the dynamic and non-uniform hyporheic temperature pattern would create potential hot spots and hot moments for the effective denitrification zone, and this in turn has important implications for stream ecosystems and water resources management [*Briggs et al.*, 2014; *Lautz and Fanelli*, 2008; *McClain et al.*, 2003]. Assessing the daily, monthly or yearly overall trend of nitrogen cycling in streams, obtained through a single sampling, may not be able to capture the spatial and temporal variations of water quality [*Mulholland et al.*, 2006]. Thus, the effect of natural temporal and spatial changes of temperature on N transformation in the HZs are still poorly understood. To this end, we used a fully coupled fluid flow, heat transport, and reactive solute transport model to examine the effect of stream diurnal temperature variations on nitrogen dynamics in HZs.

3.3 METHODOLOGY

The modeling scheme and governing equations in this study follow those by *Cardenas and Wilson* [2007a; b], *Bardini et al.* [2012] and most closely that in *Zheng et al.*

[2016]. The key difference between *Zheng et al.* [2016] and this study is that transient conditions are considered here. The modeling scheme is illustrated in Figure 3.1. Briefly, (1) steady-state two-dimensional turbulent water flow over a dune was modeled; (2) the pressure along the *SWI* from the turbulent flow model was used as a boundary condition for a groundwater flow model of hyporheic flow in the sediment; (3) transient hyporheic flow and heat transport was linked with fluid flow using the advection-conduction-dispersion equation; and finally (4) the time-varying groundwater flow field was used as input to a transient reactive transport model where the reaction kinetics were temperature-dependent. Each component of the multiphysics model is described in full details in the supporting information. The models represent a two-dimensional longitudinal-vertical section of a channel-sediment domain with a representative unit dune.

For the heat transport model, we assumed a diel stream temperature cycle following the sinusoidal function (Figure 3.2a):

$$T(t) = T_{ave} + T_{amp}\left[\sin\left(2\pi t/\tau\right)\right] \tag{3.1}$$

where T_{ave} is the average about which temperature fluctuates, T_{amp} is the amplitude of the fluctuations, and τ is the period of the fluctuations (24 hours). For the first 12-hour period, temperature varies from the T_{ave} to its maximum temperature (T_{ave}+T_{amp}) and then drops to the T_{ave}; we considered this half period as the warm phase (warmer than T_{ave}) for the following 12-hour period, temperature varies from T_{ave} to its minimum temperature (T_{ave}-T_{amp}) and then goes back to T_{ave}; we considered this half period as the cool phase (cooler than T_{ave}). The sinusoidal function was imposed as a time-varying Dirichlet boundary condition at the top boundary of the heat transport model.

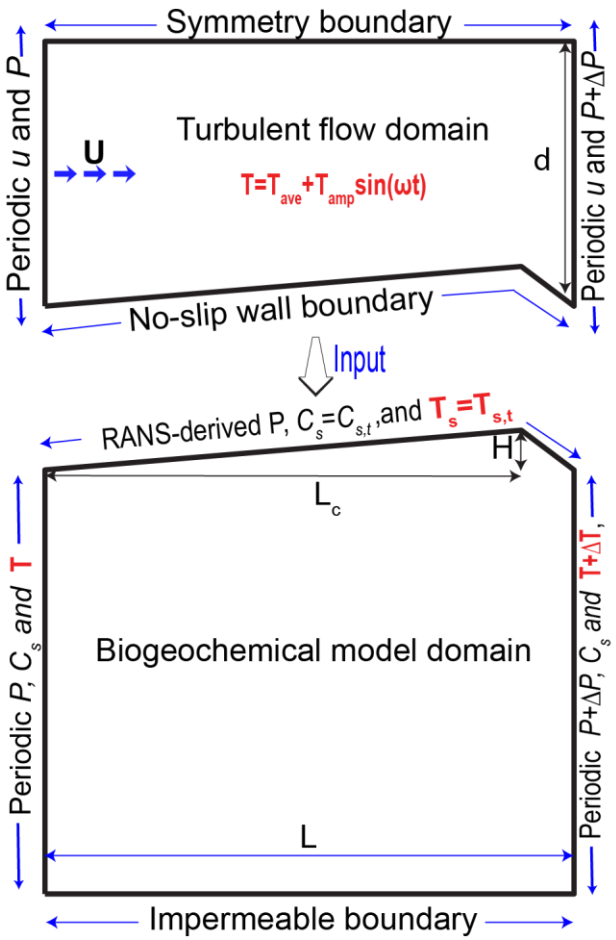

Figure 3.1: Schematic representation of numerical modeling approach for the physical and biogeochemical processes occuring in a representative bedform-induced HZ. The streambed length L=1 m, height H=0.075 m, with the crest at 0.9 L (L_c =0.9 m), and the sediment depth is 0.8 m. The upper figure represents the stream flow (water depth d=0.5 m), while the lower figure represents the permeable sediment. T is temperature, P is pressure, C is solute concentration, and U is stream velocity. (Modified from Zheng et al., 2016)

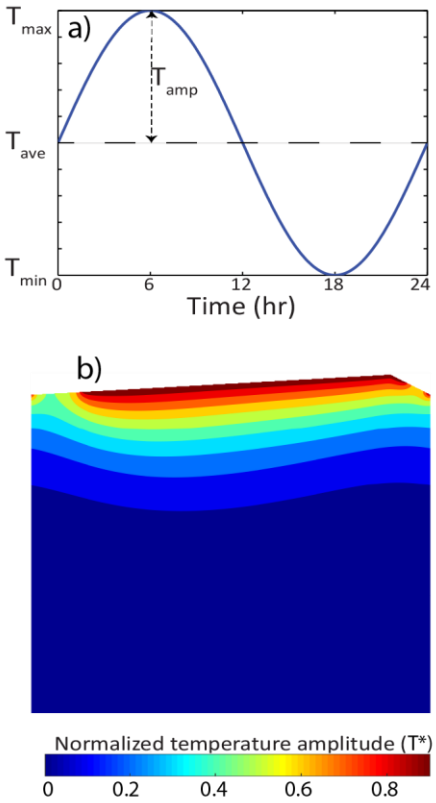

Figure 3.2: (a) Diel cycle of stream temperature as described by equation (3.1) which is used as a Dirichlet top boundary for the heat transport model of the sediment domain. The time period is 24 hours for all the simulations. T_{ave} is the average about which the temperature fluctuates and T_{amp} is the amplitude of the fluctuations. T_{ave} and T_{amp} vary for different simulations. (b) The normalized temperature amplitude T* described by equation (3.2) for each simulation. T*=1 means that the entire temperature range of the diel forcing can be observed at that given point, while T*=0 means that point is insensitive to the stream temperature signal.

Five average temperatures from 10°C to 30°C in increments of 5°C and three temperature amplitudes, 3°C, 4°C, and 5°C were considered. Thus, there were 15 simulations in total for each stream case: polluted or pristine. To clearly show the spatial distribution of daily temperature variations considering a broad range of mean temperature and amplitude, we normalized the streambed temperature pattern (Figure 3.2b) for our simulation cases through [*Cardenas and Wilson*, 2007b]:

$$T^*(\mathrm{x},\mathrm{y}) = \frac{T_{max} - T_{min}}{2T_{amp}} \tag{3.2}$$

where T_{max} and T_{min} are the maximum and minimum of streambed temperature, respectively, observed at a specific location (x, y) over a 24-hour period.

A key feature of the groundwater flow model is that the flow field was dynamic even though the flow boundary condition (the pressure distribution along the sediment-water interface) was steady. The dynamical nature of flow field can be attributed to the effect of temperature on hydraulic conductivity via temperature-dependence of water viscosity.

The reaction set for the transport model includes aerobic respiration, denitrification, and nitrification (Table 2.1). The stream concentration for the pristine and polluted cases were prescribed as a steady boundary condition at the top of the model domain where hyporheic flow paths originate from (Table 3.1). The reactions were assumed to have first-order kinetics following the parameters in Table 3.2, with the rate constant depending on temperature via the Arrhenius equation. All species were assumed to be absent in the HZ at the start of the simulation. The complete set of relevant transport

Table 3.1: In-stream and hyporheic inflow boundary concentration of solutes

Case	[DOC] (mg/L)	[O_2] (mg/L)	[NO_3^-] (mg/L)	[NH_4^+] (mg/L)
Polluted Stream	150	10	8	1
Pristine Stream	50	10	1	0.05

Table 3.2: Summary of input parameters for the reactive transport models

Symbol	Unit	Value	Description
D_m	[m^2/s]	1×10^{-10}	Molecular diffusion coefficient
θ	[-]	0.4	Porosity
τ	[-]	$\theta^{1/3}$	Tortuosity
$\beta 1$	[-]	1	Ratio of transferred electrons for O_2
$\beta 2$	[-]	0.8	Ratio of transferred electrons for NO_3^-
$[O_2]_{lim}$	mg/L	1	Oxygen limiting concentration
$[NO_3^-]_{lim}$	mg/L	0.5	Nitrate limiting concentration
k_{NH4+}	L/(mg·s)	5×10^{-6}	Second-order nitrification molar rate coefficient at temperature 20°C
k_{DOC}	1/s	5×10^{-6}	DOC decay constant at temperature 20°C
R	J/(K·mol)	8.31	Gas constant
$E1$	kJ/mol	60	Activation energy for aerobic respiration
$E2$	kJ/mol	162	Activation energy for nitrification
ρc	J/(m^3·K)	1.72×10^6	Bulk specific heat
$\rho_w c_w$	J/(m^3·K)	4.19×10^6	Water specific heat
K_T	W/(m·K)	1.72	Bulk thermal conductivity

parameters were listed in Table 3.2. The flow and reactive transport models were run for several days until a quasi-steady-state was reached, after which the results from the last 24 hours were analyzed.

To investigate the spatial variation of denitrification rates, we normalized the denitrification rates in the HZ through:

$$r_{DN}^{*}(\mathrm{x},\mathrm{y}) = \frac{r_{DN_{max}} - r_{DN_{min}}}{max\left(r_{DN_{max}} - r_{DN_{min}}\right)} \tag{3.3}$$

where $r_{DN_{max}}$ and $r_{DN_{min}}$ are the maximum and minimum instantaneous denitrification rate, respectively, observed at specific location (x,y) at streambed over a 24-hour period. The denominator in equation (3.3), $max\left(r_{DN_{max}} - r_{DN_{min}}\right)$, was used to calculate the maximum variation range across entire HZs over a day. Thus, a point with $r_{DN}^{*} = 1$ means that the maximum variation range can be observed at that given point, while $r_{DN}^{*} = 0$ means that there were no variations or that no denitrification occurred.

The spatially averaged reaction rates were calculated by integrating the distributed reaction rates over the whole sediment domain and then dividing by the area (A) of the HZ [*Bardini et al.*, 2012]:

$$\overline{r_{NI}} = \frac{1}{A}\int \theta \cdot \mathrm{r}_{\mathrm{NH}_4^+} \cdot \mathrm{dA} \tag{3.4a}$$

$$\overline{r_{DN}} = \frac{1}{A}\int \theta \cdot r_{red,2} \cdot \mathrm{dA} \tag{3.4b}$$

$$\overline{r_{netDN}} = \frac{1}{A}\int \theta \cdot R_{\mathrm{NO}_3^-} \cdot \mathrm{dA} \tag{3.4c}$$

Negative net denitrification values ($\overline{r_{netDN}}$) indicate that the amount of nitrate

consumption through denitrification is greater than the amount of nitrate production from nitrification, and vice versa.

Moreover, the reaction rates were expected to vary over the course of 24h as temperature varied. In order to study the dynamic temperature effect on reaction rates over a day, the reaction variations were compared with a steady-state temperature case using:

$$\Delta\overline{r(t)}\% = 100\frac{\overline{r(t)} - \overline{r_{T_{ave}}}}{\overline{r_{T_{ave}}}} \tag{3.5}$$

where $\overline{r(t)}$ is the spatially averaged reaction rate at time t, $\overline{r_{T_{ave}}}$ is the spatially averaged reaction rate from the steady-state temperature case (the case with the identical T_{ave}) taken from our previous study [*Zheng et al.*, 2016].

We employed NO_3^- removal efficiency (N_{RE}) as a metric to evaluate the HZ functionality and its associated efficiency. N_{RE} is a dimensionless number that expresses the relative rates of reaction and substrate supply as:

$$N_{RE} = \frac{\int_0^t \iint_A r_{netDN \cdot dA \cdot dt}}{\int_0^t [NO_3^-]_{in} \cdot dt} \tag{3.6}$$

where r_{netDN} is the net denitrification rate of the HZ, and $[NO_3^-]_{in}$ is the total influx of NO_3^- into the HZ. The range of N_{RE} is between 0 and 1 as the HZ is a nitrate sink in both stream cases (N_{RE} <0 when the HZ is a nitrate source). A larger value for N_{RE} indicates higher NO_3^- removal efficiency.

3.4 RESULTS

3.4.1 Diurnal stream temperature effects on hyporheic zone temperature and nutrient distribution

As stream temperature sinusoidally varied over a day (Figure 3.2), the temperature signal propagated into the streambed sediment and resulted in a complex temperature pattern. This was exemplified by both polluted and pristine stream case with T_{ave}=20℃ and T_{amp}=5℃ (Figure 3.3). That is, when the stream temperature reached its maximum when time t=6 hr, the streambed also had a relatively higher temperature. Moreover and as expected, when stream temperature reached the minimum when t=18 hr, the streambed temperature was also relatively lower. Larger temperature variations were observed closer to the *SWI*, and the streambed temperature variation expectedly weakened with penetration depth (Figure 3.2).

The hyporheic flow fields were nearly the same over a course of a day (Figures 3.3), which implied that temperature variation hardly affected the flow kinematics. For both stream concentration cases, the concentration fields of the four species all decreased with depth due to their consumption (Figures 3.3). Moreover, solute concentrations all had a similar parabolic or semi-circular shape that varied in size; this was directly dependent on the feature of the hyporheic flow field which constituted two semi-circular flow cells (or quasi-parallel collection of flow paths).

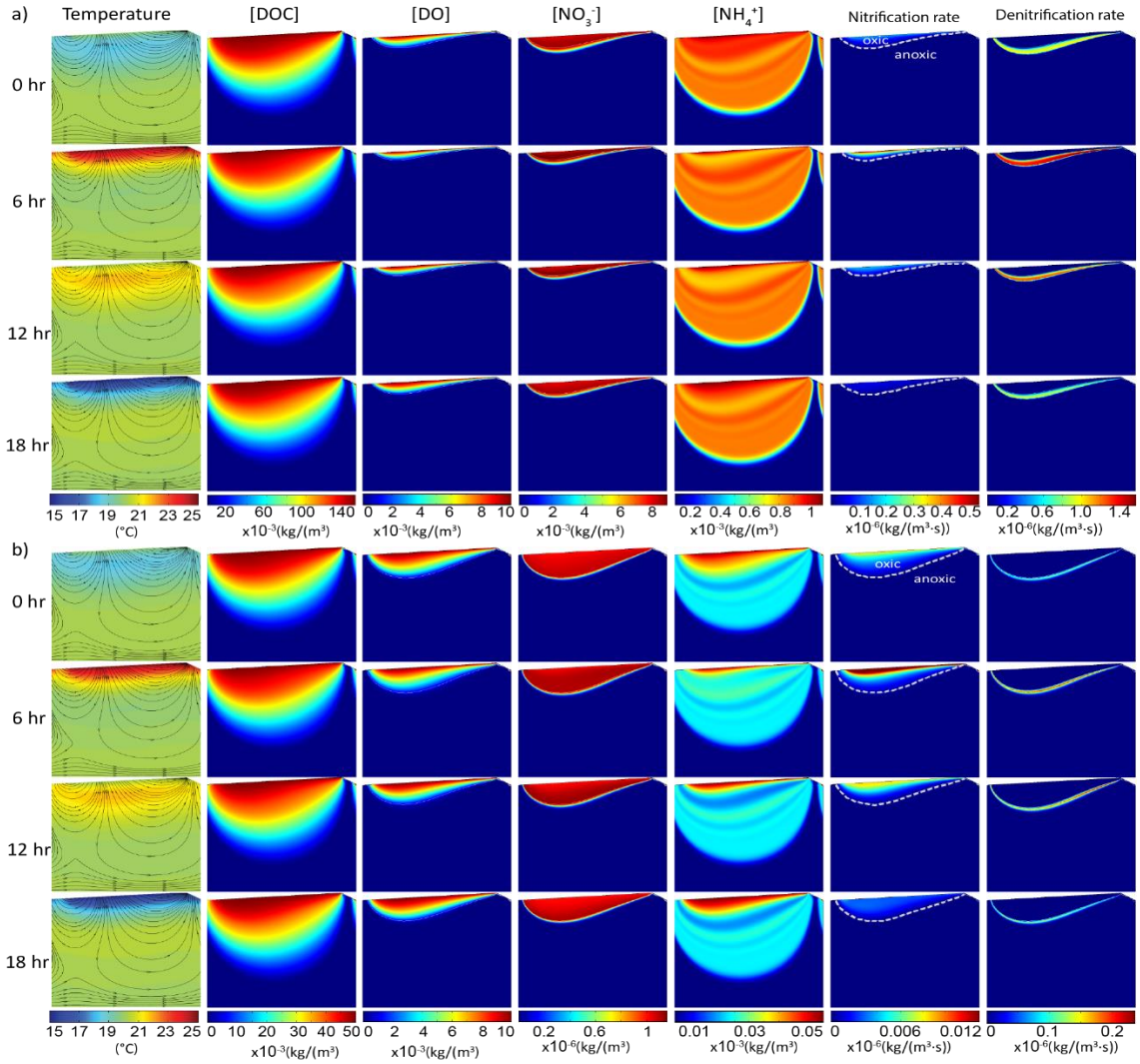

Figure 3.3: Snapshots of temperature, solute and reaction rate fields for the (a) polluted and (b) pristine stream cases, both with T_{ave} =20℃, T_{amp} =5℃ . Channel flow is from left to right. The domain is 1 m wide.

The penetration depth of solutes decreased with increasing temperature. This was illustrated from the shallowest penetration depth at t= 6 hr (maximum stream temperature), especially for DO and nitrate (Figure 3.3). While at time t=18 hr, when stream temperature was at its minimum, the penetration of solutes deepened to their maximum. The penetration depth of DOC was deeper than that of DO and NO_3^- for any given time due to the relatively high supply of DOC. Ammonium that was not nitrified in the oxic zone was simply transported further along the hyporheic flow path and spread over the HZs due to dispersion. The oxic-anoxic boundary became shallower from time t=0 hr to t=6 hr when stream temperature was increasing, and it deepened from t=6 hr to t=18 hr as temperature dropped (Figure 3.3). This was because nitrification and aerobic respiration reaction rates occurring in the shallower zone increased as temperature went up, resulting in faster oxygen depletion.

3.4.2 Temperature effect on the variations of denitrification rate during a day

Denitrification occurred below the oxic-anoxic boundary in a very narrow zone or envelope. Increasing temperature promoted oxygen depletion and resulted in an upward movement of the anoxic-oxic boundary. Consequently, the denitrification zone (i.e., the hotspot for denitrification) moved upwards and downwards as average temperature increased or decreased, respectively (Figure 3.3). In order to detect consistent hotspots of denitrification (Figure 3.3), I investigated the spatial variation of denitrification rates in the HZ over a 24-hour period to get the normalized denitrification rates. The entire range of denitrification rates variations ($r_{DN_{max}}$and $r_{DN_{min}}$) observed at a given point due to temperature variations were divided by the maximum variation range accorss the entire

HZ over a 24-hour period (Equation 3.3). Unlike the normalized temperature pattern (Figure 3.2), the spatial distribution of normalized denitrification rate variations showed a non-monotonic trend with depth for both stream cases (Figure 3.3).

The dynamics of the envelope defined by normalized denitrification rates (Equation 3.3) represents the potential effective denitrification zone's response to temperature variation. Since the daily temperature signal followed a sinusoidal function, the upwards and downwards movement of the effective denitrification zone created an overlapping area where significant denitrification rates were present all the time. The variations of denitrification rates within the overlapped area were relatively smaller than those at the envelope's edge (Figure 3.4). At the edge of the envelope, effective denitrification only occurred when temperature was high during the day. At other times, denitrification was negligible in this edge area. Consequently, the variations of denitrification in the edge area can be much larger, while in the overlapped area, effective denitrification persisted, which led to relatively smaller temporal variations. This was especially true for the polluted stream case regardless of temperature variation scenario.

In the pristine stream, the relatively high normalized denitrification values within the envelope were located in its central part (Figure 3.5) and the envelope was generally deeper. This is because the effective denitrification zone was much narrower than that of the polluted stream case (Figure 3.3). This consequently resulted in a narrow overlapping area of high denitrification. However, this narrow area (several *cm* to dozens of *cm* in thickness, with the bedform wavelength) was a persistent hotspot.

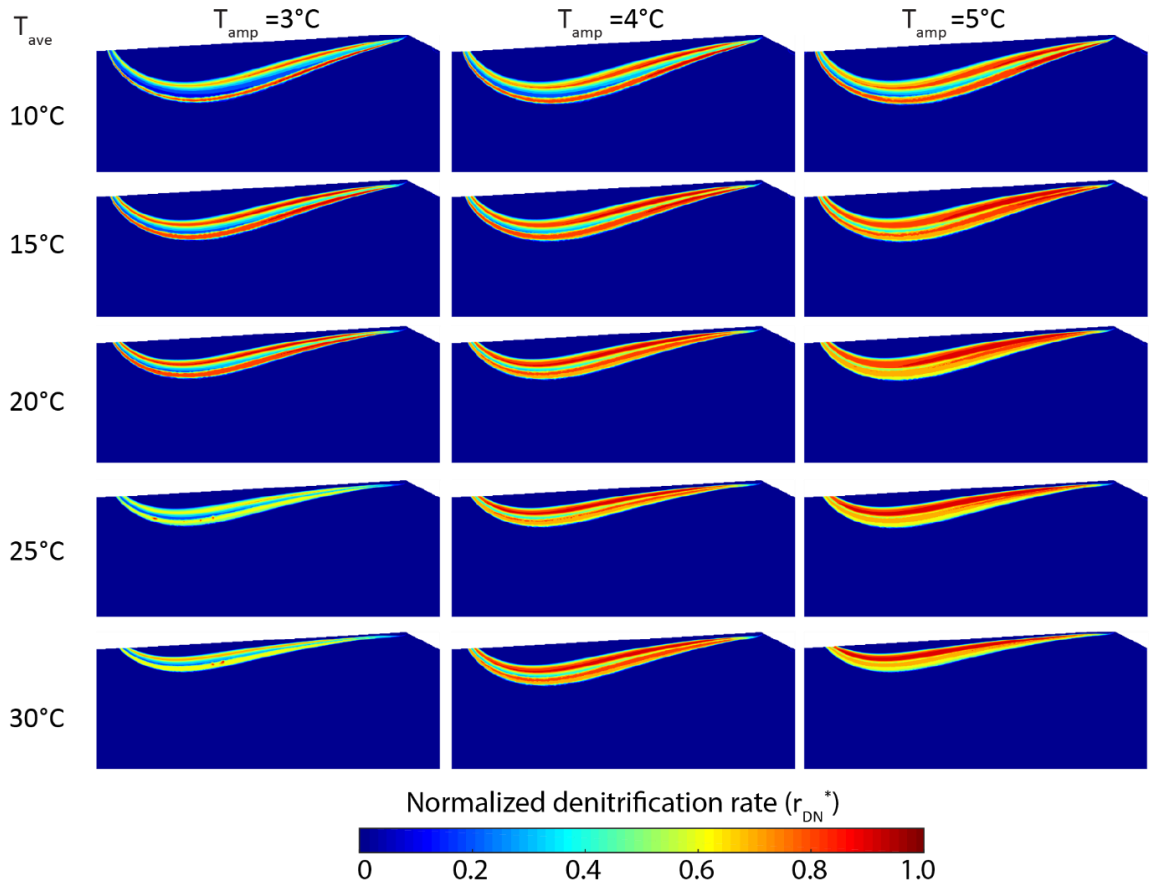

Figure 3.4: Snapshots of the normalized denitrification rate field for the polluted stream case. The normalized denitrification rates r_{DN}* is defined by equation (3.3). A point with r_{DN}*=1 means that the maximum variation range can be observed at that given point for that scenario, while r_{DN}*=0 means no variations or no denitrification occurs. The domain is 1 m wide, the depth is 0.5m.

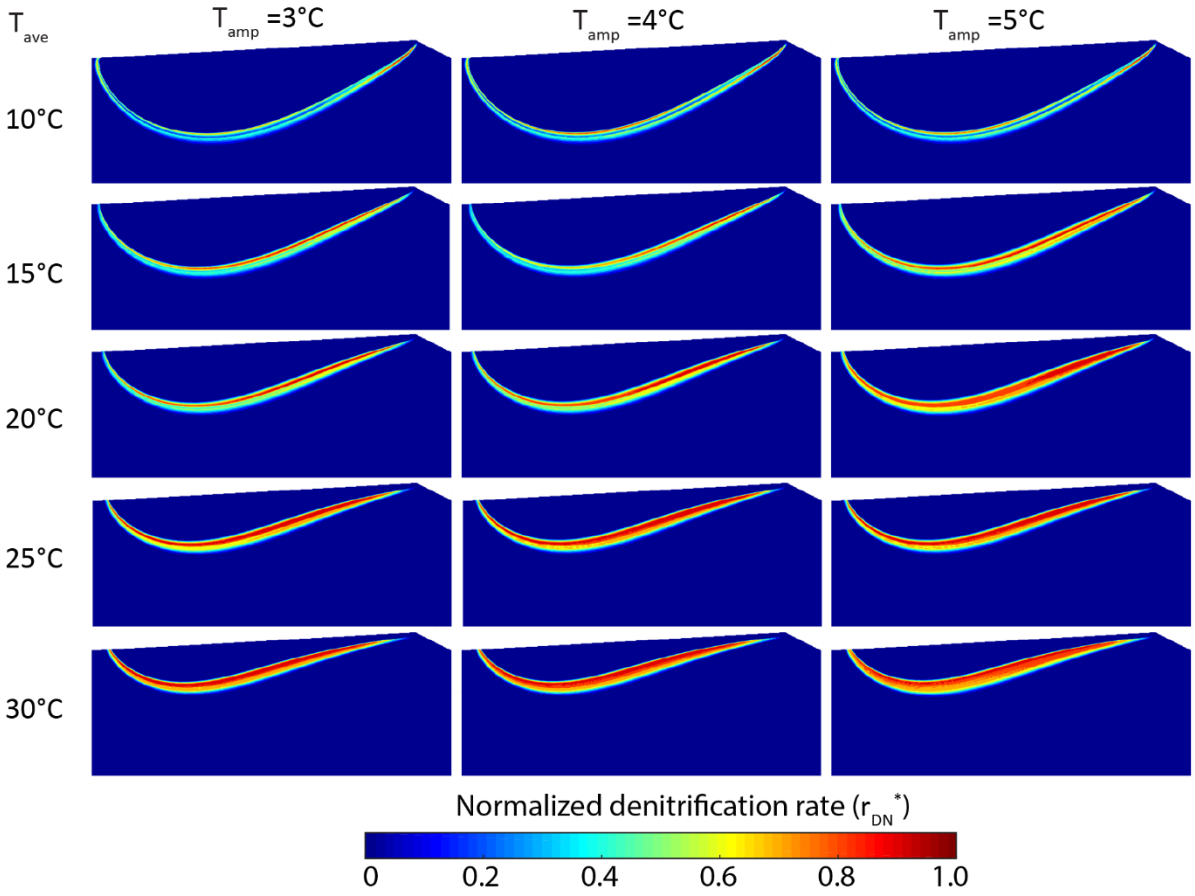

Figure 3.5: Snapshots of the normalized denitrification rate field for the pristine stream case. The normalized denitrification rates r_{DN}* is defined by equation (3.3). A point with r_{DN}*=1 means that the maximum variation range can be observed at that given point for that scenario, while r_{DN}*=0 means no variations or no denitrification occurs. The domain is 1 m wide, the depth is 0.5m.

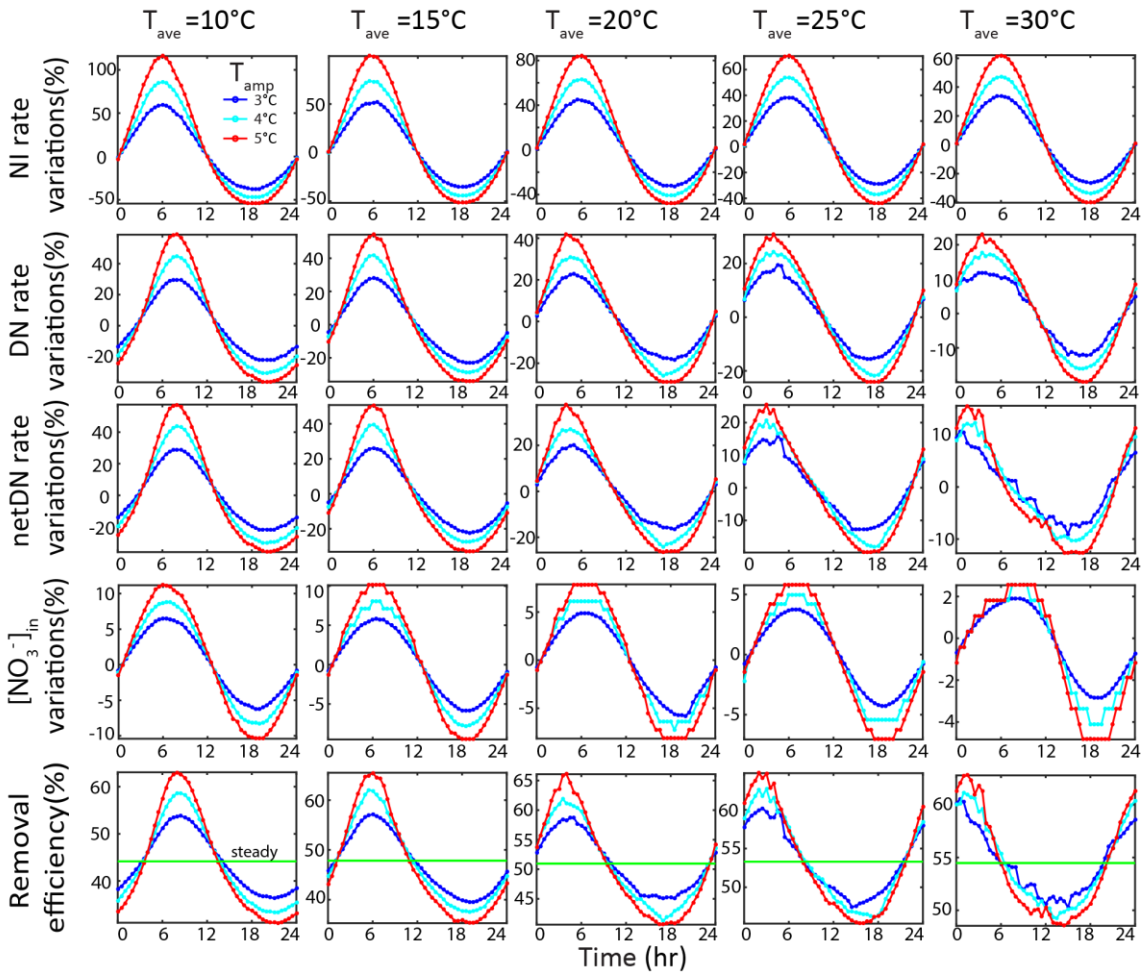

Figure 3.6: Temporal variations of various reaction metrics (areally-integrated or averaged) for the polluted stream case.

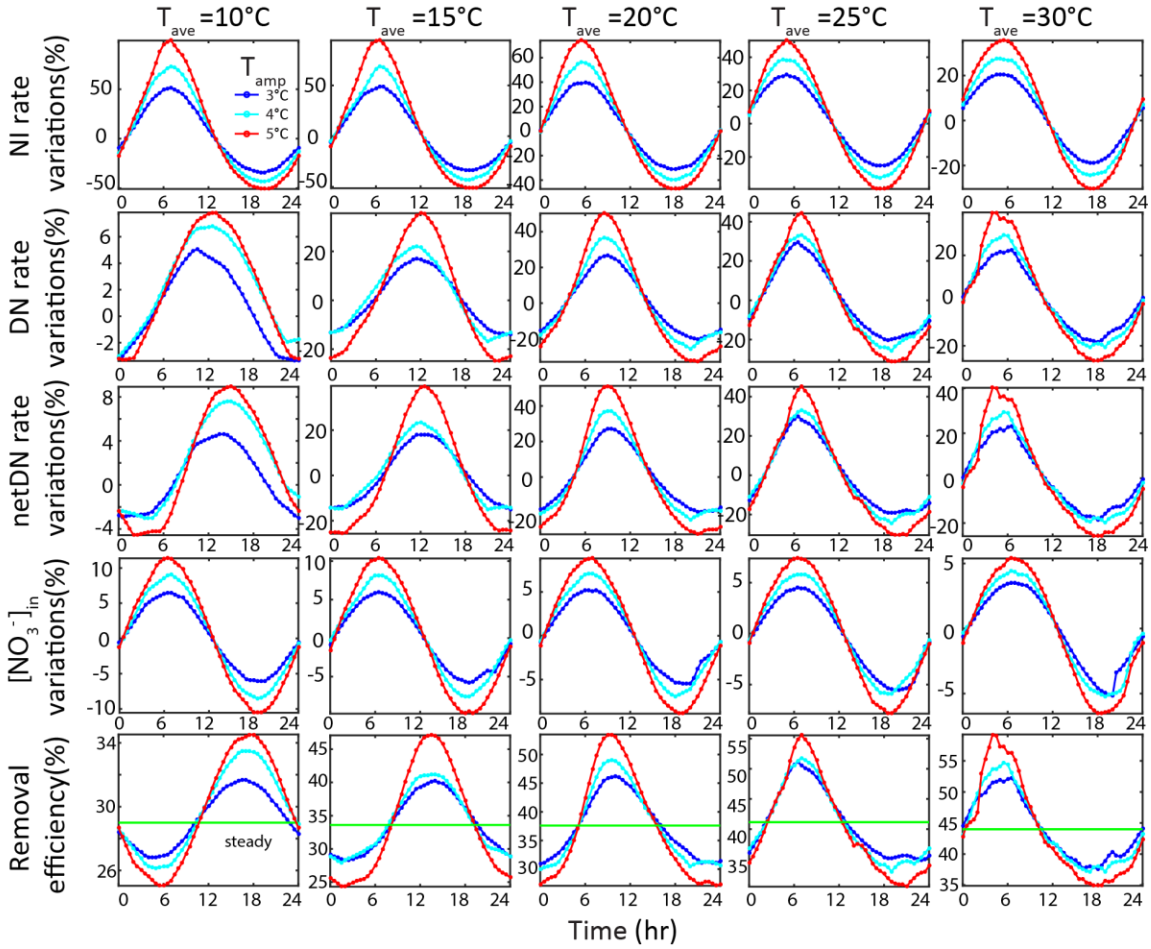

Figure 3.7: Temporal variations of various reaction metrics (areally-integrated or averaged) for the pristine stream case.

3.4.3 Diurnal temperature effect on nitrate influx into the hyporheic zone

$[NO_3^-]_{in}$ varied following the stream temperature pattern which was symmetric about 0% for both stream concentration cases (Figures 3.6-3.7). It had two notable features: (1) the maximum variation decreased with increasing T_{ave}, and (2) larger amplitudes expectedly led to a broader range of variations, i.e., the variation range for the higher amplitude (T_{amp}=5°C) was nearly two times of the variation range for the lower amplitude (T_{amp}=3°C). Note that the simulations had convergence issues with increasing T_{ave}, but overall the computational results were reasonable with only slight numerical errors. These slight errors were apparent even after extensive fine-tuning of some of the higher T_{ave} models.

3.4.4 Diurnal temperature effects on the variations of the spatially-averaged N reaction rates

Temperature can have a measurable effect on the interfacial fluid flux due to its effect on hydraulic conductivity which is affected by viscosity; but, it expectedly only affects the velocity magnitude, and does not alter the general flow pattern as shown in Figure 3.3. Temperature would however affect the nutrient cycling in HZs through the supply rate of solutes, i.e., it affects the reaction rates due to more availability of reactants advected into the hyporheic zone at higher temperature. The temperature effect on both spatially-distributed and instantaneous but spatially-integrated reaction rates were therefore analyzed in more detail below.

3.4.4.1 Nitrification rate

The concentrations of NH_4^+ and DO decreased with depth in the HZ (Figure 3.3) due to nitrification and respiration, respectively. Additionally, nitrification rate should increase with increasing temperature according to the Arrhenius equation. Since as mentioned above that the temperature signal dampened with increasing depths (Figure 3.2), we expectedly observed that nitrification rate decreased with depth (Figure 3.3). The penetrating heat is one cause for this, and the other factor is the solute supply rate as alluded to above. Since the daily stream temperature varied sinusoidally, so did the nitrification rate in the HZ (Figure 3.3). Nitrification rate was clearly larger at t= 6 hr when the shallow HZ was warmest than that at t=18 hr when it was coldest.

We integrated the nitrification rate over the HZ to get the spatially-averaged nitrification rate and identify the temperature effect on total nitrate removal efficiency by the unit bedform. In addition, instantaneous reaction rates were compared with those of the steady temperature case [*Zheng et al.*, 2016] following equation (3.5). The temporal variation in the spatially-averaged nitrification rate followed the diurnal stream temperature signal for both pristine and polluted cases, regardless of substrate concentration (Figures 3.6-3.7). This is because nitrification occurs at shallower depths where there is DO from the stream and where the stream's temperature signal is strongest (Figure 3.2).

The nitrification variation pattern over a day had two notable characteristics. First, the variations were asymmetric about 0% for all cases. That is, the variations in the first 12 hours (warm phase) were relatively larger than that of the following 12 hours (cool

phase). For example, for the polluted stream case with T_{amp}=5°C, the maximum of the nitrification rate variation over the domain during the warm phase was 102%, while it was -50% over the cool phase. This can be explained by the exponential dependence of the rate constant on temperature following the Arrhenius equation; this exponential form becomes particularly important when there is a relatively high supply of reactants. That is, the incremental change in reaction rate with a given temperature perturbation at lower temperature is smaller than at relatively higher temperature. Second, larger amplitudes led to higher nitrification rate variation. For both stream cases, nitrification variations with T_{amp}=5°C was nearly twice as large as that with T_{amp}=3°C at the same T_{ave}.

3.4.4.2 Denitrification rate and net denitrification rate

We also analyzed the denitrification variations in comparison to the steady temperature case, following equation (3.5). The denitrification rate variations over the 24-hour period were not fully synchronized with the stream temperature signal, unlike nitrification rate variations. The variation pattern was lagged with the stream temperature signal at low T_{ave}. However, the patterns were more synchronized with the stream temperature signal with increasing T_{ave} (Figures 3.6-3.7). The patterns fairly followed the temperature variation at T_{ave} =20°C and 30°*C* for the polluted and pristine stream cases, respectively. Note that the denitrification rate reached its maximum earlier with increasing T_{ave}. For the polluted stream case, the maximum denitrification occurred around t=8 hr for T_{ave} =10°C, followed by t=6 hr for T_{ave}=15°C, at t=5 hr for T_{ave} =20°C, about t=4 hr for T_{ave}=25°C, and at t=3 hr for T_{ave}=30°C (Figure 3.6). Moreover, for the pristine stream case, the maximum denitrification occurred at around t=14 hr, t=12 hr,

t=8 hr, t=7 hr, and about t=4 hr when T_{ave}=10°C, 15°C, 20°C, 25°C, and 30°C, respectively (Figure 3.7). This was because the effective denitrification reaction zone moved up to a shallower area (Figure 3.3) where there was stronger temperature signal penetration with increasing T_{ave}. That is, temperature changes were experienced sooner by the denitrification zone with higher T_{ave}. This result was not only due to the large temperature variations, but was also due to increased nitrification that supplied additional NO_3^- to the denitrification zone. Note that the upwards movement of the denitrification zone made the denitrification variations gradually more in synchrony with the stream temperature signal with increasing T_{ave}.

The denitrification variation was asymmetric about 0%, where the range in the warm phase was 1~2 times larger than that in the cool phase for both stream cases. Similar to nitrification variation, this could also be explained by the Arrhenius equation. With a given mean temperature (T_{ave}) and temperature perturbation (T_{amp}) the variations in nitrification rate in the cooling phase was smaller than the variations in the warm phase. This implies less nitrate supply variations due to nitrification variations in the cooling phase compared with warm phase.

The denitrification rate variation also depended on the temperature amplitude. Expectedly and according to the Arrhenius equation, larger amplitudes resulted in broader ranges of reaction rates compared to that of lower amplitude cases. For example, with the same T_{ave}, denitrification variations with T_{amp}=5°C was nearly twice as large as that with T_{amp}=3°C for both stream cases. The nitrate supply and reaction temperature dependence together produced the denitrification temperature dependence.

The spatially-averaged net denitrification rate was calculated following equation (3.4c). Additionally, we analyzed the relative variation pattern by comparing with the steady temperature case, calculated by equation (3.5). The instantaneous spatially-averaged net denitrification followed the denitrification variation pattern for both stream cases as denitrification dominates over nitrification in both.

3.4.5 Diurnal temperature effect on the daily N removal efficiency (N_{RE})

The prior knowledge of net denitrification in the HZ and $[NO_3^-]_{in}$ were used to estimate N_{RE}, calculated following equation (3.6). N_{RE} variation during a day followed the net denitrification variation pattern. Similar to the net denitrification variation pattern, the temporal pattern of N_{RE} was different for both polluted and pristine stream cases due to the above-mentioned dependence of denitrification rate on temperature and substrate concentration.

For the polluted stream case, N_{RE} was higher in the warm phase than in the cool phase, although with some phase shift. The maximum N_{RE} occurred earlier with increasing T_{ave} (Figure 3.6). Specifically, the maximum N_{RE} occurred around t=8 hr for T_{ave}=10℃, followed by t=6 hr for T_{ave}=15℃, about t=4 hr for T_{ave}=20℃, around t=3 hr for T_{ave}=25℃, and about t=2 hr for T_{ave}=30℃. Additionally, the variation range became smaller with increasing T_{ave} with any given T_{amp} (Figure 3.6). Take T_{amp}=5℃ as an example, N_{RE} variation range decreased from 30% for T_{ave}=10℃ to around 12% for T_{ave}=30℃. The T_{amp} also affects N_{RE}. The larger amplitude case (e.g., T_{amp}=5℃) showed a broader removal efficiency variation range than that of the relatively lower amplitude case (T_{amp}=3℃) (Figure 3.6). For example, for T_{ave}=10℃, N_{RE} changed from 32% to

62% during a day for the T_{amp}=5℃ scenario; the N_{RE} changed from 38% to 53% during a day for the T_{amp}=3℃ scenario. The N_{RE} variation range (30%) for T_{amp}=5℃ was nearly twice of that (15%) for T_{amp}=3℃ at T_{ave}=10℃.

For the pristine stream case, the dynamics of N_{RE} variation pattern was almost opposite to the temperature variation pattern at low T_{ave} regime (Figures 3.7). Unlike the polluted stream case, N_{RE} was lower in the warm phase compared to N_{RE} in the cold phase. For T_{ave}=10°C case, minimum N_{RE} occurred at t=6 hr when stream temperature reached its daily maximum; while maximum N_{RE} occurred at t=18 hr when stream temperature reached its minimum. But with increasing T_{ave}, the N_{RE} variation pattern gradually followed the temperature variation pattern. In addition, the time of the maximum N_{RE} arrived earlier with increasing T_{ave}. That is, the maximum N_{RE} advanced from around t=18 hr for T_{ave}=10°C to about t=5 hr for T_{ave}=30°C. Similarly, with given T_{ave}, N_{RE} variation range for larger amplitude T_{amp}=5℃ was nearly twice of that for lower amplitude T_{amp}=3℃.

3.5 DISCUSSION

3.5.1 Can steady hyporheic temperature conditions be assumed when considering hyporheic biogeochemical processes? Do the diurnal fluctuations matter?

The temperature pattern in the HZs is spatially complex and dynamic due to the daily and seasonally varying stream temperature, and potentially varying stream and streambed conditions (Norman and Cardenas, 2014; Marzadri et al., 2013). Bacterially-mediated N transformation reactions are also strongly temperature dependent (Veraart et al., 2011; Kirschbaurm et al.,1995). Thus, it is not surprising that temperature plays a

critical role in N transport and removal in the HZ. Our results showed that nitrification, denitrification, net denitrification and nitrate removal efficiency varied significantly over a day due to the daily temperature fluctuations for both polluted (high N) and pristine (low N) stream cases (Figures 3.6 and 3.7). The temporal variability of N removal efficiency driven by the temperature variation cannot be captured by an instantaneous measurement. Reaction rates (or substrate concentrations) measured at a specific time in the field during a day may not be representative of the daily-averaged reaction rates (or concentration), unless it so happened that the measurement occurred at a moment and location that coincides with a representative spatial-temporal average. Given variability in lags of the different reactions (e.g., nitrification vs. denitrification), it is difficult to pick a specific time or location that is representative. Our results showed that the potential effective denitrification zone moved up and down as a result of the daily fluctuations of stream temperature. However, there were overlapping areas with relatively smaller variations of denitrification during a day. This area can be considered as a persistent spot which captures the relatively steady effective denitrification rate during a day. Our findings suggest that apparent errors are inherent in instantaneous measurements since it is unclear what they represent in terms of temporal or even spatial averages.

Our results showed that the dynamics of nitrification and total nitrate influx strongly followed the diurnal stream temperature signal but with asymmetric variations. Furthermore, denitrification was not fully synchronized with the stream temperature signal (Figures 3.6-3.7). When the goal is to determine the daily nitrate removal efficiency, can steady hyporheic temperature conditions be assumed? To answer this

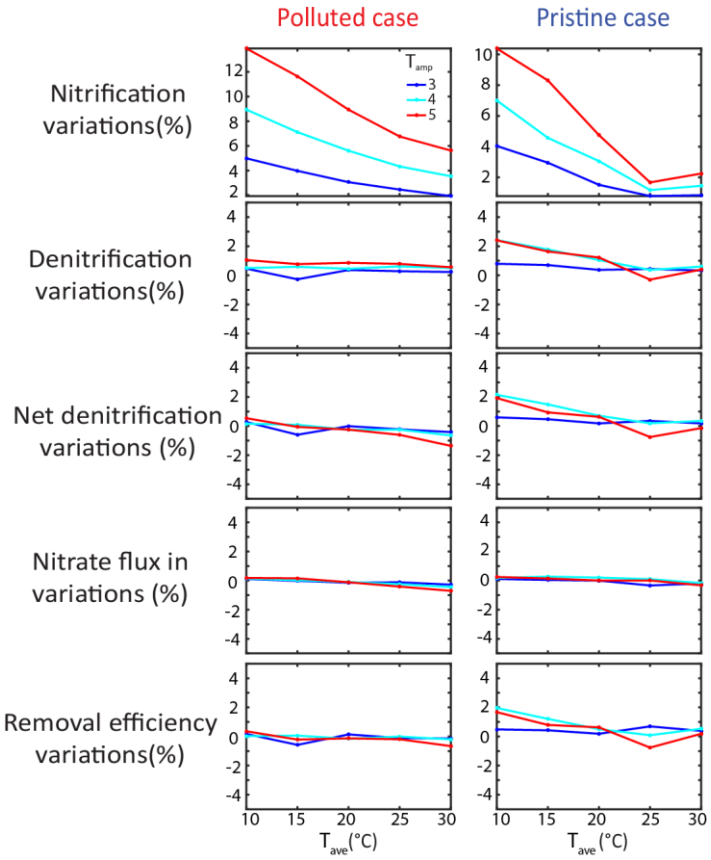

Figure 3.8: Comparison of various spatio-temporally-integrated reaction and transport metrics from the diel temperature simulations (with average temperature T_{ave} and temperature amplitude T_{amp}) relative to an equivalent steady temperature simulation.

question, we resorted to the analysis of the bulk value for nitrification, denitrification, and nitrate influx to quantify the bulk N_{RE}. We integrated the spatially-averaged reaction rates over 24-hours to get the bulk reaction rates and bulk N_{RE}. Then we compared the bulk N_{RE} with the corresponding value from equivalent constant temperature simulations (Figure 3.8). As expected, the bulk nitrification from dynamic simulations was about 10% larger than the nitrification rates from equivalent steady temperature simulations (Figure 3.8). This is because nitrification variations in the warm phase are always larger than the variations in the cool phase (Figures 3.6 and 3.7). However, the daily averaged denitrification from the dynamic temperature simulations can be considered as the same (variations within 3%) with the steady temperature simulation (Figure 3.8). In this study, the HZs for both polluted and pristine stream cases are denitrification dominant systems. Under this condition, net denitrification variations follow the diurnal denitrification pattern (Figures 3.6 and 3.7). Thus, the differences in daily averaged net denitrification between the dynamic temperature simulations and equivalent steady temperature simulations end up being negligible (Figure 3.8).

In addition, the daily averaged $[NO_3^-]_{in}$ from the dynamic temperature simulations were also similar to their equivalent steady temperature simulations. Since N_{RE} is the ratio of net denitrification to $[NO_3^-]_{in}$, the daily-averaged removal efficiency with dynamic temperature simulations was nearly identical to results of equivalent steady temperature simulations (i.e., the variations are within 3 %) (Figure 3.8). For the denitrification dominant stream, our study shows that a representative steady and uniform hyporheic temperature pattern can be assumed in determining daily averaged nitrate

removal efficiency in the HZ. However, for a nitrification dominant stream, its approximation as a steady hyporheic temperature system may not be appropriate.

3.5.2 Evidence and implication of temperature-dependent nitrate variation across different scales

Previous studies have shown that the daily in-stream nitrate concentration variation is inversely related to the diurnal stream temperature [*Heffernan and Cohen*, 2010]. That is, as the temperature reaches its minimum in the early morning, the stream exhibits its maximum nitrate concentration [*Cohen et al.*, 2012; *Rusjan and Mikoš*, 2010]. While in the late afternoon as the temperature rises and potentially peaks, the in-stream nitrate concentration reaches its minimum [*Cohen et al.*, 2012; *Halliday et al.*, 2013; *Heffernan and Cohen*, 2010; *Pellerin et al.*, 2009]. This is consistent with our simulation results, and based on our findings, this can be partly explained by warming stream temperature increasing denitrification and nitrate removal efficiency in the HZ for both the polluted and pristine stream scenarios. That is, the HZ will remove more nitrate which can then lower in-stream nitrate concentration at higher temperature, and vice versa. Consequently and in accordance with the diurnal temperature pattern, the in-stream nitrate concentration should exhibit the temperature-driven diurnally-varying biogeochemical processing in the HZ characterized by a minimum in the early afternoon and a maximum concentration in the morning.

Stream temperature not only varies daily but also changes seasonally. Previous studies demonstrated that the seasonal trends of stream nitrate concentrations have strong correlations with stream temperature. During the warmer months, in-stream water NO_3^-

and DO are low. In colder months, they are relatively high [*Christensen et al.*, 1990; *Halliday et al.*, 2013; *Rusjan and Mikoš*, 2010] . These observations are again in good accordance with our simulation results and suggests a role for temperature-dependent hyporheic biogeochemical processing. That is, the peak denitrification in the HZs would occur during the summer and lead to the minimum nitrate concentration. On the other hand, the low temperatures of the winter months are expected to result in minimum HZ denitrification, and thus the stream will have maximum nitrate concentrations.

At the even longer time scale, temperature has been shown to be negatively correlated with in-stream nitrate following two major characteristics [*Halliday et al.*, 2013]: (1) the annual temperature and nitrate concentration to some extent follow a sinusoidal pattern, and (2) the annual-mean in-stream nitrate concentration is decreasing while stream temperature is increasing. These observations are in general consistent with the lessons from our simulations and suggest that the results can potentially be extrapolated to longer time scales.

In sum, the strong quantitatively negative relations between stream temperature and in-stream nitrate concentration indicate that stream temperature can be one of the most important factors controlling the in-stream nitrate concentration cycles via temperature-dependent processes occurring in the HZ. Elevated (or reduced) denitrification occurring in the HZs driven by increasing (or decreasing) temperature is a likely root for this.

3.5.3 Limitations of the study

We simultaneously simulated fluid flow, heat transport and reactive solute transport with reaction rates dependent on temperature to study nitrogen dynamics in the HZs. The pressure distribution on the top boundary of the hyporheic zone (the SWI) was from the turbulent flow simulation above the domain. In the turbulent flow simulation, effects of the surface water temperature on flow were not considered. Thus, any consequential effects on the pressure distribution along the SWI were not considered, and we assumed that the pressure along the SWI remained static. That is the channel flow was perfectly steady. While this situation is not realistic and purely theoretical, it allows isolation of the effects of temperature on the hyporheic biogeochemical processing. In addition, I did not consider any thermal effects on stream DO concentration [*Veraart et al.*, 2011] in order to isolate and focus on the temperature effect on N dynamics. I did some steady state simulations considering about the temperature effect on stream DO concentration (Appendix A2). The results showed that nitrification rate in the shallow part of the HZ can be affected by the variable DO concentration due to temperature variations. However, the effect of variable DO concentration on denitrification rates in the HZ can be ignored (Appendix A2). Thus, for denitrification dominant system, temperature effect on stream DO concentration can be ignored. All stream solute concentrations were also kept constant in time, whereas these may vary in real field situations. Losing or gaining stream conditions would further complicate the physics [*Cardenas*, 2009], especially the thermal distribution in the HZ [*Cardenas and Wilson*, 2007c]; but here we assumed the stream is under neutral conditions and did not account

for possible feedback effects of the HZs and its discharge on the stream water. We also assumed that temperature effect on aerobic respiration and nitrification rate follow the Arrhenius equation and got its related parameters (i.e. activation energy) from literature. This study also focused on a single dune geometry and a single value of sediment dispersivity. All of the above factors could influence hyporheic exchange which drives the delivery of solute mass and energy, thus affecting the solute mass and thermal distribution and corresponding chemical reactions. Thus, there are many potential topics for future investigations. Our study helps set the foundation and direction for this.

3.6 SUMMARY AND CONCLUSIONS

Hyporheic zones (HZs) play an important role in nitrogen dynamics in freshwater ecosystems since they are preferential sites for biogeochemical reactions. While most biogeochemical reactions in HZs are strongly temperature-dependent, the effects of dynamic temperature on nitrogen cycling have been largely ignored. To this end, we conducted a series of numerical simulations sequentially coupling turbulent open channel flow, pore water flow, heat transport and reactive transport models, where chemical reactions in response to the changing temperatures were considered via the Arrhenius equation. Our results showed that spatially-averaged nitrification for all stream temperature scenarios followed the diurnal stream temperature signal and the supply rate of substrates to the HZ was synchronized with the temperature signal. This is because the temperature signal was quickly dampened with depth in the hyporheic zone, with only the shallow oxic zones where nitrification occurs subject to the large temperature swings. Thus, and in contrast, the spatially-averaged denitrification was not in synchrony with the

temperature signal, especially at lower temperatures, but became more aligned with the temperature signal with increasing average stream temperature. This is mainly due to upwards movement of the denitrification zone at higher temperatures and additional nitrate input from overlying nitrification areas. Nonetheless, the bulk nitrate removal efficiency for a day with daily varying temperature was effectively the same to that assuming temperature is constant (i.e., steady-state). This indicated the reliability of steady-state temperature solutions in reproducing the bulk nitrate removal efficiency. However, a steady temperature approximation would not adequately match the bulk biogeochemical effects of a nitrification-dominant system. Large variations throughout the day with complex patterns throughout the hyporheic zone suggested that previous and future in-situ observations may be biased or not representative of mean daily conditions.

Chapter 4: The dependence of hyporheic nitrogen cycling on ripple morphodynamics

4.1 ABSTRACT

River water quality and ecosystem health are strongly influenced by the biogeochemical processes occurring within hyporheic zones (HZs) which typically form due to the presence of bedforms. How the discharge- and grainsize-dependent equilibrium geometry of bedforms and how bedform migration affects hyporheic exchange flux, solute transport and reaction rates has not been investigated however, despite widespread spatiotemporal variation in river flow regimes. Here we investigate these processes through morphodynamically-consistent multiphysics numerical simulation experiments. We designed several realistic ripple geometries based on bedform stability dependent on mean river flow velocity and median grainsize. Then we determined the corresponding migration rate of ripples from the stream velocity. Hyporheic flow and reactive transport models of the migrating ripples were implemented to quantify nitrate transformations in the HZ or mobile bedforms, and these were compared with a base immobile-bedform simulation. We found that the "turnover" effect caused by bedform has a large impacts on supply rates and chemical reaction rates. The results showed that the nitrate removal efficiency increased asymptotically with Damköhler number for both mobile and immobile bedforms, but the immobile bedform always had a higher nitrate removal efficiency. Thus, moving bedforms remove less nitrogen. Considering bedform morphodynamics may therefore lead to reduction of

model estimates of ecosystem-scale reaction rates. The connection between nitrate removal efficiency and Damköhler number established here can be used as a framework for investigating transient, network-scale, HZ nitrate dynamics.

4.2 INTRODUCTION

Humans have greatly perturbed the global nitrogen cycle [*Gruber and Galloway*, 2008]. This perturbation has not only resulted in increasing amounts of nitrogen accumulated in ecosystems, but has also enhanced the transformation and transport of different N forms between the soil, water, and air [*Galloway*, 1998]. Excess reactive nitrogen has caused serious ecological and environmental issues[*Boano et al.*, 2014], including the degradation of water quality, coastal eutrophication and "dead zone" [*Craig et al.*, 2008], loss of biodiversity [*Alexander et al.*, 2000]. Stream and river beds have been recently recognized as actives site of nitrogen transformation due to biologically-active sediment and steep gradients in their redox environment [*Bardini et al.*, 2012; *Harvey et al.*, 2013; *Marzadri et al.*, 2012; *Zarnetske et al.*, 2012]. Rivers and their sediment play an important role in controlling the fate of nitrogen compounds, constraining N export to downstream waters that ultimately flow into the ocean [*Alexander et al.*, 2000; *Gomez et al.*, 2015; *Kiel and Cardenas*, 2014; *Peterson et al.*, 2001].

River sediments commonly form bedforms. A bedform is a morphological feature of the streambed formed by interaction between a flowing fluid and its underlying sediment. Bedform morphology can strongly influence the spatial distribution of solute species and biogeochemical reaction zones in sediment due to porewater exchange

through the hyporheic zone (HZ) [*Buffington and Tonina*, 2009; *Cardenas*, 2008b; *Harvey et al.*, 2012; *Marzadri et al.*, 2012]. Bedforms drive hyporheic exchange through two mechanisms, namely "pumping" and "turnover" [*Elliott and Brooks*, 1997a]. "Pumping" is the interstitial movement of fluid through the streambed due to irregular bedform geometry which produce pressure gradients along the sediment-water interface. While "turnover" occurs when a bedform migrates; as a bedform migrates, it captures and releases water in its pore spaces. The contributions from these two mechanisms to hyporheic exchange flux were well studied [*Packman and Brooks*, 2001].

Recently, many studies have focused on denitrification in HZs and in trying to understand and predict the function of HZs in nitrogen cycling. In particular, studies have focused on whether HZs serve as a nitrate sink or source and what the determining factors are [*Boano et al.*, 2010; *Kessler et al.*, 2015; *Marzadri et al.*, 2012; *Zarnetske et al.*, 2012; *Zheng et al.*, 2016]. However, most of the previous research assumed the bedforms were immobile. *Kessler*'s study [2015] was a recent exception in that they considered the effect of bedform migration on N transformations. However, that study applied a given pressure distribution on a flat sediment-water interface to fictitiously represent the irregular topography.This assumption did not consider the variable boundary conditions due to the moving bedforms. For example, as bedform migrates, water can also enters into the HZ from the lee side of the bedform. Kessler's study [2015] assumes that the bedform is flat, it ignores the triangle part of the bedform. This would result in inaccurately depicting the flow field and estimating the flux of hyporheic flow, thus influence the spatial pattern of solutes and biogeochemical reactions.

Bedforms are naturally prone to be mobile due to the presence of elevated shear stress applied on the sediment water interface during periods of sufficiently high river flow. Bedform movement can dramatically influence the hyporheic flow field [*Ahmerkamp et al.*, 2015], increase the exchange of solutes between streams and the hyporheic zone [*Packman and Brooks*, 2001], alter oxygen dynamics [*Precht et al.*, 2004], produce a more hostile environment for benthic microorganisms[*Rutherford et al.*, 1993], and influence organic matter retention, decomposition and metabolism [*Harvey et al.*, 2012]. Thus, it is crucial to study nitrogen dynamics of the HZ while considering bedform celerity rather than assuming immobile bedforms, which most studies have done so far. This is the goal of this study: to characterize hyporheic nitrogen cycling in mobile bedforms and to compare them with their immobile counterparts. In the process, we hope to find patterns that eventually lead to predictive models.

Ripples and dunes are the two most common bedform types in rivers. Since ripple geometry is independent of water depth [*Garcia*, 2008], but mainly controlled by mean sediment grain size, we only considered ripples in this study for simplicity and as a starting point. Given a specific characteristic grain size, ripples can be in equilibrium within a narrow range of stream velocities according to the bedform stability diagrams. The so-called equilibrium does not refer to a static bedform; in fact, the bedform moves and adjusts its morphology in a dynamic equilibrium. However, it can be assumed that the bedform geometry remains mostly unchanged if the stream velocity varies within a particular range. We used the bedform stability diagram along with the criterion of the ripple formation to establish ripple geometries. We considered seven different mean grain

size scenarios, corresponding to seven different ripple geometries (Appendix A3,Table A3.1). Sediment grain size (assumed to be uniform and thus equals to D_{50}) is the only parameter that controls the ripple geometry following empirical equations [*Baas*, 1999; *Garcia*, 2008].

Moreover, the mean stream velocity constrains the bedform formation and celerity. Thus, for each specific ripple geometry, we considered different stream velocities and its corresponding bedform celerity. We compared the hyporheic flux, flow field, solute species spatial distribution, effective nitrification and denitrification reaction zone, and nitrate removal efficiency of the immobile bedform to those of the mobile bedform. To our knowledge, this is the first systematic study of coupled hydrologic, biogeochemical, and geomorphological processes of hyporheic zones.

4.3 METHODOLOGY

4.3.1 Choice of representative bedform geometry (ripple)

Bedform type and geometry depends upon the flow velocity and depth, and sediment grain size. A bedform stability diagram shows what types of bedform are in equilibrium for a given sediment grain size and flow velocity. The diagram is empirical based on a large number of field and experimental data. In this study and for simplicity, we only considered ripples since their shapes are only controlled by sediment size rather than flow depth, allowing to eliminate one variable that also changes a lot in rivers. We used the bedform stability diagram (Figure 4.1) together with the criterion for forming the bedform as discussed below to establish our ripple geometry.

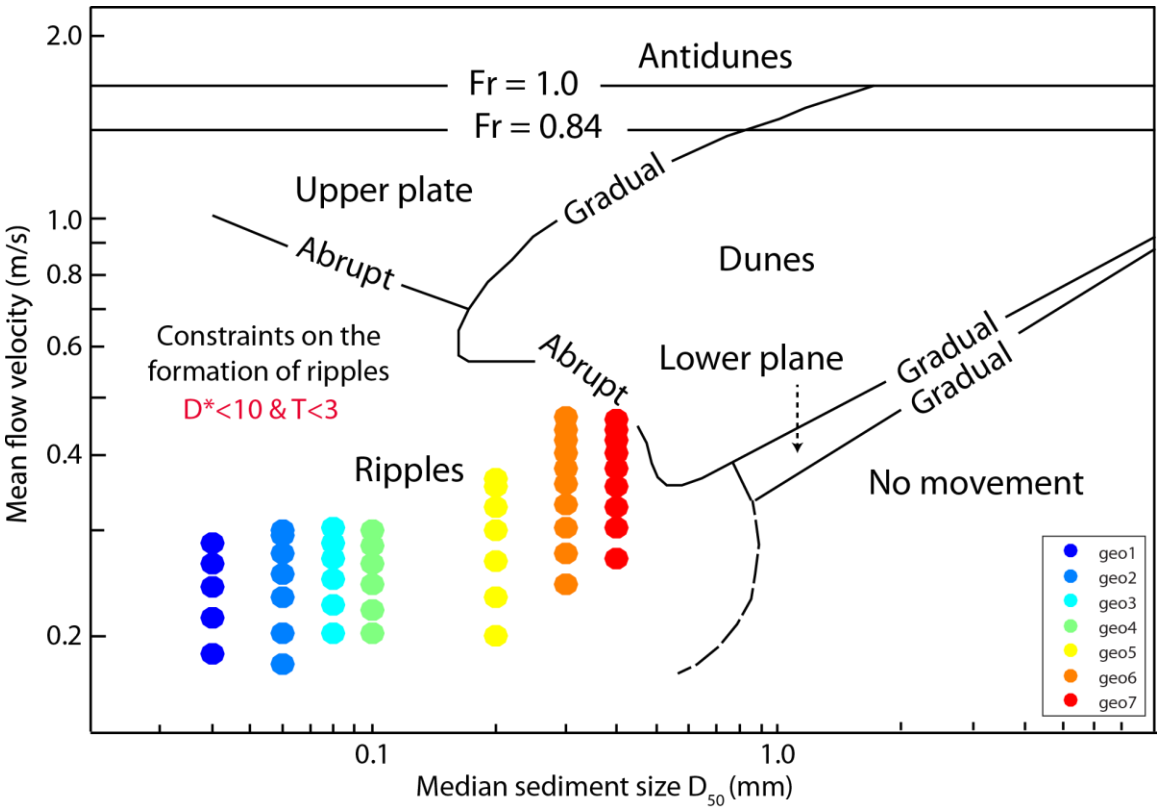

Figure 4.1: Seven ripple geometry (50 cases) were chosen for study based on the bedform stability diagram (adapted from Ashley 1990).

4.3.1.1 Criterion for ripple formation

We considered two criteria for constraining bedform formation which are generally based on the Froude number (F_r) or stream velocity.

The *Fr* is a metric based on the ratio of inertial force to the gravity:

$$F_r = \frac{U}{\sqrt{gH}} \tag{4.1}$$

where U is velocity, g is gravitational acceleration, and H indicates flow depth. Since both dunes and ripples are characteristic of low subcritical flow regime in terms of F_r, *Karim* [1995] proposed a bedform threshold predictor (F_t):

$$F_t = 2.716\left(\frac{H}{D_{50}}\right)^{-0.25} \tag{4.2}$$

where D_{50} is the mean sediment grain size. The F_t indicates the beginning of the transition regime beyond the limit of low subcritical flow regime, and therefore sets the limit for the existence of ripples and dunes; that is, the presence of dunes and ripples only exists if:

$$F_r \leq F_t \tag{4.3}$$

Van Rijin's diagram [*Garcia*, 2008; *van Rijn*, 1984a; 1993]indicated that ripples are present when both conditions are satisfied: the dimensionless particle parameter $D^* < 10$ and the transport stage parameter $T < 3$. These metrics are calculated following:

$$D^* = D_{50}\left[\frac{(s-1)g}{v^2}\right]^{1/3} \tag{4.4}$$

$$T = 2\frac{(u_*')^2 - \left(u_{*,cr}\right)^2}{\left(u_{*,\mathrm{cr}}\right)^2} \tag{4.5}$$

where s is specific gravity, $u_*'$is the bed-shear velocity related to grains, $u_{*,cr}$ is the critical bed-shear velocity according to Shields diagram [*Van Rijn*, 1984b]. u_*' is fundamentally controlled by the mean flow velocity. Detailed explanations can be found in [*Garcia*, 2008; *van Rijn*, 1984a].

4.3.1.2 Dimensions of the equilibrium ripple geometry

According to the Van Rijn's diagram for ripple formation (D*<10), ripples only develop in fine grained sediments (D_{50} < 0.4 mm). We therefore chose seven values of D_{50} ranging from 0.04 mm to 0.4 mm in this study. Each D_{50} determines the wavelength and height of ripples as described below, so we worked on seven ripples geometries.

Baas [1999] proposed the following equations for ripple wavelength (L) and height (Δ) at the equilibrium state:

$$L = 75.4\log D_{50} + 197 \tag{4.6}$$

$$\Delta = 3.4\log D_{50} + 18 \tag{4.7}$$

where L, D_{50} and Δ are all in unit of mm. Bedforms under unidirectional flows are generally asymmetric, with a gentle stoss side facing upstream and a steeper lee side downstream. We chose the lee side angle as 30° [*Paarlberg and Winter*, 2013]to build our ripple geometry here.

For a given D_{50}, the ripple geometry can be in a dynamic equilibrium and remains unchanged with a relatively small range of flow velocity according to the bedform stability diagram. Taking our designed geometry 6 (D_{50} = 0.3 mm) as an example (Appendix A3, Table A3.1), when the mean stream velocity varies from 24 cm/s up to 46 cm/s, the shape of ripple geometry remains more or less constant with particular L =

157.57 mm and Δ = 16.22 mm according to (6-7). Moreover, the stoss side angle for geometry 5 is 7.14°, with the crest shifted on the right (*Lc*=129.48mm), and the aspect ratio of wavelength to height is 9.71 (see schematic Figure 2.1).

In combination of the criterion for bedform formation and the bedform stability diagram, we designed 50 cases (Appendix A3, Table A3.1 and Figure 4.1) with different D_{50} and mean flow velocities to study the effect of moving bedform on nitrate dynamics within the HZ. Among them, we have 7 different ripple geometries, and each geometry corresponded to a few associated mean flow velocities. For instance, we simulated 10 cases with incremental mean stream velocity =2-3 cm/s within the range of 24 - 46 cm/s for geometry 6 (Figure 4.1).

4.3.1.3 Calculation of ripple celerity

Coleman and Melville (1994) proposed a relationship between the celerity (c) of small bed forms as a function of bed form height and mean flow velocity terms for small ripples:

$$\frac{c}{[(u_* - u_{*cr})(\theta - \theta_c)]}(\Delta/D_{50} - 3.5)^{1.3} = 40 \tag{4.8}$$

where θ_c is Shields' parameter at entrainment. Equation (4.8) indicates that c generally decreases with increasing Δ. Since Δ and $u_{*,cr}$ are fundamentally connected to D_{50}, and u_* is intrinsically connected to the mean flow velocity, the bedform migration rate, i.e., c, thus varied for each ripple geometry at each specific mean flow velocity. The estimated c are shown in Appendix A3, Table A3.1.

4.3.2 Numerical modeling setup

After establishing the representative morphodynamic conditions, these are used for multiphysics simulations of open channel flow, hyporheic flow, and hyporheic reactive transport. Channel water flow and pore water flow were sequentially coupled following the computational fluid dynamics (CFD) approach of Cardenas and Wilson (2007a). In this framework, the turbulent flow field is first modeled independently. The resulting pressure distribution along the SWI from the turbulent flow model is then imposed as a Dirichlet boundary condition driving a pore water flow model of the HZ. The resultant groundwater velocity field is finally used as input for modeling multi-component reactive transport. The key details of the models are described below.

4.3.2.1 Fluid flow models (turbulent flow and Darcy flow)

Steady state two-dimensional turbulent channel flow over the bedforms was simulated by numerically solving a finite-element formulation of the Reynolds-averaged Navier-Stokes (RANS) equations. For an incompressible and homogeneous fluid, the RANS reads as:

$$\frac{\partial U_i}{\partial x_i} = 0 \tag{4.9}$$

$$\rho U_j \frac{\partial U_i}{\partial x_j} = -\frac{\partial P}{\partial x_i} + \frac{\partial}{\partial x_j}\left(2\mu S_{ij} - \rho\overline{u_j' u_i'}\right) \tag{4.10}$$

Where ρ and μ are fluid density and dynamic viscosity, P is time-averaged pressure. i, j=1, 2 are the spatial indexed corresponding to x and y directions. U_i (i=1,2) and u_i'

(i=1,2) are the time-averaged and instantaneous velocity components in x_i (i=1,2) directions. S_{ij} is the strain rate tensor defined as:

$$S_{ij} = \frac{1}{2}\left(\frac{\partial U_i}{\partial x_j} + \frac{\partial U_j}{\partial x_i}\right) \tag{4.11}$$

The Reynolds stresses are related to the mean strain rates by:

$$\tau_{ij} = -\overline{u_j' u_i'} = v_t(2S_{ij}) - \frac{2}{3}\delta_{ij}k \tag{4.12}$$

where v_t is the kinematic eddy viscosity, δ_{ij} is the Kronecker delta, and k is turbulent kinetic energy. We adopt k- ω turbulence closure scheme with the eddy viscosity v_t, the specific dissipation ω, the turbulence dissipation rate ε, and the closure coefficient β*.

$$v_t = \frac{k}{\omega} \tag{4.13}$$

$$\omega = \frac{\varepsilon}{\beta^* k} \tag{4.14}$$

The steady state transport equations for k and ω are:

$$\rho\frac{\partial(U_j k)}{\partial x_j} = \rho\tau_{ij}\frac{\partial U_i}{\partial x} - \beta^*\rho\omega k + \frac{\partial}{\partial x_j}\left[(\mu + \mu_t\sigma_k)\frac{\partial k}{\partial x_j}\right] \tag{4.15}$$

$$\rho\frac{\partial(U_j \omega)}{\partial x_j} = \alpha\frac{\rho\omega}{k}\tau_{ij}\frac{\partial U_i}{\partial x_j} - \beta\rho\omega^2 + \frac{\partial}{\partial x_j}\left[(\mu + \mu_t\sigma_\omega)\frac{\partial \omega}{\partial x_j}\right] \tag{4.16}$$

RANS-derived pressure distributions at the bottom of the turbulent flow domain obtained from the above equations will be used as a boundary condition for the subsurface ripple domain.

The pressure field (or head field) in the HZs will be numerically approximated by solving the Laplace (or groundwater flow) equation:

$$\frac{\partial^2 H}{\partial x_i^2} = 0 \tag{4.17}$$

where H is total water head. The velocity in the HZs can be estimated according to the Darcy's law with given H gradient:

$$u_i = K\frac{\partial H}{\partial x_i} \tag{4.18}$$

where K is hydraulic conductivity, u_i is the velocity in the i direction. Since we are investigating moving bedforms, we introduced a frame of reference moving with bedform migration rate c to represent the effect of bedform celerity following [*Bottacin-Busolin and Marion*, 2010; *Kessler et al.*, 2015]. That is, the horizontal pore velocity should have the bedform celerity c subtracted from it. Then u_x-c, the celerity-corrected flow field which now includes turnover, was further used as an input for solving transport equations. The moving bedform have no effect on the vertical velocity. This method assumes the bedform moves at average rate, which is the overall effect of physical grain movement. Thus, the flow field is

$$\begin{cases} v_x = u_x/\theta - c \\ v_y = u_y/\theta \end{cases} \tag{4.19}$$

4.3.2.2 Multi-component reactive transport model

The HZ is a hotspot for geochemical reactions partly due to the interaction of stream water and pore water in the sediment [*Boulton et al.*, 1998; *Fischer et al.*, 2005; *Roley et al.*, 2012]. In terms of nitrate transformation in the HZ, we considered three major chemical reactions, including aerobic respiration, denitrification, and nitrification as described by [Zheng et al., 2016]. Four reactive components are involved in this study:

dissolved organic carbon (DOC), dissolved oxygen (DO), nitrate (NO_3^-), and ammonium (NH_4^+). Other nitrate-relevant reactions are neglected in this study.

The details of sequential chemical reactions and associated reaction rates can be found in *Zheng et al.* [2016]. Here, we only emphasized the key features of chemical reactions. The microbial degradation of DOC acts as the main source of chemical energy, and therefore is assumed to be the primary reaction [*Hunter et al.*, 1998] that simply follows the first-order rate law [*Bardini et al.*, 2012]:

$$r_{\mathrm{DOC}} = k_{\mathrm{DOC}} \cdot [DOC] \tag{4.20}$$

where k_{DOC} is the first-order reaction rate constant; brackets indicate the actual activity of DOC rather than its concentration. The knowledge of r_{DOC} can be further applied to estimate the reaction rates for aerobic respiration (19-1) and denitrification (19-2) processes. Moreover, the nitrification (19-3) follows the bi-molecular rate law:

$$r_{\mathrm{NH_4^+}} = k_{\mathrm{NH_4^+}} \cdot [\mathrm{NH_4^+}] \cdot [\mathrm{O_2}] \tag{4.21}$$

where $k_{\mathrm{NH_4^+}}$ is the nitrification molar rate coefficient.

The reaction kinetics above were employed to estimate the magnitude of sink or source term (R) for simulating the fate of each component in the HZ. At steady state, the component concentration is governed by the solute transport equation with sink/source terms R:

$$\nabla \cdot \left(-\theta D \nabla C_j + v \cdot C_j\right) = \theta R_j \tag{4.22}$$

where θ is the sediment porosity, j represents DOC, O_2, NO_3^-, NH_4^+, D is a dispersion tensor and C_j is the concentration of the component j, v is the flow velocity (Equation 19). The solution for the component concentration can be directly used for estimating R.

We assumed that the porous sediment is initially free of components. The well-mixed components in the stream will be transported from stream and through sediment driven by advection and dispersion. Note that in-stream component concentrations were constant in time so that these were specified as a Dirichlet inlet boundary along portions of the SWI. The portions along the SWI where water exits out from the HZ was specified as an open boundary; that is, no dispersive flux occurred at these boundaries.

4.3.3 Calculation of mean residence time of hyporheic exchange

The mean residence time indicates is the time it takes for a fluid or fluid-borne solute to enter from the stream, flow or be transported through the sediment, and eventually leave the sediment and return to the stream. At flow outlets, the mean residence time can be interchangeably used for age if we choose the age = 0 at inflow sections of the SWI where stream water enters into the sediment [*Goode*, 1996]. Note that residence time is different from flushing time [*Monsen et al.*, 2002]. Flushing time normally refers to the total or effective volume of flowing body divided by the flow rate, which has been often used for HZ studies [*Cardenas et al.*, 2008; *Gomez et al.*, 2012].

To estimate the residence time for the HZ, we first solve the age-mass transport equation as presented by [*Goode*, 1996]:

$$\frac{\partial(\theta\tau)}{\partial t} + \nabla \cdot (v\tau) = \nabla \cdot (\theta D \cdot \nabla\tau) \tag{4.23}$$

where θ is sediment porosity, τ is age mass, v is flow velocity, D is dispersion coefficient tensor. Solving (23) yields the field for τ which usually has a wide range especially at the SWI. However, none of the distributed τ along the SWI is representative of the HZ. Thus, like the traditional method used for estimating breakthrough curves from experiments and field survey [*Haggerty et al.*, 2002; *Zarnetske et al.*, 2011], we applied the flux-weighted τ to estimate mean τ at SWI; that is, the weighting coefficient for the distributed τ along the SWI is its associated local flux (normalized by the total flux) as determined from solving the Darcy's equation.

The mean τ at the SWI was used for estimating the Damköhler number (Da) in terms of DOC:

$$Da = \tau k_{DOC} \tag{4.24}$$

where k_{DOC} represents the first-order reaction rate constant for DOC [*Zheng et al.*, 2016]. Hereafter, Da only refers to reactions that involve DOC rather than other reactants in this study. Since k_{DOC} is specified to be constant as we assumed a constant temperature in space and time in the HZ, Da is thus proportional to the τ. As such, the low Da most often represents the HZ with high D_{50} and thus high exchange flux.

4.3.4 Numerical implementation in the COMSOL Multiphysics finite-element model

For each given bedform geometry determined by the stream velocity and grain size, we solved the equations above using COMSOL Multiphysics, a commercial finite-element solver. These include solving the RANS to obtain pressure along the SWI, solving the Darcy's flow equation to yield Darcy velocity in the HZ at steady state, solving the steady-state transport equations for calculating chemical reaction rate, and

solving the age-mass equation to estimate mean residence time. The boundary conditions were the same to our previous study [*Zheng et al.*, 2016]. In our numerical schemes, we employed different permeability for different ripples as D_{50} changed (Appendix A3, Table A3.1), but the same porosity = 0.372 and longitudinal dispersivity =3 cm, and transverse dispersivity =0.3 cm for all cases. We used empirical equation *permeability*= $7.35\times10^{-6}\times D_{50}^2$ (m^2) [*Gangi*, 1985].

In previous similar multiphysics/multi-domain modeling studies, the turbulent flow was modeled using a different solver [*Bardini et al.*, 2012; *Cardenas and Wilson*, 2007a], but then COMSOL was used for modeling the subsurface. This approach has been shown to work well with COMSOL performing robustly in terms of modeling the Darcy flow field and transport equations related of the HZ. Here, we used COMSOL to model all equations. Thus, we first validated that COMSOL is sufficiently accurate and robust in reproducing the flow in the open channel by tuning parameters in the RANS module; details of validation are shown in the result section.

4.4 RESULTS

4.4.1 Validation of interfacial pressure modeled by COMSOL

The numerically-estimated pressure distributions along the SWI was validated by comparing the simulation results to the experimental measurements by *Janssen et al.* [2012]. Seven identical current-type ripples with rounded troughs and crests and 5 cm long planar sections on the upstream and downstream end were built following Janssen's experiment (Figure 4.2). Water depths was 10 cm above troughs. Two mean stream

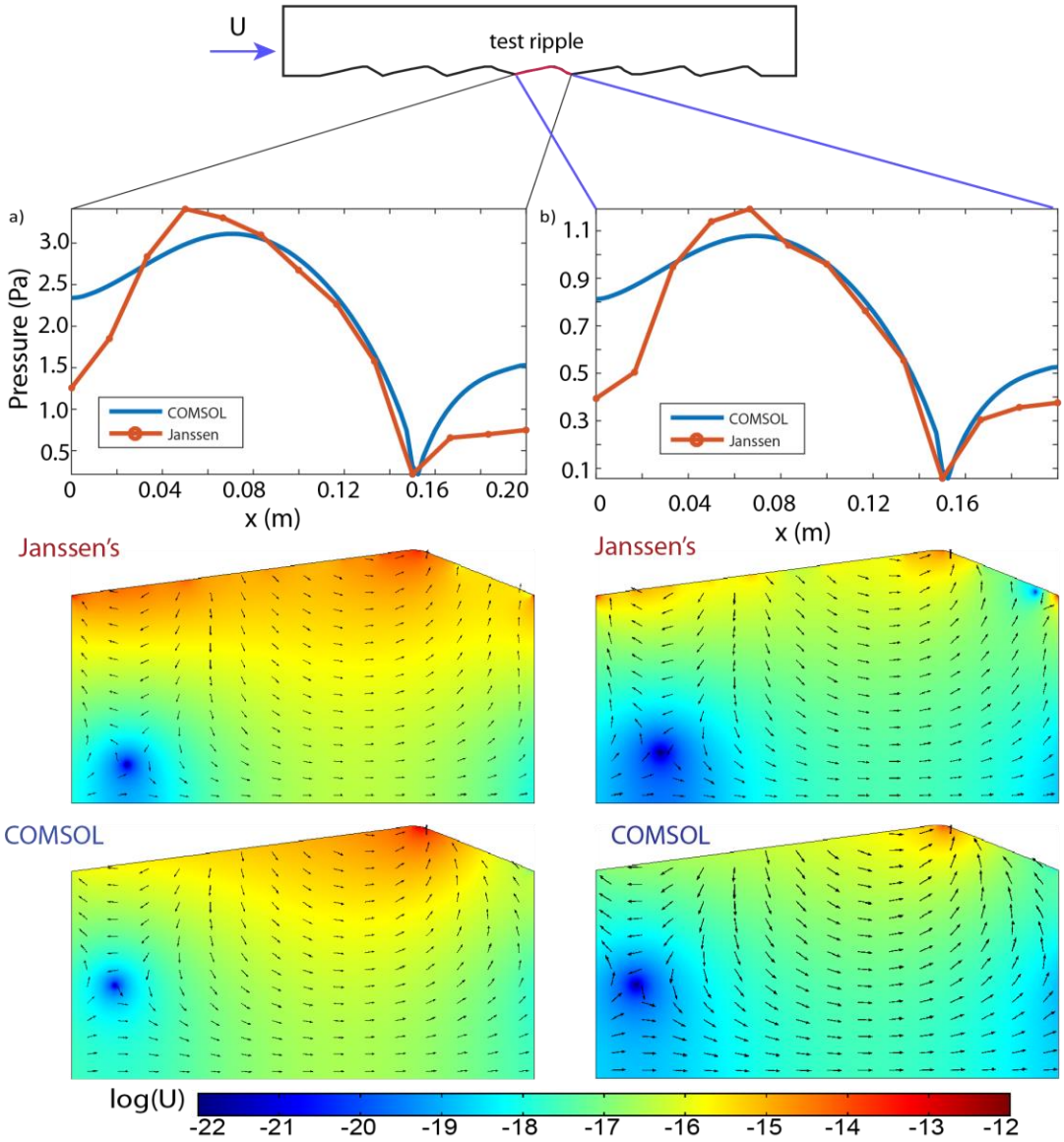

Figure 4.2: Top: comparison of measured (from Janssen's experiment) and modeled pressure distribution along the sediment-water interface for (a) high discharge case (b) low discharge case. Middle: the magnitude of velocity and flow field with Janssen's experiment pressure data. Bottom: the magnitude of velocity and flow field with our modeled pressure.

velocities [*Cardenas et al.*, 2008] that correspond to low-discharge (2.1L/s) and high-discharge (3.6 L/s) flume experiments were simulated.

We first compared the pressure of the test ripple from our COMSOL simulation with the measured pressure from Janssen's flume experiment (Figure 4.2). The overall patterns of pressure distributions along the test ripple's SWI were mostly similar. The amplitude of the pressure variation across the bed form from our simulation was slightly larger (within 10%) in comparison with experimental measurements for both discharge cases. The relative and acceptable errors were all within 10%.

Additionally, we compared the magnitude of velocity and flow field driven by the measured and simulated pressures at the SWI of the ripple (Figure 4.2). By solving Darcy's equations in the HZ, we found that the magnitude of pore water velocity was identical to each other using the measured and simulated pressures.

Since we were more concerned about the solute transport in the HZ, we released a conservative tracer to identify the differences of the solute propagation process with modeled pressure and measured pressure (Figure 4.3). Our results showed that the size and shape of the plume using the simulated pressure fairly matched that of using the measured pressure, although the solute propagation front with measured pressure was not smooth as that with modeled pressure. In sum, the deviation of pressure by solving the RANS from experimental results led to slight differences in flow and transport processes.

4.4.2 The "turnover" and "pumping" effects on flow field and flux exchange

As the bedform migrates, the boundary condition changes (Figures 4.4a and 4.4b). This would result in varying hyporheic flux for the mobile bedform and immobile

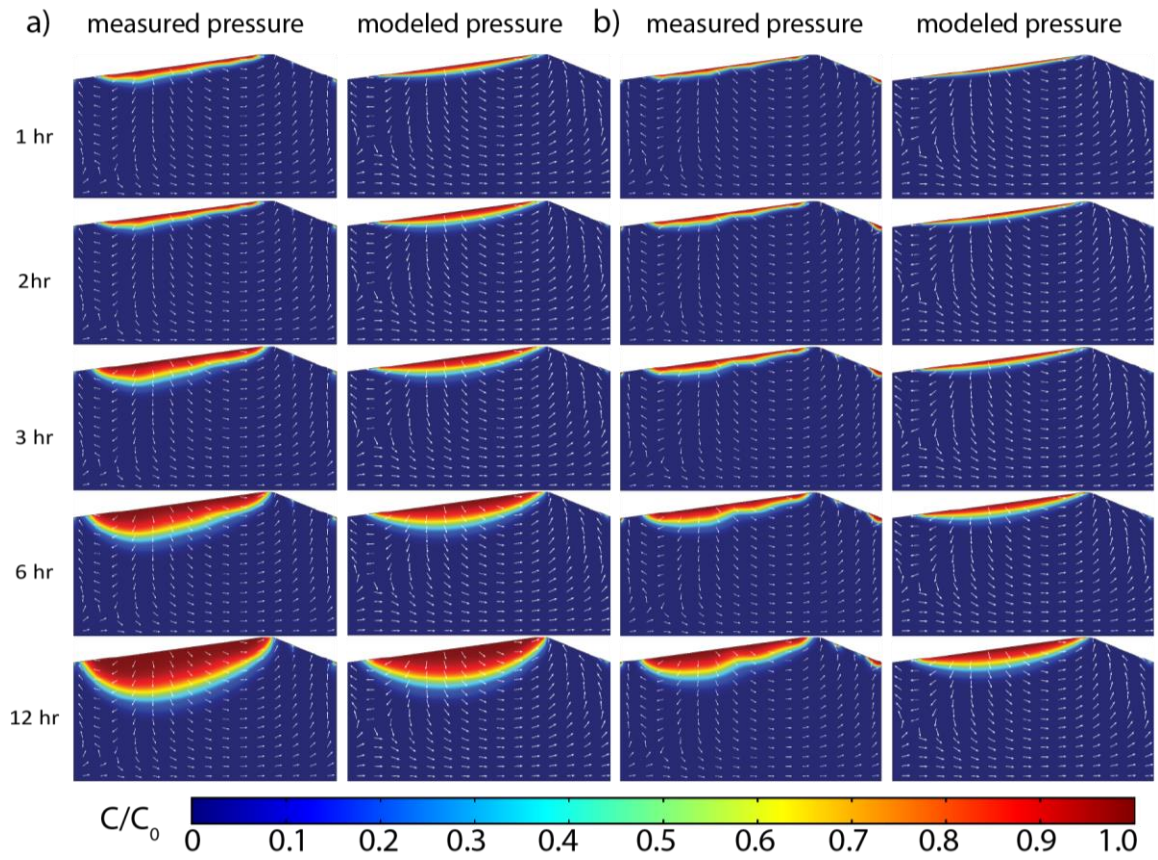

Figure 4.3: Comparison of snapshots of concentration front changing with time in the sediment for a) high discharge case b) low discharge case. left: simulation with measured pressure as driving force, right: simulation with modeled pressure from COMSOL as driving force.

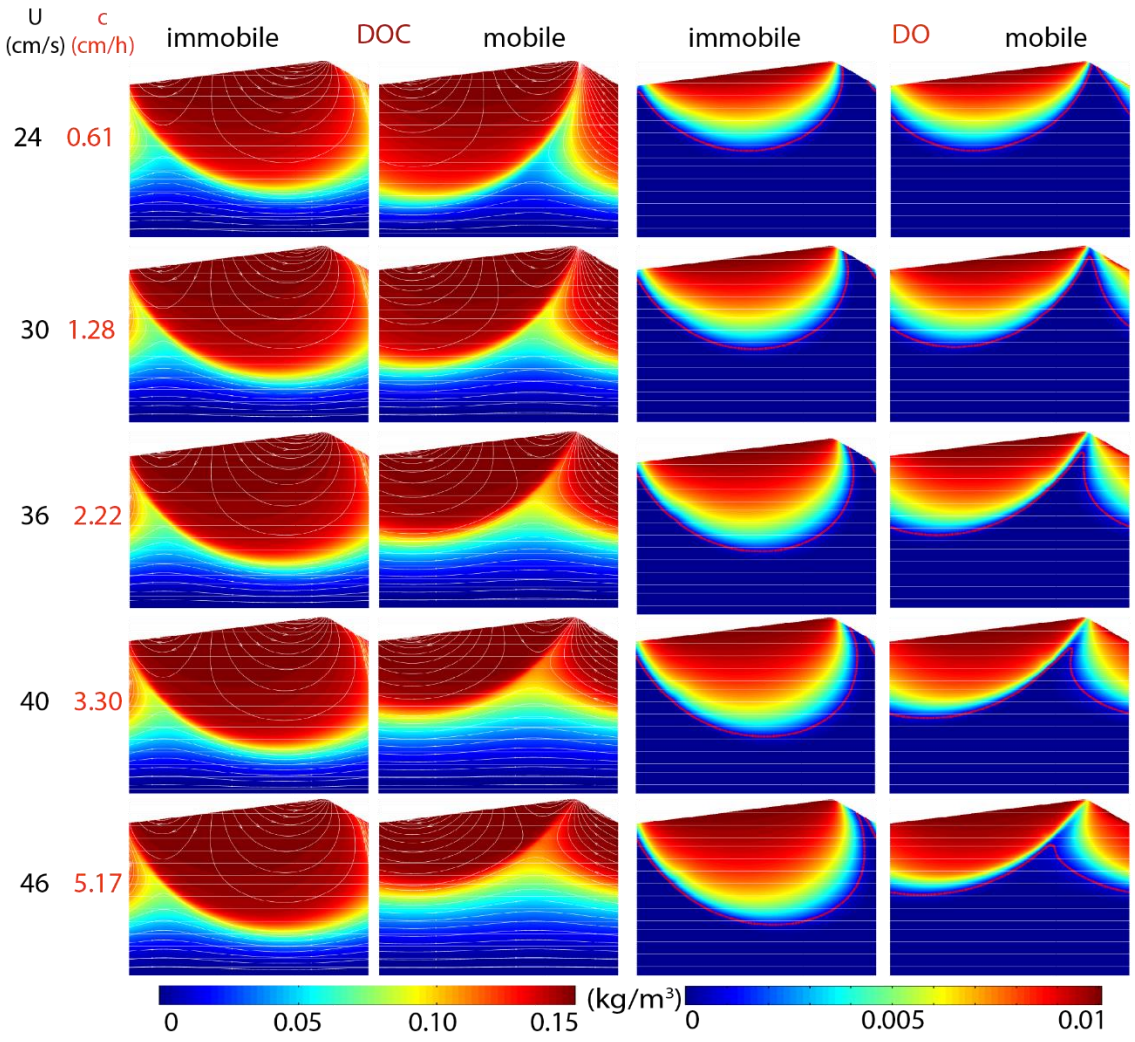

Figure 4.4a: Comparison of solute distribution (DOC and DO) of immobile and mobile bedform for geometry 6 with increasing stream velocity *U* and corresponding bedform celerity *c*. White lines with arrows indicate streamlines. Channel - flow is from left to right. Red dotted lines represent oxic-anoxic boundary.

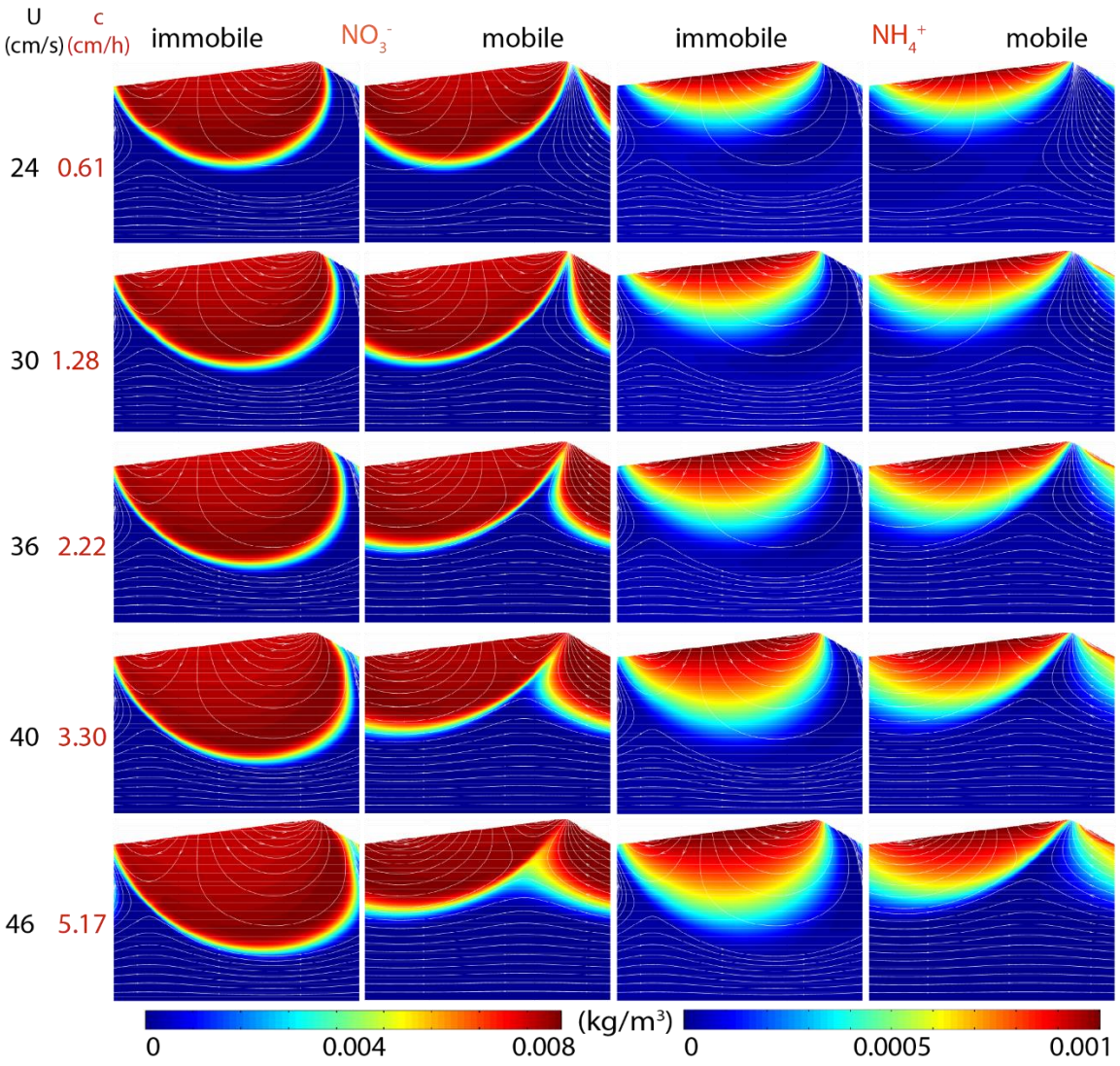

Figure 4.4b: Comparison of solute distribution (NO_3^- and NH_4^+) of immobile and mobile bedform for geometry 6 with increasing stream velocity *U* and corresponding bedform celerity *c*. White lines with arrows indicate streamlines. Channel flow is from left to right.

bedform. We hypothesized that hyporheic flux for the mobile bedform would be larger than that for the immobile bedform, this was expected since a previous study proposed that more oxygen is flushed into the HZ as the bedform migrates [*Rutherford et al.*, 1993, *Ahmerkamp et al.*, 2015]. We found the opposite in this study; that is, the hyporheic flux is not always larger as the bedform migrates.

The turnover effects with increasing bedform celerity (c) on exchange flux depended on D_{50}, i.e., ripple shapes. For different bedform geometry cases with $D_{50} < 0.1$ mm, the hyporheic flux for the mobile bedform was larger than that for their corresponding immobile bedform. However, with $D_{50} >= 0.1$ mm, hyporheic flux for the mobile bedform was smaller than that through the immobile bedform. This is attributable to the competing flux caused by pumping and turnover since the pumping effect drives water into sediment from the stoss side of SWI, while turnover drives water into sediment from the lee side of SWI. Specifically, the turnover effect due to bedform movement cannot compete with the pumping effect when D_{50}, i.e., K is large (K is a function of square of D_{50}), as such the turnover effect only effectively reduces the exchange flux from the stoss side. This was clearly demonstrated by: (a) the ratio of hyporheic flux for the immobile bedform to that for mobile bedform was less than 1, and (b) this ratio decreased with increasing stream velocity. For the small grain size geometry cases, the turnover effect exceeded the pumping effect. Since c increased correspondingly with increasing stream velocity. The difference in hyporheic flux between mobile and immobile increases with increasing c if turnover exchange is dominant over pumping (Appendix A3 Table A3.2).

4.4.3 Comparison of solute distributions for mobile bed form and immobile bed form

We focus on geometry 6 (D_{50}=0.3 mm) to scrutinize the solute reactive transport process and how these are affected by bedform mobility. The triangular bed form has a length of 157.6 mm and height of 16.2 mm with crest located at 129.5 mm. The distribution of four species (DOC, DO, NO_3^-, NH_4^+) across increasing stream velocity and corresponding bedform celerity were analyzed (Figures 4.4a and 4.4b).

There were obvious differences between the mobile and immobile cases' flow fields and boundary conditions. For the immobile bedform, there were two distinct flow cells in the sediments (Figures 4.4a and 4.4b). One was circulating clockwise (upstream), and the other was circulating counterclockwise (downstream); both of these flow cells originate from the stoss side of the bedform. The streamline shows that underflow was from left to right. Solute in the stream entered into the bedform sediment through the middle part of the stoss side of the ripple, and after a short flow path, exited the sediment through the lee side of the ripple (some through the stoss side), and went back to the stream.

There was one more flow cell for the mobile bedform. The additional flow cell originates from the right part and lee side of the bedform, and returns to the SWI at the crest. The general direction of the underflow was from right to the left, opposite to the immobile bedform. The average or dominant flow direction reversed even at the smallest stream velocity and bedform celerity due to small velocities by pumping. The solutes

from the stream entered into the sediment through both lee and stoss sides of the ripple and this pattern changed with increasing stream velocity and bedform migrating rate.

The flow field regulates the solute distributions. Based on Darcy velocity distribution, the SWI can be divided as the influx and efflux sections. We employed an open boundary for the interface, that is, the influx zone has a constant concentration which is the same as the stream solute concentration; the efflux zone releases the solute out from the HZ due to convection and not diffusion or dispersion. As expected, a mobile bedform exerted a substantial effect on solute distributions due to switching boundaries from influx to efflux. The shapes of the solute plumes were different with mobile and immobile bedforms. The four solutes for the immobile bedform had a cresent-shape, while their distribution within the mobile bedform had two separated convex zones which converged below the crest. This was because the influx into the HZ occurred only through the stoss side of the HZ within the immobile HZ, while the solute can also enter into the HZ through both the stoss and lee side of the mobile HZ. The size of the right part of the plume increased with increasing stream velocity and corresponding bedform celerity.

The penetration depths of the solute plumes were also different. At low stream velocity and associated celerity, there was a trivial difference between mobile and immobile HZs. With further increases in stream velocity and thus hyporheic exchange flux, the penetration depth of the solutes increases for immobile bedform (Figure 4.4a and 4.4b). However and unlike immobile cases, the penetration depth of each solute species decreased with increasing stream velocity and increasing bedform celerity for the

mobile bedform (Figure 4.4a and 4.4b). In addition, and compared to the immobile bedform, the penetration depth was relatively smaller (10-20cm) for the mobile bedform with the same stream velocity (Figure 4.4a and 4.4b).

4.4.4 Impact of bedform celerity on denitrification and nitrification

The mobile and immobile bedforms imposed different effects on solute distribution, and thus controlled the biogeochemical reaction zones. Here we focus more on the individual species and their individual and integrated reaction rates.

(1) For the immobile bedform cases, the $NH_4^+$and DO distributions had a crescent-shape for the immobile bedform as explained previously (Figures 4.4a and 4.4b), the nitrification zone followed the DO distribution according to nitrification reactions (4.19c). Moreover, the nitrification zone penetrated into deeper zone as the stream velocity increased for immobile bedform. Like the nitrification zone, the denitrification zone also became deeper with increasing stream velocity, and the deepest part shifted from the left of the domain at low stream velocity to the right at high stream velocity (Figure 4.5). The distribution of the DO regulated the nitrification zone and denitrification zone.

(2) For the mobile bedform cases with three flow cells, denitrification zones were two separated belt-shape or crescent-shape. These two zones diverged at the crest of the bedform (Figure 4.5). With increasing stream velocity and associated *c*, the degree of the curvature of the crescent shape became smaller. Meanwhile, the convergence point of the two crescent shapes slightly shifted from the crest at low stream velocity to the left of the crest and moved deeper.

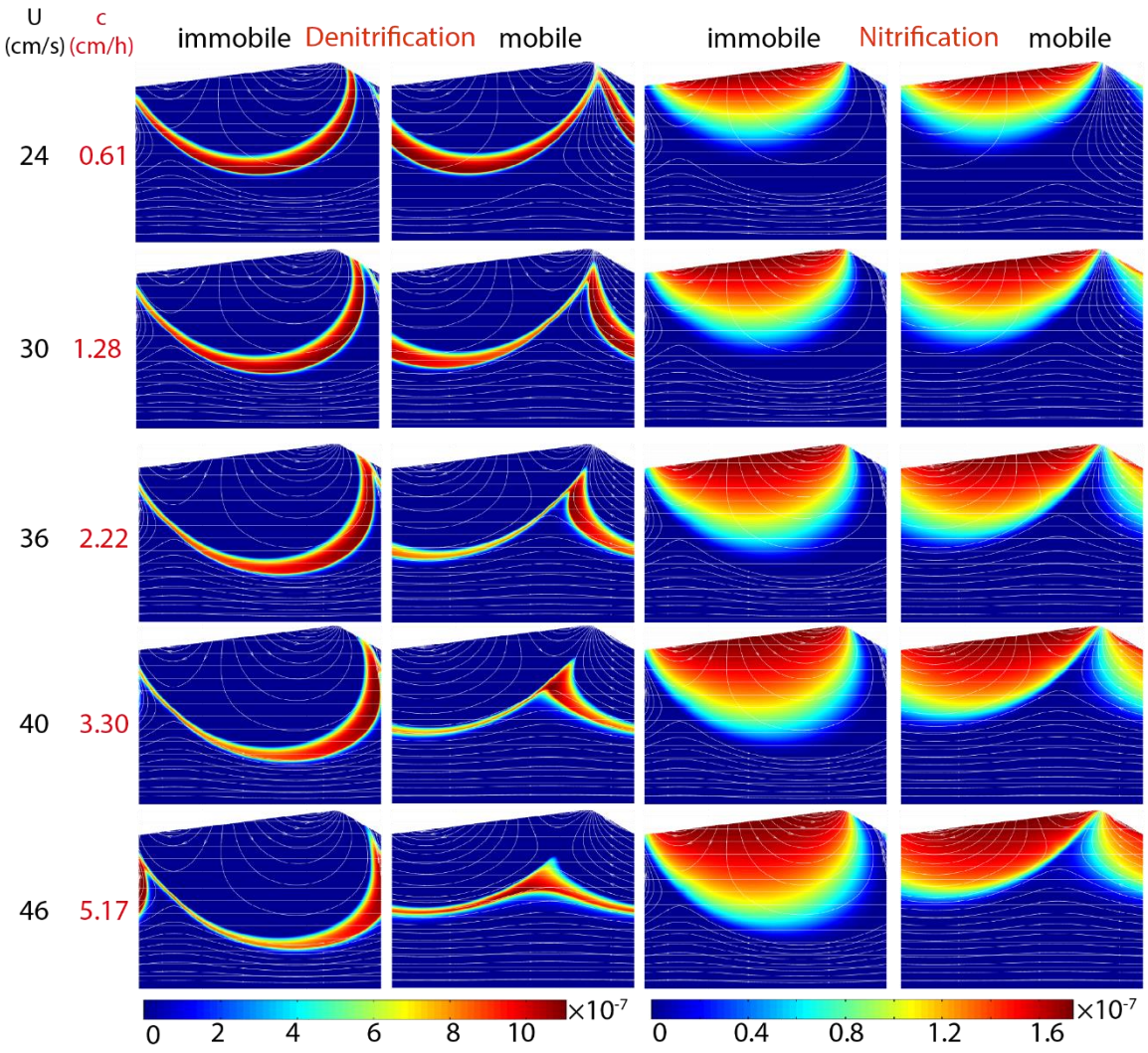

Figure 4.5: Comparison of nitrication and denitrication rates of immobile and mobile bedform for geometry 6 with increasing stream velocity U and corresponding bedform celerity c. Bedform wavelength L=157.57mm, bedform height H=16.22mm. White lines with arrows indicate streamlines. Channel flow is from left to right.

The denitrification zone was relatively shallower for the mobile case than that of the immobile case. Moreover, there were trivial changes in the denitrification zone size for the immobile bedform with increasing stream velocity. On the other hand, the size of the denitrification zone became smaller with increasing stream velocity for the mobile bedform.

We integrated nitrification rates and denitrification rates over the HZ domain (Appendix A3, Table A3.2) to assess the functionality of the entire HZ with respect to nitrate. Take geometry 6 (D_{50}=0.3mm) for example, and as expected, nitrification rates over the HZ (overall nitrification) increased with increasing stream velocity for both immobile and mobile cases. This also held for other geometries.

Each ripple geometry did not follow exactly the same trajectory in terms of dependence of denitrification with increasing stream velocity (Appendix A3, Table A3.2). For the immobile bedform, the overall denitrification always increased with increasing stream velocity for ripples with $D_{50} < 0.3$ mm; for the ripple geometry with $D_{50} = 0.3$ mm, overall denitrification increased first and then became smaller; for the ripple geometry with $D_{50} = 0.4$ mm, it always declined with increasing stream velocity. For the mobile cases, the overall denitrification increased first and then decreased with increasing stream velocity and c for the ripple geometry cases with $D_{50} < 0.08$ mm; it increased monotonically for geometry case $D_{50} = 0.08$ mm; and it decreased first and then increased; for geometry case $D_{50} = 0.4$ mm, it increased in a monotonic way with increasing stream velocity.

We further estimated the ratio of overall nitrification and denitrification for both mobile and immobile cases. It turned out that the ratio was over 1 for geometry case D_{50} < 0.08 mm. But for geometry case D_{50} > 0.08 mm (except for D_{50} = 0.4mm), the ratio was less than 1, and this ratio became smaller with increasing stream velocity.

4.5 DISCUSION

4.5.1 Resolving compounding effects caused by "turnover" on nitrate dynamics in the HZ

The fundamental mechanisms of pumping and turnover have been extensively studied in last two decades [*Elliott and Brooks*, 1997a; b]. Generally, the relative importance of pumping and turnover regulates the hyporheic flux for mobile and immobile bedforms, and thus should also dictate the biogeochemical reactions. In our study using realistic bedforms, we found that turnover becomes dominant over pumping if the sediment grain size is finer, such that the hyporheic flux would become larger as the bedform starts migrating. With grain size D_{50} > 0.1 mm, hyporheic flux for immobile bedform is slightly larger (about 10%) than mobile bedform.

Biogeochemical and ecological transformations in HZs depend on the timescale of hyporheic exchange [*Cardenas et al.*, 2008]. However, the pumping and turnover effects on nitrate dynamics are more complicated than looking solely at pure exchange flux and subsequent supply rate would suggest. This is because the nitrification occurs in the shallow HZ where NH_4^+ is oxidized by DO to NO_3^-, adding additional NO_3^- for denitrification, whereas the denitrification occurs in the deeper HZ where DO is depleted,

and where all available NO_3^- including that produced from shallower nitrification is reduced to dinitrogen gas N_2. As a result, the exchange flux imposes a direct influence on nitrification but less so on denitrification, and thus denitrification responded differently to increasing mean flow velocity as discussed in the section 3.4.

To better assess the nitrate dynamics in the HZ, we resorted to residence time analysis since it is potentially residence time rather than exchange flux that determines the potential for reactions. However, the exchange flux may affect the effective flowing region in the HZ. Many studies have established that residence time is a useful metric and predictor for the potential biogeochemical function of the HZ from pore to continental scales [*Briggs et al.*, 2014; *Gomez et al.*, 2012; *Gomez et al.*, 2015; *Zarnetske et al.*, 2011] as it controls the extent of biogeochemical transformation efficiency within the HZ [*Haggerty et al.*, 2002]. Mean residence time can be a dominant factor controlling the distribution and the amount of NO_3^- in the HZ [*Briggs et al.*, 2014].

In light of above-mentioned arguments, we estimated mean residence time for each case with varying geometries or mean stream velocity (Appendix A3, Table A3.1). Furthermore, we used mean residence time to calculate the *Da* while assuming a constant k_{DOC} in (Equation 4.24). In this case, mean residence times are interchangeable with *Da*.

4.5.2 Stream velocity and mean grain size controlling residence time

There are numerous factors affecting the residence time of HZs, such as bedform asymmetry [*Cardenas et al.*, 2008], hydraulic conductivity, valley slope, and sinuosity [*Gomez et al.*, 2012], heterogeneity [*Sawyer and Cardenas*, 2009], and alluvial

geomorphic features [*Briggs et al.*, 2014]. In this study, we considered the effect of stream velocity and D_{50} since they essentially control the other factors, including hydraulic conductivity, and bedform shapes.

D_{50} plays a dominant role compared to stream velocity in controlling the mean residence time for both mobile and immobile bedforms (Figure 4.6). This is expected from Darcy's law. That is, pore velocity in the sediment is determined by the hydraulic conductivity and pressure gradient. Stream velocity dictates the interface pressure gradient along SWI. The change of stream velocity and pressure gradient (slope) can be considered as a linear relationship. Here, we assumed a constant and uniform temperature in the HZ, so the hydraulic conductivity is regulated by the intrinsic property (permeability) of the sediment rather than by fluid properties. Moreover, according to the empirical equation $permeability = 7.35\times10^{-6} \times D_{50}^2$ (m^2) [*Gangi*, 1985] , permeability is in a quadratic relation with D_{50}, while stream velocity is linearly proportional to pressure gradient following Darcy's law. The mean grain size, which also dictates ripple geometry, plays a leading role in regulating the pore velocity and subsequent mean residence time (Figure 4.6).

4.5.3 Damköhler number determines nitrate removal efficiency

For both mobile and immobile cases, the nitrate removal efficiency is dependent on *Da* (DOC) (Figure 4.7f). This is fundamentally attributed to the competing time scales, including reaction time and residence time induced by the geochemical reaction and solute transport process, respectively, and the supply rate that is also associated with

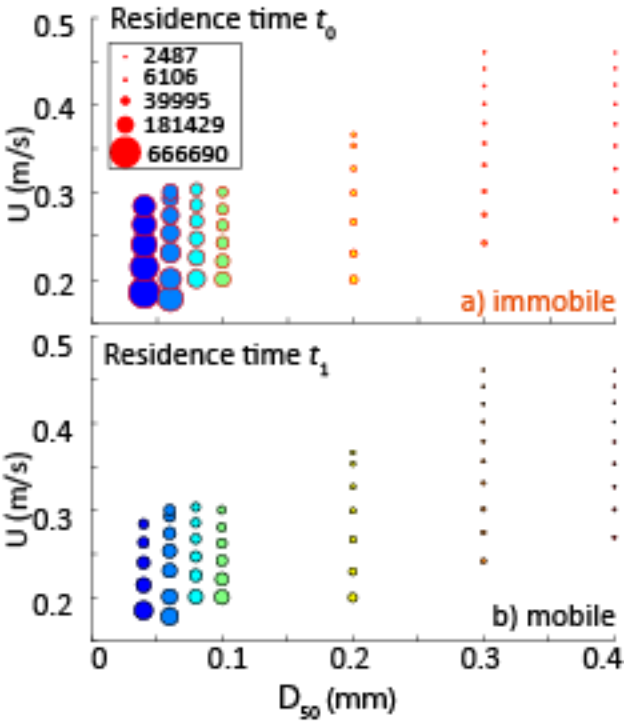

Figure 4.6: Factors controlling the mean residence time in the HZ. The size of the circle represent the relative length of the mean residence time. (a) immobile bedform, and (b) mobile bedform.

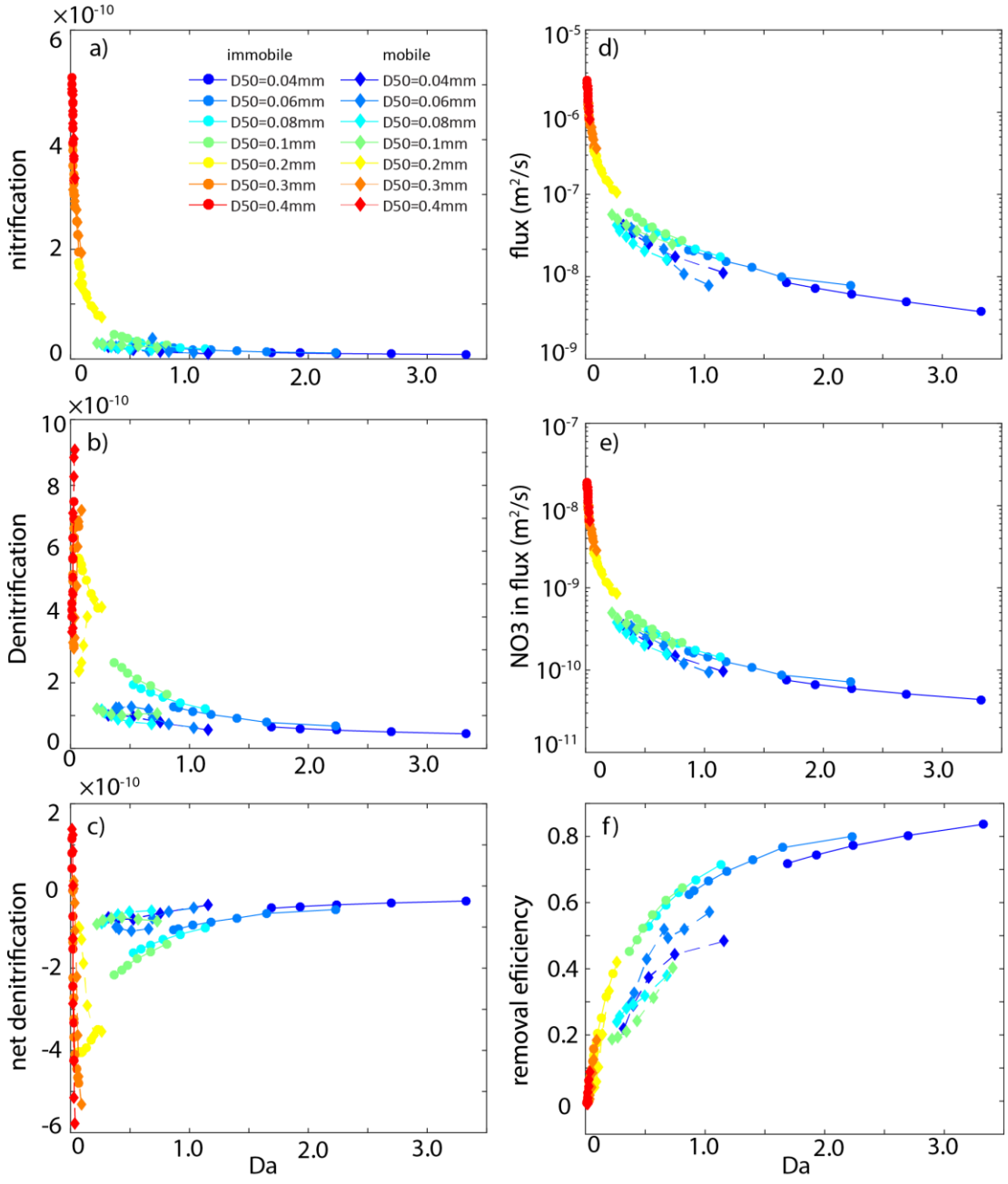

Figure 4.7: Flux and chemical reactions as a function of Damkholer number for both mobile and immobile bedforms: (a) Nitrification, (b) Denitrification, (c) Net denitrification, (d) Flux, (e) NO3 influx, (f) Nitrate removal efficiency. Color represnets the magnitude of mean grain size (D_{50}).

residence time. In any case, the *Da* encompasses all these factors and thus can be used as a proxy to assess the nitrate removal efficiency.

Traditionally, *Da*>1 signifies that residence time is greater than reaction time. Under these conditions, consequently, DOC can be exhausted leading to the cessation of denitrification. This may result in a constant denitrification rate when *Da*>1. On the other hand, *Da*<1 indicates the chemical reactions associated with DOC is insufficient due to the short of residence time that DOC spends within the HZ as the transport process occurs relatively quickly. This would cause a positive relationship between *Da* and denitrification rate. The hidden assumption of the above-mentioned traditional view is based on a fact that the chemical reaction time ($1/k_{DOC}$) controls the denitrification rate if there is a constant supply rate of reactants.

However, the decreasing interfacial flux over two-orders of magnitude leads to a large reduction of supply rate of reactants with *Da* (Figures 4.7d and 4.7e) when *Da*<1. Therefore, unlike the conventional view as *Da*<1, our numerical experiments showed that both nitrification and denitrification were overall negatively related to the *Da* (Figures 4.7a and 4.7b). That is, and consistent with the reduction of supply rate of reactants (Figure 4.7e), geochemical reactions rates decline sharply with *Da* when Da<~0.25, and then approaches a constant as *Da* increases but still <1. Moreover, and as expected when *Da*>1 according to the conventional view, both nitrification and denitrification rates are fairly constant. Again, this is essentially due to the supply rate barely changing when *Da*>1 compared to the reduction when *Da*<1, thus the conventional view that assumes constant supply rates hold for these cases.

The net denitrification rate over the HZ was estimated by integrating the coupled nitrification-denitrification process on the mass change rate of nitrate (Equation 2.14). Negative values represent a nitrite sink since the HZ is consuming nitrate; whereas positive value means the HZ is a nitrate source. In this study, we found that the HZ mostly served as a nitrate sink (Figure 4.7c) as net denitrification<0, except for the most permeable cases when D_{50} >=0.3 mm. This is because the most permeable sediment leads to insufficient residence time while providing ample reactants. The HZ quickly transitioned from a nitrate source to sink with increasing *Da* for several cases. Overall, the magnitude of net denitrification increased with *Da* for the large permeable HZ (*Da*<0.25), and decreased with *Da* for the low permeable HZ (*Da*>0.25), and eventually converged to a constant (Figure 4.7c). The net denitrification and influent nitrate flux (Figure 4.7e) were further used to compute the HZ's removal efficiency (Figure 4.7f) based on equation (2.16).

Unlike net nitrification, the removal efficiency in the HZ increased asymptotically with *Da* for all studied cases. The removal efficiency increased sharply at low *Da*, levels off, and approaches an asymptote with increasing *Da* (Figure 4.7f). This is due to the behavior expected from equation (2.16): (a) The numerator (net denitrification) increases with *Da*, whereas the denominator (effluent nitrite flux) decreases when *Da*<0.25. (b) Both the numerator (net denitrification) and denominator (effluent nitrite flux) decreased with *Da* when *Da*<1, but the degree of reduction in the numerator was much smaller than that of reduction in the denominator. Consequently, we observed a consistent elevated removal efficiency as *Da* increases. (c) Both net denitrification and effluent nitrite flux

approach a constant when $Da>1$, which led to a fairly constant, although slightly increasing, removal efficiency at a large *Da* regime.

4.5.4. Turnover effect on nitrate removal efficiency

Given the same *Da*, the nitrate removal efficiency for the immobile bedform is always greater than that for the mobile bedform across a broad range of *Da*. The hyporhiec zone removed a larger proportion of nitrate for the immobile bedform than that of mobile bedform, and thus greatly reduced the amount of nitrate returning back to the stream water. This can be attributed to the character of the flow cells as discussed above; that is, the immobile ripples had two flow cells while the mobile ripples had three. The difference in flow cells in the mobile bedforms could lead to more mixing and spreading of DO, which would (and does) suppress the denitrification process.

This study for the first time showed that the actual nitrate removal efficiency can be overestimated if bedforms are assumed to never migrate, contrary to reality in nature. Moreover, the complex connection between nitrate removal efficiency and the dimensionless *Da* can be extended to study the realistic nitrogen dynamics in river systems across different scales.

4.6. SUMMARY AND CONCLUSIONS

We studied the effect of bedform mobility on nitrate removal efficiency of the HZ by conducting and comparing simulations with and without bedform migration. We built realistic ripple geometry based on the bedform stability diagram and constrained its flow velocity by the criterion of ripple formation. Seven ripple geometries with different sediment grain sizes and flow velocities and migration rates were studied through

multiphysics numerical simulations. The results showed that the turnover effect due to bedform migration changed the flow field, hyporheic flux, solute distribution, and biogeochemical reactions in the HZ. We found that the nitrate removal efficiency increased with Damköhler number following an asymptotic curve for both mobile and immobile bedforms. Assuming immobile bedforms lead to an overestimation of nitrate removal efficiency, especially for cases with fine sediments when turnover hyporheic exchange is dominant over pumping effect. The relationship between nitrate removal efficiency and Damköhler number established here can be extrapolated to predict nitrate remove efficiency at larger integrated scales.

Chapter 5: Summary

Streams and rivers are not only conduits to the sea. Streams and their underlying aquifers are closely connected through hyporheic zones (HZs). Hyporheic flow can be driven by "pumping" induced by the pressure gradient at the water-sediment interface, and by "turnover" as bedforms migrate [*Elliott and Brooks*, 1997]. Hyporheic exchange drives stream water into and out of the HZ carrying solute and heat, and thus strongly affects solute and thermal distributions in HZs. These make HZs hotspots for N transformations, regulating the downstream nitrogen export in fluvial systems.

This dissertation used numerical simulations to investigate how temperature and bedform dynamics affect nitrogen dynamics in the hyporheic zones. Stream water temperature varies daily and seasonally in nature, which results in complex and dynamic hyporheic thermal distributions. In addition, most biogeochemical reactions are temperature dependent. Thus I conducted a series of simulations to couple and integrate fluid flow, heat transport, and reactive solute transport to understand and quantify the effect of temperature on nitrogen dynamics in HZs.

I found that the function of HZ as a nitrate sink or source is primarily controlled by the $[NO_3^-]/[NH_4^+]$ of stream water. Temperature influenced its nitrate removal or production efficiency. Nitrate removal efficiency of the HZ fluctuates in response to the oscillation of stream water temperature, but the daily average nitrate removal efficiency with dynamic stream temperature was fairly identical to those with steady temperature for denitrification-dominant systems. Future research should further explore the relationship

between temperature and in stream nitrate variation across different temporal and spatial scales.

Not only temperature influences nitrogen dynamics in HZs, bedform migration greatly controls the nitrate removal efficiency in HZs. I found that "turnover" effect due to bedform migration exerted a crucial impact on hyporheic exchange flux, supply rates and chemical reactions in HZs. The nitrate removal efficiency increased asymptotically with Damköhler number for both mobile and immobile bedforms. The mobile bedform led to less nitrate removal efficiency than immobile bedform. Future research should build synthetic but realistic three-dimensional complex bedforms, such as considering the superimposition of small ripples or dunes upon larger dunes, to investigate how their migration affect nitrogen dynamics in HZs. In addition, future study should consider the effect of bedform migration on heat transport in HZs, and synthesize both temperature and bedform dynamics effect on nitrogen dynamics in HZs.

Hyporheic zone has been identified as critically important in river water quality and aquatic ecosystems. The overall objective of my study is to improve understanding the role of the HZ in stream nitrogen cycling. Stream temperature varies daily and seasonally, it results in complex and dynamic hyporheic thermal pattern. Variable stream temperature not only affects the hyporheic flux, but also affects biogeochemical reaction rates in the HZ. This study emphasizes the potential importance of hot spot and hot moments of biogeochemical processes (i.e. denitrification). It helps predict temperature effect on nitrogen cycling in fluvial systems. This has important implications for field observation studies. For example, field measurements in the morning and afternoon

represents different temperature conditions; measurements in different depths of the HZ represents different redox status. As to the study of bedform dynamics effect on nitrogen cycling in HZs, it underlies the importance of sediment transport on the nitrogen cycling in stream ecosystem. Bedform height and the steepness should be considered in future studies.

Appendices

Appendix A1: Reaction rate calculation

Here, I show how I calculate reaction rate of four species we considered in this study in detail. The biodegradation of DOC is considered as a primary reaction, it limits the overall level of microorganism activity (Hunter et al., 1998). For simplicity, first-order degradation kinetics are assumed,

$$r_{\mathrm{DOC}} = k_{\mathrm{DOC}} \cdot C_{DOC} \qquad (A1.1)$$

Where r_{DOC} represents the rate of DOC degradation, k_{DOC} is the first-order reaction rate constant, C_{DOC} is the concentration of DOC. The electrons produced by DOC degradation are transferred first to O_2 (aerobic respiration), and then NO_3^- (denitrification) when O_2 concentration less than the limiting value $C_{O2,lim}$. The fraction of electrons consumed by O_2 (f_{O2}) and NO_3^- ($f_{\mathrm{NO_3^-}}$) are calculated using a modified Monod formulation (Equation 2.5) (Hunter et al., 1998). For each electron acceptor, this formulation assumes that there exists a limiting concentration. When the electron acceptor concentration exceeds its limiting concentration, the rate of its reduction half-reaction is independent of the electron acceptor. If less than its limiting concentration, the rate exhibits a first-order dependence on electron acceptor concentration. I used a coefficient α (Equation 2.6) to characterize this assumption. Based on the preferential order of utilization of the electron acceptor and equation 2.4, reaction rate of O_2 and NO_3^- can be calculated as follows:

$$r_{O2} = \beta_1 \cdot r_{DOC} \cdot f_{O2} = \ r_{DOC} \ \cdot \ \alpha_{O2} = r_{DOC} \ \cdot \begin{cases} \dfrac{C_{O2}}{C_{O2,lim}} & if\ C_{O2} < C_{O2,lim} \\ 1 & if\ C_{O2} \geq C_{O2,lim} \end{cases} \quad \text{(A1. 2)}$$

$$r_{\mathrm{NO_3^-}} = \beta_2 \cdot r_{DOC} \cdot f_{\mathrm{NO_3^-}} = 0.8 \cdot r_{DOC} \cdot (1 - f_{O2}) \cdot \alpha_{\mathrm{NO_3^-}}$$

$$= 0.8 \cdot r_{DOC} \cdot (1 - \alpha_{O2}) \cdot \begin{cases} \dfrac{C_{\mathrm{NO_3^-}}}{C_{\mathrm{NO_3^-},lim}} & if\ C_{\mathrm{NO_3^-}} < C_{\mathrm{NO_3^-},lim} \\ 1 & if\ C_{\mathrm{NO_3^-}} \geq C_{\mathrm{NO_3^-},lim} \end{cases} \quad (A1.3)$$

There are three different situations according to the concentration of O_2 and NO_3^- :

(1) $C_{O2} \geq C_{O2,lim} = 1mg/l$, no denitrification

$$r_{O2} = \beta_1 \cdot r_{DOC} \cdot f_{O2} = \ r_{DOC} \quad \text{(A1. 4)}$$

(2) $C_{O2} < C_{O2,lim},\ C_{\mathrm{NO_3^-}} \geq C_{\mathrm{NO_3^-},lim}$

$$r_{O2} = \beta_1 \cdot r_{DOC} \cdot f_{O2} = \ r_{DOC} \cdot \frac{C_{O2}}{C_{O2,lim}} \quad \text{(A1. 5)}$$

$$r_{\mathrm{NO_3^-}} = \beta_2 \cdot r_{DOC} \cdot f_{\mathrm{NO_3^-}} = 0.8 \cdot r_{DOC} \cdot (1 - \alpha_{O2}) \cdot \alpha_{\mathrm{NO_3^-}}$$

$$=0.8 \cdot r_{DOC} \cdot \left(1 - \frac{C_{O2}}{C_{O2,lim}}\right) \quad \text{(A1.6)}$$

(3) $C_{O2} < C_{O2,lim},\ C_{\mathrm{NO_3^-}} < C_{\mathrm{NO_3^-},lim}$

$$r_{O2} = \beta_1 \cdot r_{DOC} \cdot f_{O2} = \ r_{DOC} \cdot \frac{C_{O2}}{C_{O2,lim}} \quad \text{(A1.7)}$$

$$r_{\mathrm{NO_3^-}} = \beta_2 \cdot r_{DOC} \cdot f_{\mathrm{NO_3^-}} = 0.8 \cdot r_{DOC} \cdot (1 - \alpha_{O2}) \cdot \alpha_{\mathrm{NO_3^-}}$$

$$= 0.8 \cdot r_{DOC} \cdot \left(1 - \frac{C_{O2}}{C_{O2,lim}}\right) \cdot \left(1 - \frac{C_{\mathrm{NO_3^-}}}{C_{\mathrm{NO_3^-},lim}}\right) \quad \text{(A1.8)}$$

Nitrification is described by conventional second-order bimolecular reaction kinetics:

$$r_{\mathrm{NH_4^+}} = k_{\mathrm{NH_4^+}} \cdot C_{\mathrm{NH_4^+}} \cdot C_{\mathrm{O_2}} \quad \text{(A1. 9)}$$

where $k_{\mathrm{NH_4^+}}$ is the second-order nitrification molar rate coefficient, $C_{\mathrm{NH_4^+}}$ and $C_{\mathrm{O_2}}$ are the molar concentrations of ammonium and oxygen, respectively.

Some species act as both reactants and products. The net reaction rates of these four species can be calculated as follows:

$$R_{\mathrm{DOC}} = -r_{DOC} \qquad (A1.10)$$

$$R_{\mathrm{O_2}} = -r_{\mathrm{O_2}} - 2r_{\mathrm{NH_4^+}} \qquad (A1.11)$$

$$R_{\mathrm{NO_3^-}} = -r_{\mathrm{NO_3^-}} + r_{\mathrm{NH_4^+}} \qquad (A1.12)$$

$$R_{\mathrm{NH_4^+}} = -r_{\mathrm{NH_4^+}} \qquad (A1.13)$$

Appendix A2: Temperature effect on stream DO concentration

The effect of temperature variations on stream DO concentrations is obvious. From 5 °C to 35 °C, stream DO concentration decreases from 13mg/L to 7.6 mg/L (Table A2.1). In my dissertation, I assumed that stream DO concentration keep constant. Compared the results of variable stream DO scenario (table A2.1) with the results of constant stream DO scenario (Table A2.2), the difference in nitrification rates between these two scenarios with the same corresponding temperature can be about 30%; However, the difference in denitrification rates can be only 3%. It makes sense, since nitrification needs oxygen to occur while denitrification occurs only when oxygen concentration depletes. My stream cases are denitrification dominant, nitrate removal efficiency (N_{RE}) would not change too much if I did not consider the effect of temperature on stream DO concentration. The difference in nitrate removal efficiency (N_{RE}) between these two scenarios can be only 2% (Table A2.1 and A2.2). Thus, for denitrification dominant system, the effect of temperature on stream DO concentration can be ignored when calculating nitrate removal efficiency. While, for nitrification dominant system, we cannot ignore the temperature effect on steam DO concentration.

Table A2.1 Results for polluted stream case with variable stream DO concentration

Temp (°C)	DO (mg/L)	$\mathbf{r}_{NI}$ mg/(m·s)	$\mathbf{r}_{DN}$ mg/(m·s)	$\mathbf{r}_{netDN}$ mg/(m·s)	HZ flux (m^2/s)	$[NO_3]_{in}$ mg/(m·s)	N_{RE}
5	13	9.61×10^{-5}	2.79×10^{-3}	-2.69×10^{-3}	9.39×10^{-7}	-7.63×10^{-3}	35.3%
10	11	1.82×10^{-4}	3.90×10^{-3}	-3.72×10^{-3}	1.09×10^{-6}	-8.88×10^{-3}	41.9%
15	10	3.66×10^{-4}	5.13×10^{-3}	-4.77×10^{-3}	1.26×10^{-6}	-1.02×10^{-2}	46.7%
20	9	6.73×10^{-4}	6.57×10^{-3}	-5.90×10^{-3}	1.43×10^{-6}	-1.16×10^{-2}	51.0%
25	8.3	1.20×10^{-3}	8.19×10^{-3}	-6.99×10^{-3}	1.61×10^{-6}	-1.29×10^{-2}	54.1%
30	7.6	2.02×10^{-3}	9.95×10^{-3}	-7.93×10^{-3}	1.79×10^{-6}	-1.41×10^{-2}	56.1%

Table A2.2 Results for polluted stream case with constant stream DO concentration

Temp (°C)	DO (mg/L)	$\mathbf{r}_{NI}$ mg/(m·s)	$\mathbf{r}_{DN}$ mg/(m·s)	$\mathbf{r}_{netDN}$ mg/(m·s)	HZ flux (m^2/s)	$[NO_3]_{in}$ mg/(m·s)	N_{RE}
5	10	6.00×10^{-5}	3.03×10^{-3}	-2.97×10^{-3}	9.39×10^{-4}	-7.63×10^{-3}	38.7%
10	10	1.54×10^{-4}	3.98×10^{-3}	-3.82×10^{-3}	1.09×10^{-3}	-8.88×10^{-3}	43.0%
15	10	3.66×10^{-4}	5.13×10^{-3}	-4.77×10^{-3}	1.26×10^{-3}	-1.02×10^{-2}	46.7%
20	10	7.96×10^{-4}	6.55×10^{-3}	-5.76×10^{-3}	1.43×10^{-3}	-1.16×10^{-2}	49.9%
25	10	1.57×10^{-3}	8.28×10^{-3}	-6.71×10^{-3}	1.61×10^{-3}	-1.29×10^{-2}	52.2%
30	10	2.84×10^{-3}	1.03×10^{-2}	-7.45×10^{-3}	1.79×10^{-3}	-1.40×10^{-2}	53.4%

Appendix A3. Parameters for bedform geometry and results for simulations

Seven ripple geometries (50 cases) were chosen for study based on bedform stability diagram (Figure 4.1). Ripple wavelength (L) and height (Δ) are calculated based on empirical equations (Equation 4.6 and 4.7). I assume the lee side angle as 30° to build bedform geometry, α is the stoss angle, L/Δ is the aspect ratio of wavelength to height. Permeability (k) is calculated based on empirical equation (Gangi, 1985). U is the stream velocity, c is the bedform migration rate. Froude number (Fr), bedform threshold predictor (Ft), dimensionless particle parameter (D*), and transport stage parameter (T) are four parameters for characterizing the criterion of ripple formation (Table A3.1). Simulations results of these 50 cases are shown in table A3.2, including the comparison between mobile case and immobile case.

Table A3.1 Parameters for bedform geometry in our study (50 cases)

geometry	D_{50} (mm)	L (mm)	Δ (mm)	Lc (mm)	α	L/Δ	k (m^2) $\times 10^{-12}$	U (cm/s)	Stream slope	c (cm/h)	Fr	Ft	D^*	T (0-3)
1	0.04	91.60	13.25	68.65	10.92	6.91	1.16	18.52	0.0011	0.30	0.19	0.39	1.02	0.37
								21.43	0.0014	0.47	0.21	0.39	1.02	0.86
								23.99	0.0017	0.68	0.24	0.39	1.02	1.57
								26.31	0.0020	0.90	0.26	0.39	1.02	2.14
								28.44	0.0024	1.15	0.28	0.39	1.02	2.73
2	0.06	104.87	13.85	80.89	9.71	7.57	2.61	17.82	0.0009	0.25	0.18	0.42	1.53	0.05
								20.10	0.0012	0.37	0.20	0.42	1.53	0.38
								23.09	0.0015	0.58	0.23	0.42	1.53	0.91
								25.33	0.0018	0.77	0.25	0.42	1.53	1.38
								27.38	0.0021	0.99	0.27	0.42	1.53	1.92
								29.30	0.0024	1.23	0.29	0.42	1.53	2.53
								30.03	0.0025	1.33	0.30	0.42	1.53	2.78
3	0.08	114.29	14.27	89.58	9.05	8.01	4.64	20.11	0.0011	0.36	0.20	0.44	2.04	0.27
								22.52	0.0014	0.52	0.23	0.44	2.04	0.71
								24.70	0.0017	0.71	0.25	0.44	2.04	1.13
								26.71	0.0020	0.91	0.27	0.44	2.04	1.60
								28.58	0.0022	1.13	0.29	0.44	2.04	2.10
								30.34	0.0025	1.37	0.30	0.44	2.04	2.65
4	0.1	121.60	14.60	96.31	8.62	8.33	7.25	20.04	0.0011	0.35	0.20	0.46	2.55	0.21
								22.11	0.0013	0.49	0.22	0.46	2.55	0.53
								24.25	0.0016	0.66	0.24	0.46	2.55	0.97
								26.22	0.0019	0.86	0.26	0.46	2.55	1.47

geometry	D_{50} (mm)	L (mm)	Δ (mm)	Lc (mm)	α	L/Δ	k (m^2) $\times 10^{-12}$	U (cm/s)	Stream slope	c (cm/h)	Fr	Ft	D^*	T (0-3)
								28.06	0.0021	1.08	0.28	0.46	2.55	2.12
								30.02	0.0024	1.35	0.30	0.46	2.55	2.77
								20.01	0.0011	0.34	0.20	0.52	5.09	0.09
								23.00	0.0014	0.55	0.23	0.52	5.09	0.49
								26.62	0.0018	0.89	0.27	0.52	5.09	1.06
5	0.2	144.30	15.62	117.24	7.59	9.24	29.02	29.96	0.0023	1.32	0.30	0.52	5.09	1.70
								32.70	0.0027	1.74	0.33	0.52	5.09	2.21
								35.35	0.0031	2.23	0.35	0.52	5.09	2.63
								36.61	0.0034	2.49	0.37	0.52	5.09	2.90
								24.18	0.0015	0.61	0.24	0.57	7.64	0.27
								27.48	0.0019	0.94	0.27	0.57	7.64	0.59
								30.14	0.0022	1.28	0.30	0.57	7.64	0.85
								33.11	0.0027	1.74	0.33	0.57	7.64	1.17
								35.60	0.0031	2.22	0.36	0.57	7.64	1.51
6	0.3	157.57	16.22	129.48	7.14	9.71	65.28	37.93	0.0035	2.74	0.38	0.57	7.64	1.84
								40.12	0.0039	3.30	0.40	0.57	7.64	2.18
								42.19	0.0043	3.90	0.42	0.57	7.64	2.52
								44.17	0.0047	4.52	0.44	0.57	7.64	2.75
								46.06	0.0052	5.17	0.46	0.57	7.64	2.96
								26.91	0.0018	0.82	0.27	0.60	10.18	0.17
								30.07	0.0022	1.22	0.30	0.60	10.18	0.46
6	0.4	167.00	16.65	138.16	6.87	10.03	116.1	32.69	0.0026	1.62	0.33	0.60	10.18	0.67
								35.34	0.0030	2.10	0.35	0.60	10.18	0.90
								37.82	0.0034	2.65	0.38	0.60	10.18	1.15

geometry	D_{50} (mm)	L (mm)	Δ (mm)	Lc (mm)	α	L/Δ	k (m^2) $\times 10^{-12}$	U (cm/s)	Stream slope	c (cm/h)	Fr	Ft	D^*	T (0-3)
								40.13	0.0039	3.24	0.40	0.60	10.18	1.39
								42.32	0.0043	3.86	0.42	0.60	10.18	1.58
								44.21	0.0047	4.48	0.44	0.60	10.18	1.82
								46.03	0.0051	5.11	0.46	0.60	10.18	1.98

Table A3.2 Hyporheic flux, Reaction rates, mean residence time, and nitrate removal efficiency for immobile bedform and mobile bedform (50 cases). Ratio represents the value of mobile / value of immobile.

D50(mm)	U(m/s)	Nitrate in mg/(m·s)			Nitrification (mg/(m·s)			Denitrification (kg/(m·s)			Removal Efficiency			Mean residence time (s)			Hyporheic flux (m^2/s)		
		immobile	*mobile*	*ratio*	*immobile*	*mobile*	*ratio*	*immobile*	*mobile*	*ratio*	*immobile*	*mobile*	*diff*	*immobile*	*mobile*	ratio	*immobile*	*mobile*	ratio
0.04	0.19	-4.4×10^{-5}	-9.5×10^{-5}	2.19	8.1×10^{-6}	9.5×10^{-6}	1.18	4.5×10^{-5}	5.6×10^{-5}	1.25	0.84	0.48	0.35	666690	231364	0.35	3.7×10^{-9}	1.1×10^{-8}	3.00
0.04	0.21	-5.1×10^{-5}	-1.5×10^{-4}	2.91	8.9×10^{-6}	1.3×10^{-5}	1.44	5.0×10^{-5}	7.9×10^{-5}	1.58	0.80	0.44	0.36	539652	150723	0.28	4.9×10^{-9}	1.8×10^{-8}	3.55
0.04	0.24	-5.9×10^{-5}	-2.1×10^{-4}	3.60	9.7×10^{-6}	1.6×10^{-5}	1.67	5.5×10^{-5}	9.6×10^{-5}	1.74	0.77	0.38	0.40	448506	106800	0.24	6.1×10^{-9}	2.5×10^{-8}	4.09
0.04	0.26	-6.7×10^{-5}	-2.8×10^{-4}	4.18	1.1×10^{-5}	2.0×10^{-5}	1.85	6.1×10^{-5}	1.0×10^{-4}	1.67	0.74	0.29	0.45	385782	80820	0.21	7.3×10^{-9}	3.3×10^{-8}	4.55
0.04	0.28	-7.5×10^{-5}	-3.5×10^{-4}	4.68	1.1×10^{-5}	2.3×10^{-5}	2.00	6.6×10^{-5}	1.0×10^{-4}	1.52	0.72	0.22	0.50	338110	63738	0.19	8.5×10^{-9}	4.2×10^{-8}	4.99
0.06	0.18	-7.2×10^{-5}	-9.3×10^{-5}	1.30	1.1×10^{-5}	1.1×10^{-5}	0.98	6.8×10^{-5}	6.4×10^{-5}	0.94	0.80	0.57	0.23	445455	208559	0.47	7.8×10^{-9}	7.8×10^{-9}	1.00
0.06	0.20	-8.7×10^{-5}	-1.2×10^{-4}	1.37	1.3×10^{-5}	1.2×10^{-5}	0.98	7.9×10^{-5}	7.4×10^{-5}	0.94	0.77	0.52	0.25	329699	165503	0.50	9.9×10^{-9}	1.1×10^{-8}	1.09
0.06	0.23	-1.1×10^{-4}	-1.6×10^{-4}	1.48	1.4×10^{-5}	3.7×10^{-5}	2.60	9.2×10^{-5}	9.2×10^{-5}	1.00	0.73	0.49	0.23	279933	138937	0.50	1.3×10^{-8}	1.6×10^{-8}	1.25
0.06	0.25	-1.3×10^{-4}	-2.0×10^{-4}	1.59	1.6×10^{-5}	1.4×10^{-5}	0.90	1.0×10^{-4}	1.2×10^{-4}	1.14	0.69	0.52	0.18	236647	131794	0.56	1.5×10^{-8}	2.2×10^{-8}	1.43
0.06	0.27	-1.4×10^{-4}	-2.6×10^{-4}	1.78	1.7×10^{-5}	1.8×10^{-5}	1.01	1.1×10^{-4}	1.3×10^{-4}	1.13	0.66	0.43	0.24	206029	102510	0.50	1.8×10^{-8}	2.9×10^{-8}	1.60
0.06	0.29	-1.6×10^{-4}	-3.2×10^{-4}	1.93	1.9×10^{-5}	2.1×10^{-5}	1.11	1.2×10^{-4}	1.2×10^{-4}	1.01	0.64	0.33	0.31	181429	82353	0.45	2.0×10^{-8}	3.6×10^{-8}	1.77
0.06	0.30	-1.7×10^{-4}	-3.4×10^{-4}	1.99	2.0×10^{-5}	2.2×10^{-5}	1.14	1.3×10^{-4}	1.2×10^{-4}	0.98	0.62	0.30	0.33	173471	75774	0.44	2.1×10^{-8}	3.9×10^{-8}	1.84
0.08	0.20	-1.4×10^{-4}	-1.6×10^{-4}	1.10	1.8×10^{-5}	1.6×10^{-5}	0.87	1.2×10^{-4}	7.5×10^{-5}	0.63	0.71	0.38	0.34	225912	136315	0.60	1.8×10^{-8}	1.6×10^{-8}	0.92
0.08	0.23	-1.8×10^{-4}	-2.0×10^{-4}	1.14	2.1×10^{-5}	1.8×10^{-5}	0.84	1.4×10^{-4}	8.1×10^{-5}	0.58	0.67	0.32	0.35	183705	100510	0.55	2.2×10^{-8}	2.1×10^{-8}	0.95
0.08	0.25	-2.1×10^{-4}	-2.4×10^{-4}	1.16	2.4×10^{-5}	2.0×10^{-5}	0.83	1.5×10^{-4}	9.0×10^{-5}	0.58	0.63	0.29	0.34	156202	80183	0.51	2.6×10^{-8}	2.6×10^{-8}	0.98
0.08	0.27	-2.4×10^{-4}	-2.8×10^{-4}	1.18	2.6×10^{-5}	2.2×10^{-5}	0.83	1.7×10^{-4}	1.0×10^{-4}	0.60	0.59	0.28	0.31	134822	67122	0.50	3.0×10^{-8}	3.1×10^{-8}	1.02
0.08	0.29	-2.7×10^{-4}	-3.3×10^{-4}	1.21	2.9×10^{-5}	2.4×10^{-5}	0.84	1.8×10^{-4}	1.1×10^{-4}	0.60	0.56	0.26	0.30	118658	58624	0.49	3.5×10^{-8}	3.7×10^{-8}	1.06
0.08	0.30	-3.1×10^{-4}	-3.8×10^{-4}	1.23	3.1×10^{-5}	2.7×10^{-5}	0.85	1.9×10^{-4}	1.2×10^{-4}	0.60	0.53	0.24	0.29	105817	51983	0.49	3.9×10^{-8}	4.3×10^{-8}	1.09
0.1	0.20	-2.2×10^{-4}	-2.1×10^{-4}	0.97	2.5×10^{-5}	2.1×10^{-5}	0.84	1.7×10^{-4}	1.1×10^{-4}	0.64	0.64	0.40	0.24	162441	145898	0.90	2.8×10^{-8}	2.5×10^{-8}	0.89
0.1	0.22	-2.6×10^{-4}	-2.6×10^{-4}	0.98	2.9×10^{-5}	2.4×10^{-5}	0.81	1.9×10^{-4}	1.0×10^{-4}	0.55	0.61	0.31	0.29	134463	113825	0.85	3.3×10^{-8}	3.0×10^{-8}	0.90
0.1	0.24	-3.2×10^{-4}	-3.1×10^{-4}	1.00	3.3×10^{-5}	2.5×10^{-5}	0.76	2.1×10^{-4}	1.0×10^{-4}	0.48	0.56	0.24	0.32	112324	85487	0.76	4.0×10^{-8}	3.6×10^{-8}	0.91
0.1	0.26	-3.7×10^{-4}	-3.7×10^{-4}	1.01	3.7×10^{-5}	2.6×10^{-5}	0.72	2.3×10^{-4}	1.0×10^{-4}	0.46	0.52	0.21	0.31	96912	67252	0.69	4.6×10^{-8}	4.3×10^{-8}	0.92
0.1	0.28	-4.2×10^{-4}	-4.3×10^{-4}	1.02	4.1×10^{-5}	2.8×10^{-5}	0.69	2.5×10^{-4}	1.1×10^{-4}	0.45	0.49	0.19	0.29	85106	53872	0.63	5.3×10^{-8}	4.9×10^{-8}	0.93
0.1	0.30	-4.8×10^{-4}	-5.0×10^{-4}	1.04	4.5×10^{-5}	3.0×10^{-5}	0.66	2.6×10^{-4}	1.2×10^{-4}	0.47	0.45	0.19	0.27	74645	44240	0.59	6.0×10^{-8}	5.7×10^{-8}	0.95
0.2	0.20	-9.1×10^{-4}	-8.4×10^{-4}	0.93	7.9×10^{-5}	7.6×10^{-5}	0.96	4.3×10^{-4}	4.3×10^{-4}	1.00	0.38	0.42	-0.04	45264	51638	1.14	1.1×10^{-7}	1.1×10^{-7}	0.93
0.2	0.23	-1.2×10^{-3}	-1.1×10^{-3}	0.92	9.6×10^{-5}	9.2×10^{-5}	0.95	4.7×10^{-4}	4.5×10^{-4}	0.96	0.32	0.33	-0.02	34727	39187	1.13	1.5×10^{-7}	1.4×10^{-7}	0.93
0.2	0.27	-1.6×10^{-3}	-1.4×10^{-3}	0.92	1.2×10^{-4}	1.1×10^{-4}	0.94	5.1×10^{-4}	4.0×10^{-4}	0.79	0.25	0.20	0.05	26111	28852	1.10	2.0×10^{-7}	1.8×10^{-7}	0.92
0.2	0.30	-2.0×10^{-3}	-1.8×10^{-3}	0.92	1.4×10^{-4}	1.2×10^{-4}	0.91	5.4×10^{-4}	3.1×10^{-4}	0.58	0.20	0.10	0.10	20723	22258	1.07	2.5×10^{-7}	2.3×10^{-7}	0.91
0.2	0.33	-2.3×10^{-3}	-2.1×10^{-3}	0.92	1.5×10^{-4}	1.3×10^{-4}	0.86	5.6×10^{-4}	2.6×10^{-4}	0.47	0.17	0.06	0.11	17569	18169	1.03	2.9×10^{-7}	2.7×10^{-7}	0.91
0.2	0.35	-2.7×10^{-3}	-2.5×10^{-3}	0.92	1.7×10^{-4}	1.4×10^{-4}	0.81	5.7×10^{-4}	2.4×10^{-4}	0.42	0.15	0.04	0.11	15071	15196	1.01	3.4×10^{-7}	3.1×10^{-7}	0.91
0.2	0.37	-2.9×10^{-3}	-2.7×10^{-3}	0.92	1.8×10^{-4}	1.4×10^{-4}	0.78	5.8×10^{-4}	2.4×10^{-4}	0.41	0.14	0.04	0.10	14045	14023	1.00	3.6×10^{-7}	$3.\times10^{-7}$	0.91
0.3	0.24	-3.0×10^{-3}	-2.9×10^{-3}	0.94	1.9×10^{-4}	1.9×10^{-4}	0.99	6.8×10^{-4}	7.2×10^{-4}	1.07	0.16	0.19	-0.03	14774	17050	1.15	3.8×10^{-7}	3.6×10^{-7}	0.95
0.3	0.27	-3.9×10^{-3}	-3.6×10^{-3}	0.94	2.3×10^{-4}	2.2×10^{-4}	0.99	6.9×10^{-4}	6.9×10^{-4}	0.99	0.12	0.13	-0.01	11501	13340	1.16	4.9×10^{-7}	4.6×10^{-7}	0.94
0.3	0.30	-4.6×10^{-3}	-4.3×10^{-3}	0.93	2.5×10^{-4}	2.5×10^{-4}	0.99	7.0×10^{-4}	6.1×10^{-4}	0.88	0.10	0.08	0.01	9587	11169	1.16	5.8×10^{-7}	5.4×10^{-7}	0.94
0.3	0.33	-5.6×10^{-3}	-5.2×10^{-3}	0.93	2.8×10^{-4}	2.7×10^{-4}	0.98	6.9×10^{-4}	4.9×10^{-4}	0.72	0.07	0.04	0.03	7984	9320	1.17	7.0×10^{-7}	6.5×10^{-7}	0.93
0.3	0.36	-6.4×10^{-3}	-5.9×10^{-3}	0.92	3.0×10^{-4}	2.9×10^{-4}	0.96	6.7×10^{-4}	4.0×10^{-4}	0.59	0.06	0.02	0.04	6925	8089	1.17	8.0×10^{-7}	7.4×10^{-7}	0.93
0.3	0.38	-7.3×10^{-3}	-6.7×10^{-3}	0.92	3.2×10^{-4}	3.0×10^{-4}	0.93	6.4×10^{-4}	3.4×10^{-4}	0.53	0.04	0.01	0.04	6106	7132	1.17	9.1×10^{-7}	8.4×10^{-7}	0.92
0.3	0.40	-8.1×10^{-3}	-7.4×10^{-3}	0.92	3.4×10^{-4}	3.0×10^{-4}	0.90	6.1×10^{-4}	3.1×10^{-4}	0.51	0.03	0.00	0.03	5458	6350	1.16	1.0×10^{-6}	9.3×10^{-7}	0.92
0.3	0.42	-9.0×10^{-3}	-8.2×10^{-3}	0.92	3.5×10^{-4}	3.1×10^{-4}	0.87	5.8×10^{-4}	3.0×10^{-4}	0.53	0.02	0.00	0.03	4931	5721	1.16	1.1×10^{-6}	1.0×10^{-6}	0.92
0.3	0.44	-1.1×10^{-2}	-1.0×10^{-2}	0.89	3.9×10^{-4}	3.3×10^{-4}	0.84	5.3×10^{-4}	3.2×10^{-4}	0.60	0.01	0.00	0.01	4503	5190	1.15	1.4×10^{-6}	1.3×10^{-6}	0.89
0.3	0.46	-1.1×10^{-2}	-9.8×10^{-3}	0.92	3.8×10^{-4}	3.1×10^{-4}	0.81	5.1×10^{-4}	3.2×10^{-4}	0.63	0.01	0.00	0.01	4135	4741	1.15	1.3×10^{-6}	1.2×10^{-6}	0.92

D50(mm)	U(m/s)	Nitrate in mg/(m·s)			Nitrification (mg/(m·s)			Denitrification (kg/(m·s)			Removal Efficiency			Mean residence time (s)			Hyporheic flux (m^2/s)		
		immobile	*mobile*	*ratio*	*immobile*	*mobile*	*ratio*	*immobile*	*mobile*	*ratio*	*immobile*	*mobile*	*diff*	*immobile*	*mobile*	ratio	*immobile*	*mobile*	ratio
0.4	0.27	-6.8×10^{-3}	-6.5×10^{-3}	0.96	3.3×10^{-4}	3.3×10^{-4}	1.01	7.5×10^{-4}	9.1×10^{-4}	1.21	0.06	0.09	-0.03	6901	7939	1.15	8.5×10^{-7}	8.2×10^{-7}	0.97
0.4	0.30	-8.4×10^{-3}	-8.1×10^{-3}	0.96	3.6×10^{-4}	3.7×10^{-4}	1.02	7.0×10^{-4}	8.9×10^{-4}	1.27	0.04	0.06	-0.02	5549	6448	1.16	1.1×10^{-6}	1.0×10^{-6}	0.96
0.4	0.33	-9.9×10^{-3}	-9.4×10^{-3}	0.95	3.9×10^{-4}	4.0×10^{-4}	1.02	6.4×10^{-4}	8.3×10^{-4}	1.29	0.02	0.05	-0.02	4717	5518	1.17	1.2×10^{-6}	1.2×10^{-6}	0.96
0.4	0.35	-1.1×10^{-2}	-1.1×10^{-2}	0.95	4.2×10^{-4}	4.3×10^{-4}	1.02	5.7×10^{-4}	7.2×10^{-4}	1.25	0.01	0.03	-0.01	4048	4760	1.18	1.4×10^{-6}	1.4×10^{-6}	0.95
0.4	0.38	-1.3×10^{-2}	-1.2×10^{-2}	0.95	4.5×10^{-4}	4.5×10^{-4}	1.02	5.2×10^{-4}	5.8×10^{-4}	1.12	0.01	0.01	0.00	3541	4191	1.18	1.6×10^{-6}	1.6×10^{-6}	0.95
0.4	0.40	-1.5×10^{-2}	-1.4×10^{-2}	0.94	4.7×10^{-4}	4.7×10^{-4}	1.01	4.8×10^{-4}	4.7×10^{-4}	0.98	0.00	0.00	0.00	3269	3741	1.14	1.8×10^{-6}	1.7×10^{-6}	0.94
0.4	0.42	-1.6×10^{-2}	-1.5×10^{-2}	0.94	4.9×10^{-4}	4.8×10^{-4}	0.99	4.4×10^{-4}	4.0×10^{-4}	0.90	0.00	-0.01	0.00	2944	3378	1.15	2.0×10^{-6}	1.9×10^{-6}	0.94
0.4	0.44	-1.8×10^{-2}	-1.7×10^{-2}	0.93	5.0×10^{-4}	4.9×10^{-4}	0.98	4.2×10^{-4}	3.6×10^{-4}	0.87	0.00	-0.01	0.00	2694	3085	1.14	2.2×10^{-6}	2.1×10^{-6}	0.94
0.4	0.46	-1.9×10^{-2}	-1.8×10^{-2}	0.93	5.1×10^{-4}	4.9×10^{-4}	0.96	4.0×10^{-4}	3.5×10^{-4}	0.88	-0.01	-0.01	0.00	2487	2847	1.14	2.4×10^{-6}	2.3×10^{-6}	0.93

Bibliography

Alexander, R. B., R. A. Smith, and G. E. Schwarz (2000), Effect of stream channel size on the delivery of nitrogen to the Gulf of Mexico, *Nature,* 403(6771), 758-761, doi: 10.1038/35001562.

Ahmerkamp, S., C. Winter, F. Janssen, M. M. Kuypers, and M. Holtappels (2015), The impact of bedform migration on benthic oxygen fluxes, *J. Geophys. Res. Biogeosci*., 120(11), 2229-2242. doi:10.1002/2015JG003106.

Alexander, R. B., J. K. Böhlke, E. W. Boyer, M. B. David, J. W. Harvey, P. J. Mulholland, S. P. Seitzinger, C. R. Tobias, C. Tonitto, and W. M. Wollheim (2009), Dynamic modeling of nitrogen losses in river networks unravels the coupled effects of hydrological and biogeochemical processes, *Biogeochemistry*, 93(1-2), 91-116, doi: 10.1007/s10533-008-9274-8

Baas, J. H. (1999), An empirical model for the development and equilibrium morphology of current ripples in fine sand, *Sedimentology*, 46(1), 123-138. doi:10.1046/j.1365-3091.1999.00206.x

Baer, S. E., T. L. Connelly, R. E. Sipler, P. L. Yager, and D. A. Bronk (2014), Effect of temperature on rates of ammonium uptake and nitrification in the western coastal Arctic during winter, spring, and summer, *Global Biogeochem.. Cy.*, 28(12), 2013GB004765, doi: 10.1002/2013GB004765

Bardini, L., F. Boano, M. B. Cardenas, R. Revelli, and L. Ridolfi (2012), Nutrient cycling in bedform induced hyporheic zones, *Geochim. Cosmochim. Acta,* 84(0), 47-61, doi: 10.1016/j.gca.2012.01.025.

Bardini, L., F. Boano, M.B. Cardenas, A. Sawyer, R. Revelli, and L. Ridolfi (2013), Small scale permeability heterogeneity has negligible effects on nutrient cycling in steambeds, *Geophys. Res. Lett*., 40, 1118–1122, doi:10.1002/grl.50224.

Birgand, F., R. W. Skaggs, G. M. Chescheir, and J. W. Gilliam (2007), Nitrogen removal in streams of agricultural catchments—a literature review, *Crit. Rev. Env. Sci. Technol*., 37(5), 381-487. doi: 10.1080/10643380600966426.

Boano, F., A. Demaria, R. Revelli, and L. Ridolfi (2010), Biogeochemical zonation due to intrameander hyporheic flow, *Water Resour. Res.,* 46(2), W02511, doi:10.1029/2008WR007583.

Boano, F., C. Camporeale, R. Revelli, and L. Ridolfi (2006), Sinuosity-driven hyporheic exchange in meandering rivers, *Geophys. Res. Lett.,* 33(18), L18406, doi: 10.1029/2006GL027630

Boano, J. W. Harvey, A. Marion, A. I. Packman, R. Revelli, L. Ridolfi, and A. Wörman (2014), Hyporheic flow and transport processes: Mechanisms, models, and biogeochemical implications, *Rev. Geophys.,* 52, 603–679, doi:10.1002/2012RG000417.

Bottacin-Busolin, A., and A. Marion (2010), Combined role of advective pumping and mechanical dispersion on time scales of bed form–induced hyporheic exchange, *Water Resour*. *Res*., 46(8), W08518, doi:10.1029/2009WR008892.

Boulton, A. J., S. Findlay, P. Marmonier, E. H. Stanley, and H. M. Valett (1998), The functional significance of the hyporheic zone in streams and rivers, *Annu. Rev. Ecol. Syst.,* 29(1), 59-81.

Briggs, M. A., L. K. Lautz, and D. K. Hare (2014), Residence time control on hot moments of net nitrate production and uptake in the hyporheic zone, *Hydrol. Process.,* 28(11), 3741-3751, doi: 10.1002/hyp.9921

Brunke, M., and T. Gonser (1997), The ecological significance of exchange processes between rivers and groundwater, *Freshwater Biol.,* 37(1), 1-33. doi: 10.1046/j.1365-2427.1997.00143.x.

Buffington, J. M., and D. Tonina (2009), Hyporheic exchange in mountain rivers II: effects of channel morphology on mechanics, scales, and rates of exchange, *Geog. Compass,* 3(3), 1038-1062. doi:10.1111/j.1749-8198.2009.00225.x

Burns, D. A., M. P. Miller, B. A. Pellerin, and P. D. Capel (2016), Patterns of diel variation in nitrate concentrations in the Potomac River, *Freshw. Sci.,* 35(4), 1117-1132, doi: 10.1086/688777

Caissie, D. (2006), The thermal regime of rivers: a review, *Freshwater Biol.,* 51(8), 1389-1406, doi:10.1111/j.1365-2427.2006.01597.x

Cardenas, and J. L. Wilson (2007), Dunes, turbulent eddies, and interfacial exchange with permeable sediments, *Water Resour. Res*, 43(8), W08412, doi: 10.1029/2006WR005787

Cardenas, J. L. Wilson, and R. Haggerty (2008), Residence time of bedform-driven hyporheic exchange, *Adv Water Resour*, 31(10), 1382-1386, doi: 10.1016/j.advwatres.2008.07.006.

Cardenas, M. B. (2008), Surface water-groundwater interface geomorphology leads to scaling of residence times, *Geophys. Res. Lett*., 35(8), L08402, doi:10.1029/2008GL033753.

Cardenas, M. B. (2009), Stream-aquifer interactions and hyporheic exchange in gaining and losing sinuous streams, *Water Resour. Res.,* 45(6), W06429, doi: 10.1029/2008WR007651

Cardenas, M. B. (2015), Hyporheic zone hydrologic science: A historical account of its emergence and a prospectus, *Water Resour. Res.,* 51, 3601–3616, doi:10.1002/2015WR017028.

Cardenas, M. B., and J. L. Wilson (2007a), Thermal regime of dune-covered sediments under gaining and losing water bodies, *J. Geophys. Res. Biogeosci*., 112(G4), G04013.doi: 10.1029/2007JG000485

Cardenas, M. B., and J. L. Wilson (2007b), Effects of current-bed form induced fluid flow on the thermal regime of sediments, *Water Resour. Res,* 43(8), W08431, doi: 10.1029/2006WR005343

Cardenas, M.B. (2008), The effect of river bend morphology on flow and timescales of surface water–groundwater exchange across pointbars, *J. Hydrol.,* 362(1–2), 134-141, doi:10.1016/j.jhydrol.2008.08.018.

Cardenas,M.B., and J. L. Wilson (2004), Impact of heterogeneity, bed forms, and stream curvature on subchannel hyporheic exchange. *Water Resour. Res*., 40(8), W08307,doi:10.1029/2004WR003008.

Christensen, P. B., L. P. Nielsen, J. Sørensen, and N. P. Revsbech (1990), Denitrification in nitrate-rich streams: Diurnal and seasonal variation related to benthic oxygen metabolism, *Limnol. Oceanogr.*, 35(3), 640-651, doi:10.4319/lo.1990.35.3.0640

Cirmo, C. P., and J. J. McDonnell (1997), Linking the hydrologic and biogeochemical controls of nitrogen transport in near-stream zones of temperate-forested catchments: a review, *J. Hydrol.,* 199(1), 88-120. doi: 10.1016/S0022-1694(96)03286-6.

Clément, J.-C., G. Pinay, and P. Marmonier (2002), Seasonal dynamics of denitrification along topohydrosequences in three different riparian wetlands, *J. Environ. Qual*., 31(3), 1025-1037. doi:10.2134/jeq2002.1025.

Cohen, M. J., J. B. Heffernan, A. Albertin, and J. B. Martin (2012), Inference of riverine nitrogen processing from longitudinal and diel variation in dual nitrate isotopes, *J. Geophys. Res*. *Biogeosci*., 117(G1), doi:10.1029/2011JG001715.

Craig, L. S., M. A. Palmer, D. C. Richardson, S. Filoso, E. S. Bernhardt, B. P. Bledsoe, M. W. Doyle, P. M. Groffman, B. A. Hassett, and S. S. Kaushal (2008), Stream restoration strategies for reducing river nitrogen loads, *Front. Ecol. Environ.,* 6(10), 529-538. doi:10.1890/070080

Dawson, R., and K. Murphy (1972), The temperature dependency of biological denitrification, *Water Res.,* 6(1), 71-83, doi: 10.1016/0043-1354(72)90174-1

Duff, J. H., and F. J. Triska (1990), Denitrifications in sediments from the hyporheic zone adjacent to a small forested stream, *Can. J. Fish. Aquat.,* 47(6), 1140-1147.

Elliott, A. H., and N. H. Brooks (1997a), Transfer of nonsorbing solutes to a streambed with bed forms: Laboratory experiments, *Water Resour. Res.,* 33(1), 137-151, doi: 10.1029/96wr02783.

Elliott, A. H., and N. H. Brooks (1997b), Transfer of nonsorbing solutes to a streambed with bed forms: Theory, *Water Resour. Res*., 33(1), 123-136, doi: 10.1029/96wr02784.

Endreny, T., L. Lautz, and D. I. Siegel (2011), Hyporheic flow path response to hydraulic jumps at river steps: Flume and hydrodynamic models, *Water Resour. Res*., 47(2), W02517. doi: 10.1029/2009WR008631

Engler, R., and W. Patrick (1974), Nitrate removal from floodwater overlying flooded soils and sediments, *J. Environ. Qual.,* 3(4), 409-413. doi:10.2134/jeq1974.00472425000300040025x.

Fabian, M. W., T. A. Endreny, A. Bottacin-Busolin, and L. K. Lautz (2011), Seasonal variation in cascade-driven hyporheic exchange, northern Honduras, *Hydrol. Process.*, 25(10), 1630-1646, doi: 10.1002/hyp.7924

Findlay, S. (1995), Importance of surface-subsurface exchange in stream ecosystems: the hyporheic zone, *Limnol. Oceanogr.,* 40(1), 159-164. doi: 10.4319/lo.1995.40.1.0159.

Fischer, H., F. Kloep, S. Wilzcek, and M. Pusch (2005), A River's Liver – Microbial Processes within the Hyporheic Zone of a Large Lowland River, *Biogeochemistry*, 76(2), 349-371, doi: 10.1007/s10533-005-6896-y.

Galloway, J. N. (1998), The global nitrogen cycle: changes and consequences, *Environ. Pollut.,* 102(1), 15-24. doi:10.1016/S0269-7491(98)80010-9

Galloway, J. N., F. J. Dentener, D. G. Capone, E. W. Boyer, R. W. Howarth, S. P. Seitzinger, G. P. Asner, C. Cleveland, P. Green, and E. Holland (2004), Nitrogen cycles: past, present, and future, *Biogeochemistry*, 70(2), 153-226. doi:10.1007/s10533-004-0370-0

Galloway, J. N., J. D. Aber, J. W. Erisman, S. P. Seitzinger, R. W. Howarth, E. B. Cowling, and B. J. Cosby (2003), The nitrogen cascade, *Bioscience*, 53(4), 341-356. doi:10.1641/0006-3568.

Gangi, A. F. (1985), Permeability of unconsolidated sands and porous rocks, *J. Geophys. Res*., 90(B4), 3099–3104, doi:10.1029/JB090iB04p03099.

Garcia, M. H. (2008), *Sedimentation Engineering*. ASCE Manual No. 110, American Society of Civil Engineers, ISBN 10 # 0784408149.

Gerecht, K. E., M. B. Cardenas, A. J. Guswa, A. H. Sawyer, J. D. Nowinski, and T. E. Swanson (2011), Dynamics of hyporheic flow and heat transport across a bed-to-bank continuum in a large regulated river, *Water Resour.Res.* 47(3), W03524, doi: 10.1029/2010WR009794

Gomez, J. D., J. L. Wilson, and M. B. Cardenas (2012), Residence time distributions in sinuosity-driven hyporheic zones and their biogeochemical effects, *Water Resour. Res*., 48(9), W09533, doi: 10.1029/2012wr012180.

Gomez, J. D., J. W. Harvey, M. B. Cardenas, and B. Kiel (2015), Denitrification in the Mississippi River network controlled by flow through river bedforms, *Nat. Geosci,* 8, 941–945. doi:10.1038/ngeo2567.

Goode, D. J. (1996), Direct Simulation of Groundwater Age, *Water Resour. Res.,* 32(2), 289-296, doi: 10.1029/95wr03401.

Groffman, P. M., A. M. Dorsey, and P. M. Mayer (2005), N processing within geomorphic structures in urban streams, *J. N. Am. Benthol. Soc*., 24, 613-625. doi: 10.1899/04-026.1.

Gruber, N., and J. N. Galloway (2008), An Earth-system perspective of the global nitrogen cycle, *Nature*, 451(7176), 293-296. doi:10.1038/nature06592

Haggerty, R., S. M. Wondzell, and M. A. Johnson (2002), Power-law residence time distribution in the hyporheic zone of a 2nd-order mountain stream, *Geophys. Res. Lett.,* 29(13), 1640, doi: 10.1029/2002GL014743.

Halliday, S., R. Skeffington, A. Wade, C. Neal, B. Reynolds, D. Norris, and J. Kirchner (2013), Upland streamwater nitrate dynamics across decadal to sub-daily timescales: a case study of Plynlimon, Wales, *Biogeosciences*, 10, 8013-8038, doi: 10.5194/bg-10-8013-2013

Harvey, J. Drummond, R. Martin, L. McPhillips, A. Packman, D. Jerolmack, S. Stonedahl, A. Aubeneau, A. Sawyer, and L. Larsen (2012), Hydrogeomorphology

of the hyporheic zone: Stream solute and fine particle interactions with a dynamic streambed, *J. Geophys*. *Res.,* 117(G4), G00N11, doi:10.1029/2012JG002043.

Harvey, J. K. Böhlke, M. A. Voytek, D. Scott, and C. R. Tobias (2013), Hyporheic zone denitrification: Controls on effective reaction depth and contribution to whole-stream mass balance, *Water Resour. Res.,* 49, 6298–6316, doi:10.1002/wrcr.20492.

Harvey, J. W., and K. E. Bencala (1993), The Effect of streambed topography on surface-subsurface water exchange in mountain catchments, *Water Resour. Res.,* 29(1), 89-98, doi:10.1029/92WR01960.

Harvey, J. W., and M. Gooseff (2015), River corridor science: Hydrologic exchange and ecological consequences from bedforms to basins, *Water Resour. Res*., 51, 6893–6922, doi:10.1002/2015WR017617.

Harvey, J. W., J. K. Böhlke, M. A. Voytek, D. Scott, and C. R. Tobias (2013), Hyporheic zone denitrification: Controls on effective reaction depth and contribution to whole-stream mass balance, *Water Resour. Res.,* 49, 6298–6316, doi:10.1002/wrcr.20492.

Heffernan, J. B., and M. J. Cohen (2010), Direct and indirect coupling of primary production and diel nitrate dynamics in a subtropical spring-fed river, *Limnol. Oceanogr.*, 55(2), 677-688, doi: 10.4319/lo.2010.55.2.0677

Hester, E. T., K. I. Young, and M. A. Widdowson (2014), Controls on mixing-dependent denitrification in hyporheic zones induced by riverbed dunes: A steady state

modeling study, *Water Resour.Res.,* 50(11), 9048-9066, doi: 10.1002/2014WR015424

Hester, E. T., M. W. Doyle, and G. C. Poole (2009), The influence of in-stream structures on summer water temperatures via induced hyporheic exchange, *Limnol. Oceanogr.,* 54(1), 355-367, doi: 10.4319/lo.2009.54.1.0355.

Hill, A. R., C. F. Labadia, and K. Sanmugadas (1998), Hyporheic zone hydrology and nitrogen dynamics in relation to the streambed topography of a N-rich stream, *Biogeochemistry*, 42(3), 285-310. doi: 10.1023/A:1005932528748

Howard-Williams, C., S. Pickmere, and J. Davies (1983), Decay rates and nitrogen dynamics of decomposing watercress, *Hydrobiologia*, 99(3), 207-214. doi:10.1007/BF00008772.

Hunter, K. S., Y. Wang, and P. Van Cappellen (1998), Kinetic modeling of microbially-driven redox chemistry of subsurface environments: coupling transport, microbial metabolism and geochemistry, *J. Hydrol*., 209(1), 53-80. doi:10.1016/S0022-1694(98)00157-7.

Janssen, F., M.B. Cardenas, A. H. Sawyer, T. Dammrich, J. Krietsch, and D. Beer (2012), A comparative experimental and multiphysics computational fluid dynamics study of coupled surface–subsurface flow in bed forms, *Water Resour.Res,* 48(8). W08514. doi: 10.1029/2012WR011982.

Jones Jr, J. B., and R. M. Holmes (1996), Surface-subsurface interactions in stream ecosystems, *Trends Ecol. & Evol.,* 11(6), 239-242. doi:10.1016/0169-5347(96)10013-6.

Jones Jr, J. B., S. G. Fisher, and N. B. Grimm (1995), Nitrification in the hyporheic zone of a desert stream ecosystem, *J. N. Am. Benthol. Soc.* 14, 249-258.doi: 10.2307/1467777.

Karim, F. (1995), Bed configuration and hydraulic resistance in alluvial-channel flows, *J. Hydraul. Eng*. 121(1), 15-25. doi:10.1061/(ASCE)0733-9429

Kasahara, T., and S. M. Wondzell (2003), Geomorphic controls on hyporheic exchange flow in mountain streams, *Water Resour. Res*., 39(1), 1005, doi: 10.1029/2002WR001386

Kaushik, N., and J. Robinson (1976), Preliminary observations on nitrogen transport during summer in a small spring-fed Ontario stream, *Hydrobiologia*, 49(1), 59-63.doi: 10.1007/BF00016169.

Kessler, A. J., M. B. Cardenas, and P. L. Cook (2015), The negligible effect of bed form migration on denitrification in hyporheic zones of permeable sediments, *J. Geophys. Res*. *Biogeosci.,* 120(3), 538-548, doi: 10.1002/2014JG002852

Kessler, A. J., M.B. Cardenas, I. R. Santos, and P. L. M. Cook (2014), Enhancement of denitrification in permeable carbonate sediment due to intra-granular porosity: A multi-scale modelling analysis, *Geochim. Cosmochim. Acta,* 141, 440-453. doi: 10.1016/j.gca.2014.06.028.

Kiel, B. A., and M.B. Cardenas (2014), Lateral hyporheic exchange throughout the Mississippi River network, *Nat. Geosci*, 7(6), 413-417, doi: 10.1038/ngeo2157.

Lautz, L. K., and R. M. Fanelli (2008), Seasonal biogeochemical hotspots in the streambed around restoration structures, *Biogeochemistry*, 91(1), 85-104, doi:10.1007/s10533-008-9235-2

Lautz, L.K., Kranes N.T., and Siegel D.I. (2010), Heat tracing of heterogeneous hyporheic exchange adjacent to in-stream geomorphic features. *Hydrol. Process* 24(21), 3074-3086. doi:10.1002/hyp.7723

Martin, L. A., P. J. Mulholland, J. R. Webster, and H. M. Valett (2001), Denitrification potential in sediments of headwater streams in the southern Appalachian Mountains, USA, *J. N. Am. Benthol. Soc*., 20(4), 505-519. doi: 10.2307/1468084.

Marzadri, A., D. Tonina, and A. Bellin (2012), Morphodynamic controls on redox conditions and on nitrogen dynamics within the hyporheic zone: Application to gravel bed rivers with alternate-bar morphology, *J. Geophys. Res. Biogeosci*., 117(G3), G00N10, doi: 10.1029/2012jg001966.

Marzadri, A., D. Tonina, and A. Bellin (2013), Quantifying the importance of daily stream water temperature fluctuations on the hyporheic thermal regime: Implication for dissolved oxygen dynamics, *J. Hydrol.,* 507, 241-248. doi: 10.1016/j.jhydrol.2013.10.030.

Mazza, R., S. Wondzell, and J. Zarnetske (2014), The stream subsurface: nitrogen cycling and the cleansing function of hyporheic zones. *Science Findings*, 166. Portland

McClain, M. E., E. W. Boyer, C. L. Dent, S. E. Gergel, N. B. Grimm, P. M. Groffman, S. C. Hart, J. W. Harvey, C. A. Johnston, and E. Mayorga (2003), Biogeochemical

hot spots and hot moments at the interface of terrestrial and aquatic ecosystems, *Ecosystems,* 6(4), 301-312. doi: 10.1007/s10021-003-0161-9.

Menichino, G.T., and Hester E.T. (2014), Hydraulic and thermal effects of in-stream structure-induced hyporheic exchange across a range of hydraulic conductivities, *Water Resour.Res*. 50(6), 4643-4661,doi: 10.1002/2013WR014758

Monsen, N. E., J. E. Cloern, L. V. Lucas, and S. G. Monismith (2002), A comment on the use of flushing time, residence time, and age as transport time scales, *Limnol Oceanogr.*, 47(5), 1545-1553, doi: 10.4319/lo.2002.47.5.1545.

Mulholland, P. J., S. A. Thomas, H. M. Valett, J. R. Webster, and J. Beaulieu (2006), Effects of light on NO3-uptake in small forested streams: diurnal and day-to-day variations, *J. N. Am. Benthol. Soc.,* 25(3), 583-595, doi: 10.1899/0887-3593.

Nimick, D. A., C. H. Gammons, T. E. Cleasby, J. P. Madison, D. Skaar, and C. M. Brick (2003), Diel cycles in dissolved metal concentrations in streams: occurrence and possible causes, *Water Resour.Res*., 39(9), 1247, doi:10.1029/2002WR001571

Norman, F. A., and M. B. Cardenas (2014), Heat transport in hyporheic zones due to bedforms: An experimental study, *Water Resour.Res*., 50(4), 3568-3582, doi: 10.1002/2013wr014673.

Paarlberg, A. L. A. J., and C. Winter (2013), Flow separation in the lee of bedforms: a numerical study on the influence of bedform height and length, Coastaldynamics.

Packman, A. I., and M. Salehin (2003), Relative roles of stream flow and sedimentary conditions in controlling hyporheic exchange, *Hydrobiologia*, 494(1), 291-297. doi: 10.1023/A:1025403424063.

Packman, A. I., and N. H. Brooks (2001), Hyporheic exchange of solutes and colloids with moving bed forms, *Water Resour. Res.,* 37(10), 2591–2605, doi:10.1029/2001WR000477.

Pellerin, B. A., B. D. Downing, C. Kendall, R. A. Dahlgren, T. E. Kraus, J. Saraceno, R. G. Spencer, and B. A. Bergamaschi (2009), Assessing the sources and magnitude of diurnal nitrate variability in the San Joaquin River (California) with an in situ optical nitrate sensor and dual nitrate isotopes, *Freshwater Biol.,* 54(2), 376-387, doi:10.1111/j.1365-2427.2008.02111.x

Peterson, B. J., W. M. Wollheim, P. J. Mulholland, J. R. Webster, J. L. Meyer, J. L. Tank, E. Martí, W. B. Bowden, H. M. Valett, and A. E. Hershey (2001), Control of nitrogen export from watersheds by headwater streams, *Science,* 292(5514), 86-90, doi: 10.1126/science.1056874

Precht, E., U. Franke, L. Polerecky, and M. Huettel (2004), Oxygen dynamics in permeable sediments with wave-driven pore water exchange, *Limnol. Oceanogr.*, 49(3), 693-705. doi: 10.4319/lo.2004.49.3.0693.

Roley, S. S., J. L. Tank, and M. A. Williams (2012), Hydrologic connectivity increases denitrification in the hyporheic zone and restored floodplains of an agricultural stream, *J. Geophys. Res.,* 117(G3), G00N04, doi:10.1029/2012JG001950.

Rusjan, S., and M. Mikoš (2010), Seasonal variability of diurnal in-stream nitrate concentration oscillations under hydrologically stable conditions, *Biogeochemistry,* 97(2-3), 123-140, doi:10.1007/s10533-009-9361-5

Rutherford, J. C., N. A. Marsh, P. M. Davies, and S. E. Bunn (2004), Effects of patchy shade on stream water temperature: how quickly do small streams heat and cool?, *Mar*. *Freshwater Res.,* 55(8), 737-748, http://dx.doi.org/10.1071/MF04120

Rutherford, J., G. Latimer, and R. Smith (1993), Bedform mobility and benthic oxygen uptake, *Water Res,* 27(10), 1545-1558. doi:10.1016/0043-1354(93)90099-4

Saad, O. A., and R. Conrad (1993), Temperature dependence of nitrification, denitrification, and turnover of nitric oxide in different soils, *Biol. Fertil. Soils*, 15(1), 21-27, doi: 10.1007/BF00336283

Sawyer, A. H., and M. B. Cardenas (2009), Hyporheic flow and residence time distributions in heterogeneous cross-bedded sediment, *Water Resour. Res*., 45(8), W08406, doi:10.1029/2008WR007632.

Sawyer, A. H., M. B. Cardenas, and J. Buttles (2011), Hyporheic exchange due to channel-spanning logs, *Water Resour. Res,* 47(08). doi: 10.1029/2011WR010484.

Sawyer, A. H., M. B. Cardenas, and J. Buttles (2012), Hyporheic temperature dynamics and heat exchange near channel-spanning logs, *Water Resour.Res*, 48(1), W01529. doi: 10.1029/2011WR011200.

Schmidt, E. (1979), *Properties of water and steam in SI-units*. Springer, New York.

Scholefield, D., T. Le Goff, J. Braven, L. Ebdon, T. Long, and M. Butler (2005), Concerted diurnal patterns in riverine nutrient concentrations and physical conditions, *Sci. Total Environ.,* 344(1), 201-210, http://dx.doi.org/10.1016/j.scitotenv.2005.02.014

Seitzinger, S. P., R. V. Styles, E. W. Boyer, R. B. Alexander, G. Billen, R. W. Howarth, B. Mayer, and N. Van Breemen (2002), Nitrogen retention in rivers: model development and application to watersheds in the northeastern USA, *Biogeochemistry*, 57(1),199-237. doi:10.1023/A:1015745629794

Sharma, L., J. Greskowiak, C. Ray, P. Eckert, and H. Prommer (2012), Elucidating temperature effects on seasonal variations of biogeochemical turnover rates during riverbank filtration, *J. Hydrol.,* 428, 104-115. doi: 10.1016/j.jhydrol.2012.01.028.

Sheibley, R. W., A. P. Jackman, J. H. Duff, and F. J. Triska (2003), Numerical modeling of coupled nitrification–denitrification in sediment perfusion cores from the hyporheic zone of the Shingobee River, MN, *Adv. Water Resour.*, 26(9), 977-987. doi:10.1016/S0309-1708(03)00088-5.

Stanford, J. A., and J. V. Ward (1988), The hyporheic habitat of river ecosystems, *Nature,* 335(6185), 64-66. doi:10.1038/335064a0.

Svendsen, L. M., and B. Kronvang (1993), *Retention of nitrogen and phosphorus in a Danish lowland river system: implications for the export from the watershed*, pp. 123-135, Springer. doi: 10.1007/978-94-011-1602-2_15.

Swanson, T. E., and M. B.Cardenas (2010), Diel heat transport within the hyporheic zone of a pool-riffle-pool sequence of a losing stream and evaluation of models for fluid flux estimation using heat, *Limnol. Oceanogr.,* 55(4), 1741-1754. doi: 10.4319/lo.2010.55.4.1741.

Thamdrup, B., J. W. Hansen, and B. B. Jørgensen (1998), Temperature dependence of aerobic respiration in a coastal sediment, *FEMS Microbiol. Ecol.*, 25(2), 189-200, doi: http://dx.doi.org/10.1111/j.1574-6941.1998.tb00472.x.

Thibodeaux, L. J., and J. D. Boyle (1987), Bedform-generated convective transport in bottom sediment, *Nature*, 325(6102), 341-343, doi:10.1038/325341a0

Tonina, D., and J. M. Buffington (2007), Hyporheic exchange in gravel bed rivers with pool-riffle morphology: Laboratory experiments and three-dimensional modeling, *Water Resour.Res*., 43(1). W01421, doi:10.1029/2005WR004328.

Tonina, D., and J. M. Buffington (2009), Hyporheic Exchange in Mountain Rivers I: Mechanics and Environmental Effects, *Geog. Compass*, 3(3), 1063-1086, doi: 10.1111/j.1749-8198.2009.00226.x

van Rijn, L. C. (1984a), Sediment transport, part III: bed forms and alluvial roughness, *J. Hydraul. Eng*., 110(12), 1733–1754,doi: 10.1061/(ASCE)0733-9429

Van Rijn, L. C. (1984b), Sediment transport, part I: bed load transport, *J. Hydraul. Eng*., 110(10), 1431-1456.doi: 10.1061/(ASCE)0733 9429

Van Rijn, L. C. (1993), *Principles of sediment transport in rivers, estuaries and coastal seas*, Aqua publications, Amsterdam, the Netherlands.

Veraart, A. J., J. J. M. de Klein, and M. Scheffer (2011), Warming can boost denitrification disproportionately due to altered oxygen dynamics, *PloS one*, 6(3), e18508. doi:10.1371/journal.pone.0018508.

Webb, B., and D. Walling (1993), Longer-term water temperature behaviour in an upland stream, *Hydrol. Process*, 7(1), 19-32, doi:10.1002/hyp.3360070104

Wilcox, D. (1991), A half century historical review of the k-w model. AIAA 91-0615.

Wondzell, S. M., and F. J. Swanson (1996), Seasonal and storm dynamics of the hyporheic zone of a 4th-order mountain stream. II: Nitrogen cycling, *J. North Am. Benthol. Soc.*.15, 20-34, doi: 10.2307/1467430

Yvon-Durocher, G., et al. (2012), Reconciling the temperature dependence of respiration across timescales and ecosystem types, *Nature,* 487(7408), 472-476, doi:10.1038/nature11205

Zarnetske, J. P., R. Haggerty, S. M. Wondzell, and M. A. Baker (2011), Labile dissolved organic carbon supply limits hyporheic denitrification, *J. Geophys. Res. Biogeosci.,* 116, G04036, doi: 10.1029/2011JG001730.

Zarnetske, J. P., R. Haggerty, S. M. Wondzell, V. A. Bokil, and R. González-Pinzón (2012), Coupled transport and reaction kinetics control the nitrate source-sink function of hyporheic zones, *Water Resour. Res.,* 48(11), W11508, doi: 10.1029/2012WR011894

Zarnetske, R. Haggerty, S. M. Wondzell, and M. A. Baker (2011), Dynamics of nitrate production and removal as a function of residence time in the hyporheic zone, *J. Geohys. Res.,* 116(G1), G01025, doi:10.1029/2010JG001356

Zheng, L., M. B. Cardenas, and L. Wang (2016), Temperature effects on nitrogen cycling and nitrate removal-production efficiency in bed form-induced hyporheic zones, *J. Geophys. Res. Biogeosci.,* 121(4), 1086-1103, doi:10.1002/2015JG003162.